THESIS WORK

Master of Science in Energy Technology

Instituto Tecnológico de Buenos Aires - Karlsruhe Institute of Technology

System Performance of Resistive Mixers as Part of an Integrated D-Band Single Antenna Radar Transceiver

Selina Eckel

Tutor
Dr. Ing. Markus Rösch (IAF)

Examiners
Prof. Dr. Ing. Thomas Zwick (KIT)
Prof. Dr. Ing. Martin Gabi (KIT) / Dr.Ing. Cecilia Smoglie (ITBA)

Karlsruhe
03/07/2019

Declaration

I hereby declare that I wrote my Master Thesis on my own and that I have followed the regulations relating to good scientific practice of the Karlsruhe Institute of Technology (KIT) in its latest form. I did not use any unacknowledged sources or means and I marked all references I used literally or by content.

Karlsruhe, 03.07.2019

Selina Eckel

Abstract

In the development of renewable energies, there is a trend towards larger wind turbines with rotor blade diameters reaching hundreds of meters. This increases the demands placed on the materials being used, requiring reliable material testing during the manufacturing process.

At the Fraunhofer Institute for Applied Solid State Physics IAF, an integrated D-Band FMCW radar transceiver has been developed for these applications. During the characterization of the transceiver, however, the conversion gain of the integrated mixer shows undesired dips within the operating bandwidth, which leads to a decreased system performance.

This work investigates the characteristics of the integrated FET resistive mixer within the given system context. Based on simulations, different hypotheses regarding the cause of the described behavior are formulated. In order to verify these assumptions, a theoretical model extending the standard mixer analysis is developed as well as a measurement setup enabling the investigation of an individual mixer cell within a precisely controlled artificial system environment.

An undesired coupling path of the local oscillator (LO) signal via the parasitic drain-gate capacitance is identified as the main culprit. In addition, it is shown that the strength of its impact on the conversion gain is significantly influenced by the effective delay between this coupling path and the original LO signal.

To compensate for the effective delay and thus eliminate the dips in the conversion gain, three different approaches for the realization of a delay cell in the LO path are introduced and evaluated based on different criteria. With respect to its practicability and efficient space utilization, a slow-wave structure with alternating metal stripes underneath a coplanar waveguide shows the most promising results.

Zusammenfassung

Beim Ausbau der erneuerbaren Energien wird bei Windkraftanlagen unter anderem auf größere Durchmesser der Rotorblätter gesetzt. Dies erhöht die Anforderungen an das verwendete Material, wodurch der Materialuntersuchung während des Herstellungsprozesses eine große Bedeutung zukommt.

Der hier untersuchte FMCW Radartransceiver im D-Band, der am Fraunhofer Institut für Angewandte Festkörperphysik IAF entwickelt wurde, kann unter anderem zur Materialprüfung eingesetzt werden. Der Konversionsgewinn des integrierten Mischers zeigt jedoch bei der Charakterisierung des Systems unerwünschte Einbrüche über der Systembandbreite, die zu einer Verschlechterung der Systemeigenschaften führen.

Diese Arbeit beschäftigt sich mit dem Verhalten des eingesetzten resistiven FET-Mischers im gegebenen Systemkontext. Basierend auf Simulationen werden verschiedene Hypothesen zur Ursache des beschriebenen Verhaltens aufgestellt, die anschließend durch ein gegenüber der klassischen Mischer-Analyse erweitertes Modell und einen im Rahmen der Arbeit entwickelten Messaufbau verifiziert werden. Dabei wird ein unerwünschter Koppelpfad des Lokaloszillatorssignals (LO) über die parasitäre Gate-Drain Kapazität des Transistors als Hauptursache identifiziert. Darüber hinaus wird gezeigt, dass die Stärke des Effekts maßgeblich von der effektiven Verzögerung zwischen dem Koppelpfad und dem ursprünglichen LO-Signal beeinflusst wird.

Um diese effektive Verzögerung und damit die Einbrüche im Konversionsgewinn zu kompensieren, werden drei Ansätze zur Realisierung einer Verzögerungsstruktur im LO-Pfad vorgestellt und anhand verschiedener Kriterien evaluiert. Hinsichtlich Umsetzbarkeit und effizienter Raumausnutzung zeigt eine Slow-Wave-Struktur mit alternierenden Metallstreifen unterhalb einer koplanaren Leitung die vielversprechendsten Ergebnisse.

Resumen

En el desarrollo de las energías renovables hay una tendencia hacia turbinas eólicas más grandes con aspas del rotor de diámetros hasta cientos de metros. Esto aumenta las demandas que se imponen a los materiales empleados y require pruebas fiables de los materiales en el proceso de fabricación.

En el Instituto Fraunhofer de Física Aplicada del Estado Sólido se ha desarrollado un transceptor de radar FMCW de banda D integrado para estas aplicaciones. Durante las caracterizaciones de este transceptor, la ganancia de conversión del mezclador integrado muestra caídas no deseadas en el ancho de banda operado que lleva a una disminución del rendimient del sistema.

Esta tesis trata sobre el comportamiento del mezclador FET resistivo utilizado en el contexto del sistema. A partir de simulaciones, diferentes hipótesis se formulan sobre la causa del probelma descritos. Para verificar estos supuestos se desarolla un modelo teórico que amplía el análisis estándar del mezclador y además una configuracón de medida especia.

Una ruta de acoplamiento no deseada de la señal del oscilador local (LO) a través de la capacidad parásita de puerta-drenador es identificada como la causa princial. También se demuestra que la intensidad del efecto depende en gran medida del retraso efectivo ente la ruta de acoplamiento y la señal de LO original.

Para compensar el retardo efectivo y eliminar así las caídas en la ganacia de conversión, se introducen y evalún tres enfoques diferentes para la realización de una celda de retraso en la trayectoria LO. Con respecto a factibilidad y el uso eficiente del espacio muestra una estructura de “slow-wave” con tiras metálicas alternas debajo de líneas coplanares los resultados prometedores.

Danksagung

An erster Stelle möchte ich herzlich meinem Betreuer Markus Rösch danken für die Auswahl eines vielseitigen und ergiebigen Themas und seine Unterstützung in jeder Phase dieser Arbeit.

Herrn Professor Zwick danke ich für seine engagierte Förderung während meines Studiums und die Gelegenheit, meine Masterarbeit in Kooperation mit dem Fraunhofer IAF anzufertigen. Außerdem danke ich ihm für die Übernahme des Erstgutachtens.

Ich danke allen Kollegen am IAF für die geduldige Beantwortung meiner Fragen und die Bereitschaft, mich bei der Umsetzung meiner Ideen zu unterstützen. Ich konnte viele wertvolle Erfahrungen während meiner Zeit am IAF sammeln, die meine Begeisterung für das Hochfrequenz-Schaltungsdesign noch verstärkt haben.

Schließlich gilt mein besonderer Dank meiner Familie und meinen Freunden, die mich nicht nur während der Anfertigung dieser Arbeit immer unterstützt haben.

Contents

1 Introduction

1.1 Motivation

Today's information society sees a continuous increase in the number of electronic devices present in our everyday lives, the amount of data being generated and processed by these devices and consequently the total energy consumption of the world. At the same time, a responsible and sustainable global energy supply is more important now than ever before.

Facing these challenges, fossil energy sources are being replaced by renewable alternatives such as solar, wind and biomass energy in many contexts. In Germany, $50\,\%$ of the renewable energies are generated by wind turbines [Bun]. To harvest the potential of wind energy to a higher degree, there is a strong trend towards taller wind turbines featuring rotor blades with larger diameters (currently up to $118\,\mathrm{m}$ [Win]). During operation these blades are exposed to strong forces while their failure poses an immense safety and financial risk. As a consequence, reliable quality control during the manufacturing process, which usually involves the reinforcement of epoxy-based plastics with glass-fibers, is highly desirable. Any imperfections in the composition and layering of the materials can lead to structural weaknesses (and eventually catastrophic failures) that need to be detected early in the production process. If it is not possible to detect those defects, the thickness of the blades has to be increased in order to include tolerances. This leads to a reduced system efficiency of the wind turbines and causes economical disadvantages to manufacturers and insurance companies.

Millimeter-wave imaging systems based on radar technology offer a promising way to detect and classify many of these defects [Mei+19]. It neither requires a coupling medium present in ultrasonic systems [GH94] nor additional safety measures as with hazardous X-Rays [FL16] and it inherently provides three-dimensional information as compared to e.g. thermographic approaches [DSM15]. A suitable radar system should be compact and have a wide bandwidth in order to provide sufficient classification and detection performance. This master thesis focuses on a radio frequency (RF) radar front end that can be used as part of a millimeter-wave imaging system.

1.2 Scope

To meet the above-mentioned requirements, a frequency modulated continuous wave (FMCW) radar transceiver has been developed at the Fraunhofer Institute for Applied Solid State Physics (IAF) in Freiburg. It offers a bandwidth of $30\,\mathrm{GHz}$ in the frequency range of $130\,\mathrm{GHz}$ to $160\,\mathrm{GHz}$ and compactness is achieved by using a single antenna for transmitting and receiving.

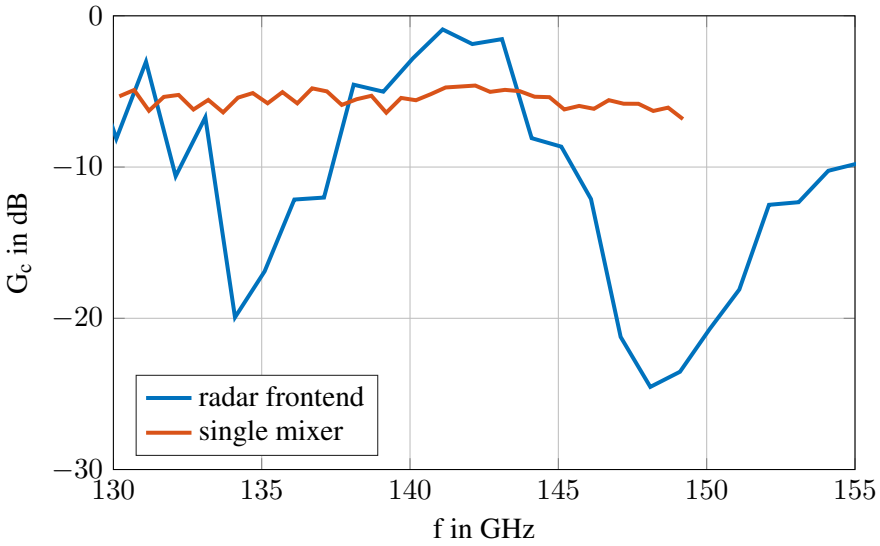

Figure 1.1: Measurement results of the conversion gain versus frequency of the single resistive mixer and the integrated radar transceiver, the latter showing two large dips which negatively affect the system performance.

One central element of the FMCW radar is the mixer used as a down converter. An important figure of merit is its conversion gain G_c, which should ideally remain relatively constant over the system bandwidth. In order to test the functionality of the system, G_c was measured at the individual mixer and at the integrated radar transceiver. The results are shown in Fig. 1.1. The measurement at the individual mixer shows the desired constant conversion gain over the frequency, whereas the measurement at the entire radar front end shows unwanted dips in G_c.

In order to obtain a high depth resolution, information on the received signal needs to be available to the subsequent signal processing stages over the entire operating bandwidth. Due to the dips in G_c, information is missing during some parts of the FMCW ramp, which leads to a drop in the signal-to-noise ratio (SNR) and ultimately to a lower system performance. In terms of material testing, this can result in a poorer resolution of the defect shapes and has a negative impact on the available depth information.

Preliminary experiments identify a non-ideal but potentially unavoidable coupling path from the transmitted local oscillator (LO) to the receiver as the main culprit causing the observed problems at the receiving mixer. At the beginning of this work, several unstructured and partly contradictory hypotheses existed regarding the exact coupling mechanism and, consequently, the possible options for eliminating the problem. A detailed understanding of the mixer's behavior in the transceiver context was lacking as well as an experimental verification of any of the possible explanations. From this initial situation, the main goals of this work are derived as follows:

1. Gain a structured and in-depth understanding of the performance of the used resistive mixer in the context of a single-antenna radar transceiver. Ideally, the gained knowledge is not limited to a specific frequency of operation or the integrated circuit analyzed in this work but can be applied to a wider range of future designs.

2. If possible, identify a small number of accessible system or circuit parameters that determine the observed behavior of the conversion gain.
3. Verify the developed models and hypotheses experimentally, i. e. by appropriate measurements e. g. at the individual mixer.
4. Based on the previous analyses, research possible solutions and assess their applicability while observing existing boundary conditions such as system requirements and the characteristics of the available technology.

The remainder of this thesis is structured accordingly: In the second chapter, the fundamentals of the investigated system are discussed in a top-to-bottom fashion, covering FMCW radar, mixer analysis in general and resistive mixers based on the IAF technology in particular. The third chapter is devoted to the analysis and simulation of mixers in the presence of significant LO coupling, starting with technology-specific simulations and culminating in the derivation and solution of several general analytic models reproducing the relevant effects. In the fourth chapter, the conclusions drawn from the systematic analysis of the mixer are verified by a series of measurements. As the measurement concept was devised and implemented as part of this work, a part of this chapter discusses some of the practical challenges and the developed solutions associated with the setup. In the fifth chapter, a number of possible options to eliminate or at least reduce the impact of the coupling path on the receiver's performance are discussed, ranging from relatively simple to more complex approaches based on active delays and slow-wave structures. These options are evaluated with respect to their applicability in the context of the available technology as well as their efficiency. A short conclusion is given in the last chapter together with some suggestions for future research.

2 Fundamentals

2.1 FMCW Radar

From the system level perspective, this work is about radar technology. As the name "RAdio Detection And Ranging" (Radar) suggests, a radar system is able to determine the distance of a target using radio frequencies. A transmitter sends a signal which is reflected by a target. The receiver detects the reflected signal and the distance can be calculated by comparing the transmitted and the received signal.

The Monolithic Microwave Integrated Circuit (MMIC) considered in this thesis is part of a frequency modulated continuous wave radar front end. A high level block diagram can be seen in Fig. 2.1. A local oscillator (LO) generates a linear chirp signal. The LO signal is amplified by a power amplifier (PA) and transmitted by an antenna. The signal is reflected by a target at a distance R. At the radar front end, the received RF signal is amplified by a low noise amplifier (LNA). To obtain the desired range information, the received signal is mixed with a portion of the LO signal. The mixer operating as a down converter generates the intermediate frequency (IF), which is digitized by an analog-to-digital converter (ADC) and processed by a digital signal processor (DSP) [Ram17].

One of the most common modulation forms for the LO signal is a sawtooth pattern as shown in Fig. 2.2. For a stationary single point target, the received RF signal is a delayed and attenuated copy of the transmitted signal. The frequency difference of the two signals is the IF frequency given by

$$f_{\mathrm{IF}} = \frac{B}{T}\tau \tag{2.1}$$

with the bandwidth B and the ramp duration T. With the delay of the transmitted and received

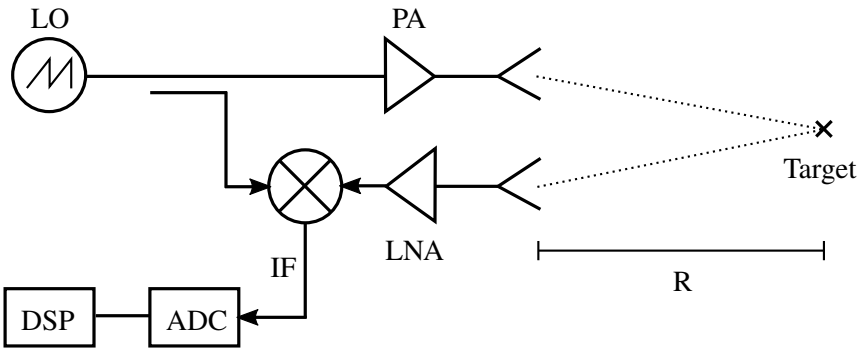

Figure 2.1: High level block diagram of an FMCW radar. A portion of the transmitted LO signal is mixed with the received RF signal to produce a beat signal at the frequency f_{IF}.

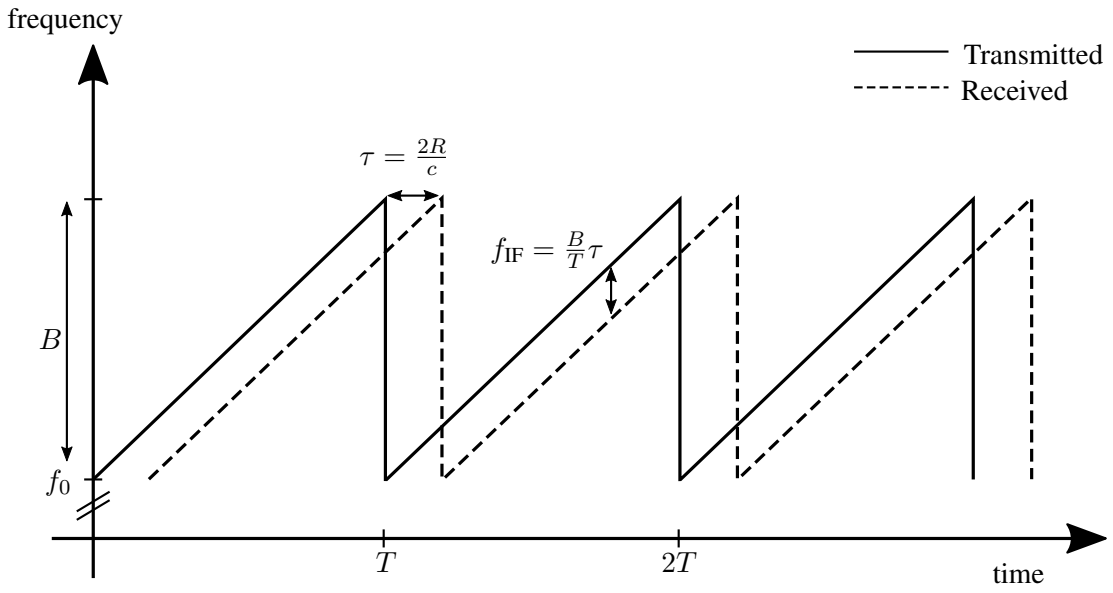

Figure 2.2: Sawtooth signal pattern for FMCW.

signal

$$\tau = \frac{2R}{c} \tag{2.2}$$

the IF frequency is given by

$$f_{\text{IF}} = \frac{B}{T} \cdot \frac{2R}{c} \tag{2.3}$$

and is therefore proportional to the distance R of the detected object, with c as propagation velocity.

To determine the IF frequency, the fast Fourier transform (FFT) of the IF time domain signal has to be computed. The ideal spectrum shows a single tone at the IF frequency.

The range resolution of an FMCW radar provides information about its ability to separate two different targets. It is calculated as

$$\delta R = \frac{cT}{2B} \cdot \delta(f_{\text{IF}}). \tag{2.4}$$

$\delta(f_{\text{IF}}) = \frac{1}{T}$ describes the minimum distance of two frequencies which can still be separated by the FFT. As a consequence, the range resolution is related to the bandwidth via

$$\delta R = \frac{c}{2B}. \tag{2.5}$$

It can be seen that the bandwidth directly influences the achievable resolution. This result holds in a much more general radar context. [Bro05]

On the other hand, the accuracy of an FMCW radar is defined with respect to a single target. It is a measure of how accurately the distance R to one target can be determined as indicated by Fig. 2.1. It is related to the standard deviation of the measured distance R and is inversely proportional to the SNR.

2.2 Mixers

On the circuit level, the focus of this work is on the mixing device. As mentioned above, mixers are used in radar systems to down convert the RF frequency to the IF frequency.

2.2.1 Basics

A mixer is a three-port device and the schematic of a down converter is shown in Fig. 2.3. An ideal mixer is a multiplier where the RF signal is multiplied with the LO signal resulting in the desired IF signal. The LO and RF signals are described as

$$s_{\mathrm{LO}}(t) = a_{\mathrm{LO}}(t)\cos(\omega_{\mathrm{LO}}t) \tag{2.6}$$

$$s_{\mathrm{RF}}(t) = a_{\mathrm{RF}}(t)\cos(\omega_{\mathrm{RF}}t) \tag{2.7}$$

with the time-varying amplitudes a. Using trigonometric identities, the output signal includes the sum and difference frequencies of the input signals as shown in Eq. 2.8. The difference frequency presents the desired IF signal whereas the undesired sum frequency has to be filtered out.

$$s_{\mathrm{LO}}(t)\cdot s_{\mathrm{RF}}(t) = \underbrace{a(t)\cos((\omega_{\mathrm{RF}}+\omega_{\mathrm{LO}})t)}_{\text{filtered}} + \underbrace{a(t)\cos((\omega_{\mathrm{RF}}-\omega_{\mathrm{LO}})t)}_{s_{\mathrm{IF}}(t)} \tag{2.8}$$

$$\text{with } a(t) = \frac{1}{2}a_{\mathrm{LO}}(t)\cdot a_{\mathrm{RF}}(t).$$

To realize the multiplication at high frequencies, devices with a non-linear characteristic curve can be used. The non-linear relationship between voltage and current of diodes and transistors is a suitable example.

There are a few important figures of merit which characterize a mixer. The conversion gain or conversion loss G_c describes the ratio of the available IF output power to the available RF input power

$$G_c = 10\log\frac{\text{available IF output power}}{\text{available RF input power}}\text{dB}. \tag{2.9}$$

The losses in the mixer occur due to the generation of undesired harmonics and other frequency products. Besides, resistive loads increase mixer losses further. The noise figure is important to predict the lowest detectable IF signal level, i.e. the sensitivity of the mixer. By diode or transistor elements and thermal sources due to resistive losses, noise is generated. As non-linearity is used

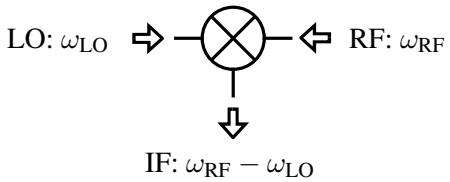

Figure 2.3: Schematic of a mixer operated as a down converter.

for mixing, intermodulation products are generated and the third order intercept point has to be considered. The isolation between RF and LO port is not ideal due to parasitic elements of the transistor. Therefore, the LO isolation also needs to be taken into account [Poz12].

2.2.2 Passive FET Mixers

Field-effect transistors (FETs) enable the design of mixers with a lower noise figure as compared to diode mixers. Passive FET mixers have advantages over active ones in terms of linearity, bandwidth and power consumption [LD15]. Based on the mentioned benefits, this work focuses on passive FET mixers.

Topologies

The three different ways in which the LO/RF signal can be applied to the terminals of the FET in order to exploit its non-linearity are shown in Fig. 2.4.

1) The FET drain mixer uses the LO signal applied to the drain to modulate the transconductance g_{m} and the drain/source conductance g_{DS} of the FET. The FET drain mixer therefore changes the gain of a common source amplifier. The bias condition is around the characteristic "knee". The advantages are the capability of providing a conversion gain and a low noise figure. The disadvantage is the required additional DC bias [Gun+08].
2) In a FET gate mixer the LO and RF signals are applied to the gate. The main contributor to the mixing process is the time-varying transconductance g_{m}. The bias condition is close to the transistor's threshold voltage V_{T}. The advantages of the FET gate mixer are the low LO power requirement and the possibility to realize a positive conversion gain instead of a conversion loss. The disadvantage is its relative complex structure due to the need of a diplexer network [Maa03].
3) In the case of a FET resistive mixer, the LO signal is applied to the gate of the FET and modulates the drain/source conductance g_{DS}. The FET acts like a variable resistor when looking from the drain to the source. The bias condition is at pinch-off. The advantages are the high linearity and robust performance. Because there is no need for DC bias, the DC power consumption is zero, but on the downside the mixer possesses a conversion loss. Furthermore, it needs a relatively high LO power [Gun+08].

Resistive Mixers

Due to the above-mentioned advantages of resistive mixers, especially its high linearity and robust performance, this mixer topology was originally chosen for the radar chip. The FET resistive mixer uses the channel of the FET as an approximately linear resistor at low drain-to-source-voltages for converting the RF frequency to the IF frequency. By applying a LO voltage to the gate, the depth of the depletion region under the gate and therefore the resistance of the channel changes. The range

of resistance varies from a few ohms when the gate voltage reaches its maximum value to very large values when the gate voltage drops below V_{T} [Maa03].

To understand the multiplication process of the resistive mixer mathematically, it is useful to consider the large signal and small signal behavior separately.

For the large signal modulation of g_{DS} a periodic LO signal is applied to the gate. The LO signal instantaneously modulates the conductance of the FET channel. In addition, a bias voltage U_{bias} shifts the mean value of the LO signal to an appropriate operating point. The large signal voltage at the gate is given by

$$U_{\mathrm{G}} = U_{\mathrm{B}} + U_{\mathrm{LO}} \cos(\omega_{\mathrm{LO}} t). \tag{2.10}$$

Around the operating point, the small RF signal is applied to the unbiased drain. In the small signal model this corresponds to a voltage applied to the time-varying channel conductance g_{DS}. The corresponding small signal equivalent circuit is shown in Fig. 2.5. The FET is reduced to its channel conductance and the voltages of the RF and IF signal applied to the drain are coupled via ideal transformers. The small signal voltage at the drain is given by

$$u_{\mathrm{DS}} = U_{\mathrm{RF}} \cos(\omega_{\mathrm{LO}} t) + U_{\mathrm{IF}} \cos(\omega_{\mathrm{IF}} t) \tag{2.11}$$

The mathematical operation of multiplication can be seen when calculating the non-linear drain-source current i_{DS} as a function of u_{DS} as given by

$$i_{\mathrm{DS}} = g_{\mathrm{DS}}(U_{\mathrm{gate}}) u_{\mathrm{DS}}. \tag{2.12}$$

The conductance g_{DS} changes periodically with ω_{LO}. Therefore, g_{DS} can be expanded into a Fourier series as

$$g_{\mathrm{DS}}(t) = \sum_{n=-\infty}^{+\infty} g_{\mathrm{DS}}^{n} \cdot e^{jn\omega_{\mathrm{LO}} t}. \tag{2.13}$$

Only the first two Fourier coefficients will be considered because higher order mixing products are not part of this analysis, so Eq. 2.13 simplifies to

$$g_{\mathrm{DS}}(t) \approx g_{\mathrm{DS}}^{0} + g_{\mathrm{DS}}^{1} e^{j\omega_{\mathrm{LO}} t} + g_{\mathrm{DS}}^{-1} e^{-j\omega_{\mathrm{LO}} t}. \tag{2.14}$$

Furthermore, $(g_{\mathrm{DS}}^{1})^{*} = g_{\mathrm{DS}}^{-1}$ holds because the conductance is real-valued, so the equation further simplifies to

$$\begin{aligned} g_{\mathrm{DS}}(t) &= g_{\mathrm{DS}}^{0} + g_{\mathrm{DS}}^{1} e^{j\omega_{\mathrm{LO}} t} + (g_{\mathrm{DS}}^{1})^{*} e^{-j\omega_{\mathrm{LO}} t} \\ &= g_{\mathrm{DS}}^{0} + 2 g_{\mathrm{DS}}^{1} \cos(\omega_{\mathrm{LO}} t). \end{aligned} \tag{2.15}$$

Inserting g_{DS} into Eq. 2.12 leads to

$$i_{\mathrm{DS}} = (g_{\mathrm{DS}}^{0} + 2 g_{\mathrm{DS}}^{1} \cos(\omega_{\mathrm{LO}} t)) \cdot (U_{\mathrm{RF}} \cos(\omega_{\mathrm{RF}} t) + U_{\mathrm{IF}} \cos(\omega_{\mathrm{IF}} t)). \tag{2.16}$$

The zeroth Fourier coefficient represents the DC component and the first Fourier coefficient leads to the desired mixing operation [Pet12].

In the small signal model, the mixer can be described as a linear two port network (2.17) by absorbing the non-linear mixing operation in g_{DS}. The matrix of g_{DS} has the form of a Y-matrix.

$$\begin{pmatrix} i_{\mathrm{RF}} \\ i_{\mathrm{IF}} \end{pmatrix} = \begin{pmatrix} g^0_{\mathrm{DS}} & g^1_{\mathrm{DS}} \\ (g^1_{\mathrm{DS}})^* & g^0_{\mathrm{DS}} \end{pmatrix} \cdot \begin{pmatrix} u_{\mathrm{RF}} \\ u_{\mathrm{IF}} \end{pmatrix} \tag{2.17}$$

The maximum conversion gain G_c of a mixer is formally equivalent to the gain of an amplifier and can be calculated from the Y-parameters, i.e. from the zeroth and first Fourier coefficients of g_{DS}. G_c is calculated according to Eq. 2.18 under the assumption of impedance matching to the characteristic impedance of the system [ST71].

$$G_c = \frac{1 - \sqrt{1 - \left|\frac{g^1_{\mathrm{DS}}}{g^0_{\mathrm{DS}}}\right|^2}}{1 + \sqrt{1 - \left|\frac{g^1_{\mathrm{DS}}}{g^0_{\mathrm{DS}}}\right|^2}} \tag{2.18}$$

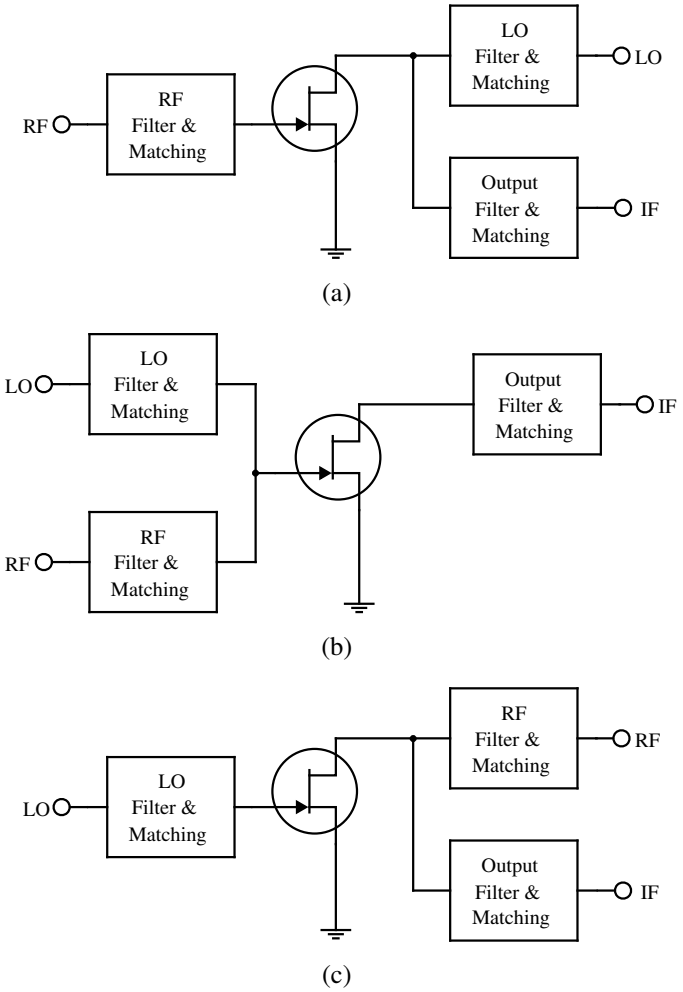

Figure 2.4: Topologies of different FET mixers, (a) FET drain mixer, (b) FET gate mixer and (c) FET resistive mixer.

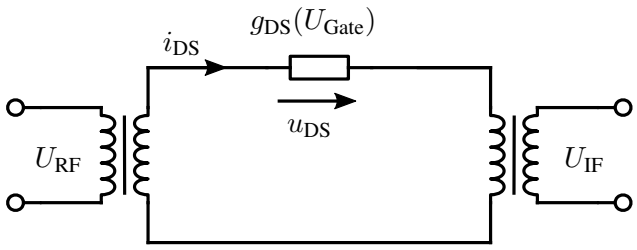

Figure 2.5: Small signal equivalent circuit of a resistive mixer with transformers for ideal voltage coupling of RF and IF. The transistor is reduced to its drain-source conductance.

2.3 Technology

The radar chip considered in this work has been fabricated on the Fraunhofer IAF $50\,\mathrm{nm}$ metamorphic high electron mobility transistor (mHEMT) technology grown on a semi-insulating 4" Gallium Arsenide (GaAs) substrate. The technology features integrated resistors, capacitors, airbridges, two front side metalization layers and a backside process with through substrate vias. Fig. 2.6 shows a simplified diagram of the layers and structures of the process.

The top metal layer (METG) has a thickness of $2.7\,\mu\mathrm{m}$ and features an air-bridge technology. The second metal layer (MET1) is thinner than METG with a thickness of $0.5\,\mu\mathrm{m}$. The material of the two metalization layers is gold. To realize on-chip metal-insulator-metal (MIM) capacitors with a capacitance of $0.225\,\mathrm{fF}/\mu\mathrm{m}^2$, a thin dielectric layer of $0.5\,\mu\mathrm{m}$ silicon-nitride (SiN) is placed between the metal layers. An integrated thin film resistor can be fabricated with a nickel-chromium (NiCr) alloy having a sheet resistance of $50\,\Omega/\mathrm{sq}$. The substrate consists of GaAs which is thinned to a thickness of $50\,\mu\mathrm{m}$ to suppress any unwanted propagation of electro-magnetic waves through the substrate. The material of the backside of the wafer is also gold. To realize grounded coplanar waveguide (GCPW) transmission lines, vias are introduced to connect the ground from the front side with the back side metalization.

The transistor used in this technology is a special type of FET, namely the mHEMT. It has a Schottky gate contact and provides a high electron mobility. This is achieved by means of a two-dimensional electron gas (2DEG) which is confined at the boundary of a special epitaxially grown heterostructure. The channel of the mHEMT consists of Indium Gallium Arsenide (InGaAs). A high electron mobility leads to potentially higher switching frequencies of the transistor and therefore also to higher mixing frequencies. These characteristics make the mHEMT an ideal candidate for the design of passive mixers in the upper mmW frequency range [LD15].

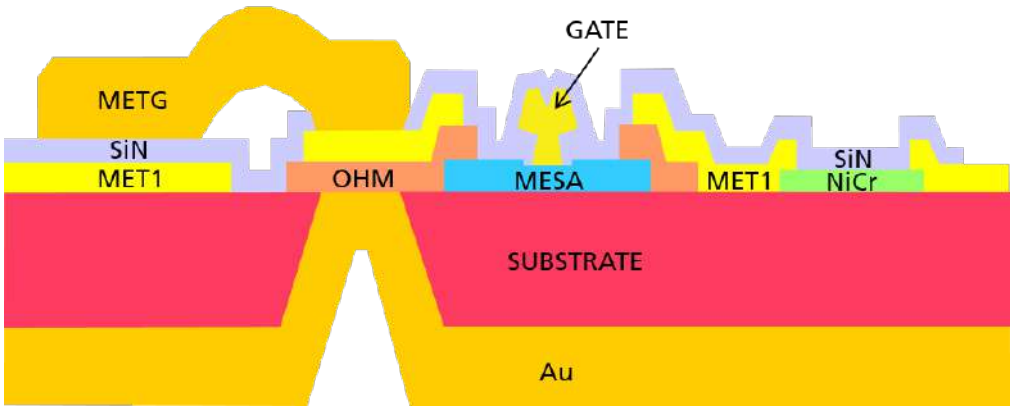

Figure 2.6: Layer structure of the IAF mHEMT technology.

3 Problem Quantification

3.1 Cause Analysis

In order to understand the emergence of the dips in the conversion gain, the setup of the radar front end is described in detail in the first part of this section. Based on simulations of the mixer the origin of the problem is elaborated and the impact of different parameters is investigated in the second part of the section.

3.1.1 System Level

Fig. 3.1 shows the detailed schematic of the investigated $140\,\mathrm{GHz}$ radar front end. The LO signal is generated at $24\,\mathrm{GHz}$ and multiplied by six to reach the desired frequency of $140\,\mathrm{GHz}$. The subsequent power divider splits the LO signal into two paths. The first one leads to a PA which amplifies the signal to reach a power level sufficient for the illumination of targets with a certain distance. Through a Lange coupler the LO signal is routed to an antenna where it is radiated. The received RF signal passes the Lange coupler to an LNA. The amplified RF signal is fed to the RF port of the mixer. The mixer is driven by the LO signal from the second path of the power divider. By down conversion, the IF signal is generated.

The desired LO/RF frequency range of the system is from $130\,\mathrm{GHz}$ to $160\,\mathrm{GHz}$, to meet the requirement of a wide bandwidth for a high range resolution.

The mixer is a FET resistive mixer as described in chapter 2. The system uses two resistive mixers to realize an In-phase and Quadrature (IQ) Mixer. An IQ-mixer has been originally selected due to a number of advantages. First, there is a potential decrease in noise bandwidth of up to $3\,\mathrm{dB}$ because the upper and lower sideband stay separated and noise as well as interference in the upper sideband are not folded back onto the desired signal. Second, as long as the intermediate frequency is in the first Nyquist zone of a single (I or Q) channel, the target information is essentially the same in both channels. This redundancy may be exploited for error or interference detection [Ram17].

The system uses a single antenna for transmitting and receiving. This meets the requirements of a compact and cost effective construction of the system. In addition, the targeted applications require a focused beam which is achieved by an antenna concept using a single lens that can not easily incorporate a second antenna without losing compactness or precision.

Using a single antenna results in a significant portion of the transmitter power leaking into the receiver due to the non-ideal isolation of the Lange coupler. In contrast to a pulsed radar this causes a problem for FMCW radars because of the simultaneous transmission and reception. In addition

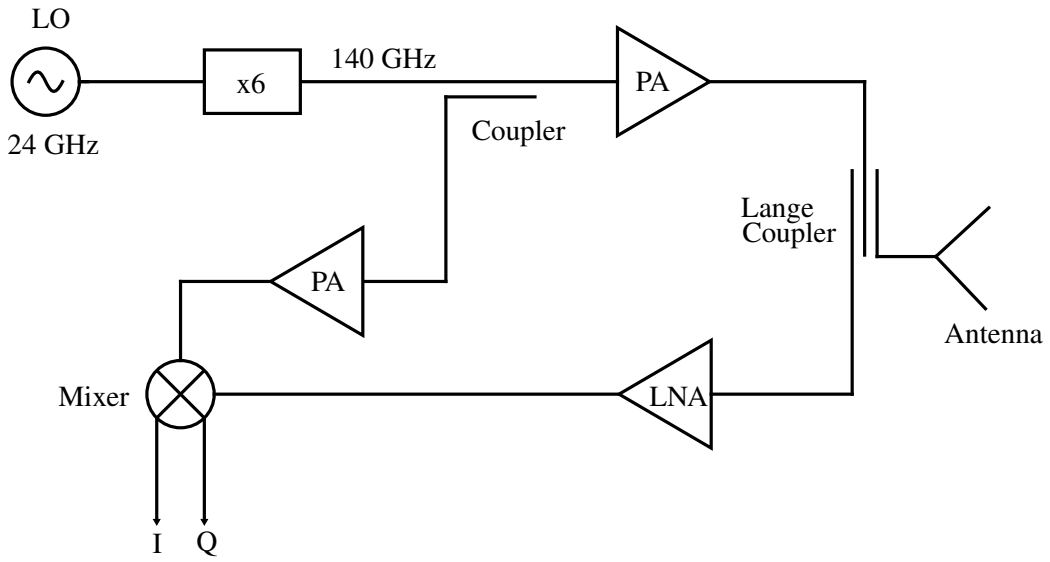

Figure 3.1: Block diagram of the 140 GHz radar front end. The transmitting and receiving paths are connected to the antenna via the non-ideal Lange coupler. This results in an unwanted feedback path for the LO signal. Consequently, the LO-RF signal is also present at the mixer.

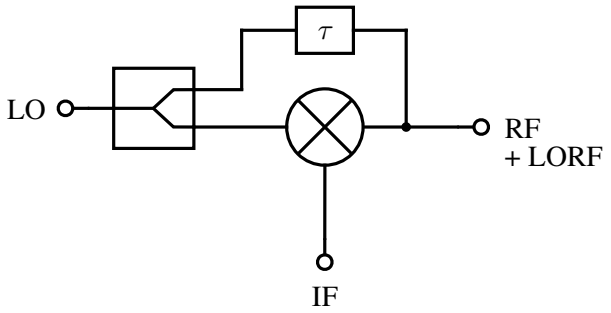

Figure 3.2: Reduced and modified block diagram of the radar front end focusing on the mixer. Beside the desired signals LO, RF and IF, the additional delayed LO-RF signal is applied to the RF port of the mixer.

to the desired RF signal, the LO signal is also coupled to the RF port of the mixer which is referred to as LO-RF signal in the following. Due to the LNA in the receiver path the power of the LO-RF signal is in the same order of magnitude as the LO signal itself. As a consequence, the mixer is negatively affected by the additional signal.

To further analyze the problem, the system can be reduced to the block diagram in Fig. 3.2. The LO-RF signal travels along a different path than the LO signal. Assuming an approximately linear phase response of the devices in the radar front end, the LO-RF signal has an effective delay of τ w.r.t. the LO signal. The effective delay is connected to the phase difference

$$\Delta\varphi = 2\pi f \tau \tag{3.1}$$

at the mixer. The rate at which $\Delta\varphi$ changes as a function of the frequency f is determined by τ.

Based on the previous considerations, it is assumed that the position of the dips in G_c correspond to a certain phase difference of the LO and LO-RF signal and so the peaks should occur periodically.

Table 3.1: Initial parameters for the ADS simulation.

Signal	P in dBm	φ in rad	f in GHz
LO	2	0	140.0
LO-RF	2	$2\pi f\tau$	140.0
RF	-25	0	140.1

From the 2π-periodicity of the phase, the separation of the dips Δf can be obtained as

$$2\pi f\tau = 2\pi(f + \Delta f)\tau + 2\pi \tag{3.2}$$

$$\Leftrightarrow \Delta f = \frac{1}{\tau}. \tag{3.3}$$

Analyzing the position of the dips in the measurement (Fig. 1.1) thus allows the calculation of τ. The first dip occurs at $f = 134\,\mathrm{GHz}$ and the second one at $f + \Delta f = 148\,\mathrm{GHz}$, leading to an effective delay of $\tau = 71\,\mathrm{ps}$. The higher the delay, the closer the peaks are to each other because the rate at which $\Delta\varphi$ changes increases.

The number of dips in the system bandwidth can be calculated as

$$n_{\mathrm{Dips}} = \frac{\Delta\varphi_{160\,\mathrm{GHz}} - \Delta\varphi_{130\,\mathrm{GHz}}}{2\pi} \tag{3.4}$$

$$= (f_{160\,\mathrm{GHz}} - f_{130\,\mathrm{GHz}})\tau \tag{3.5}$$

which yields $n_{\mathrm{Dips}} = 2.13$ for $\tau = 71\,\mathrm{ps}$. Thus, every phase difference of the LO signal w.r.t. the LO-RF signal occurs approximately twice in the bandwidth of interest. As the position of the dips presumably corresponds to a certain phase difference, the dips occur twice.

To verify the assumptions about the effective delay of both signals, a simulation with the software Advanced Design System (ADS) by Keysight Technologies is performed. The simulation setup is shown in the block diagram in Fig. 3.2. To simulate the non-linear behavior of the mixer, a Harmonic Balance (HB) simulation is chosen. HB solves a non-linear system of equations in the frequency domain and calculates a time-varying DC operating point [Kun99]. Table 3.1 lists the initial parameters of the simulation environment exemplarily for one frequency.

For a delay of $71\,\mathrm{ps}$ the dips in the simulation correspond to the measurement results as seen in Fig. 3.3, which confirms the assumptions regarding τ.

This result shows that the simulation setup with the given transistor models of the IAF mHEMT replicate the problem in good agreement with the measurements. In contrast to the measurement, the simulation offers the possibility to easily tune different parameters and thus further analyze the dips.

The impact of different delays is demonstrated in Fig. 3.4(a) which shows G_c for a delay of $0\,\mathrm{ps}$, $71\,\mathrm{ps}$ and $141\,\mathrm{ps}$. It can be seen that the separation of the dips becomes smaller for higher τ as predicted by Eq. 3.3.

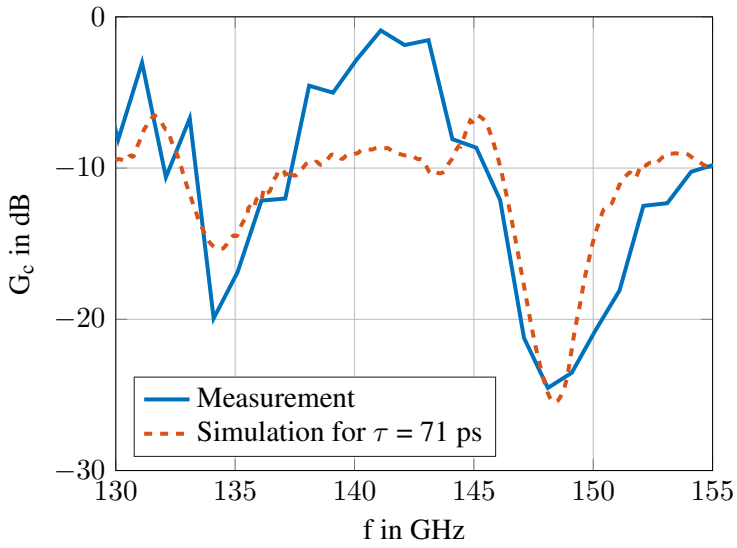

Figure 3.3: Comparison of the measured and simulated conversion gain for τ =71 ps. The simulation qualitatively resembles the measurement.

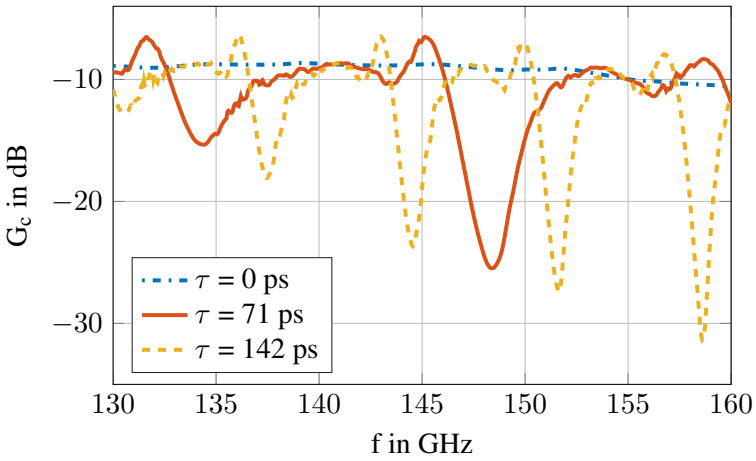

(a)

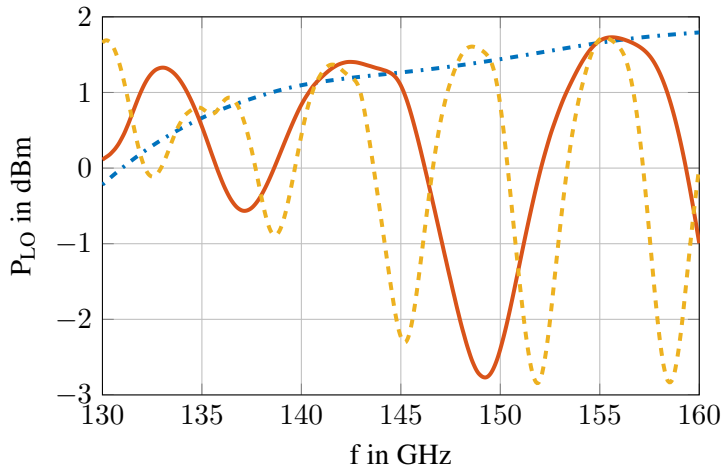

(b)

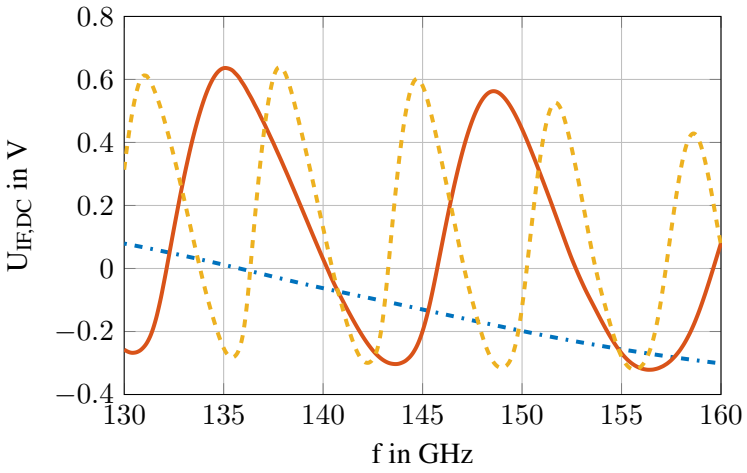

(c)

Figure 3.4: Simulation of the FET resistive mixer with different effective delays τ for the LO-RF signal w.r.t. the LO signal. All three quantities show a characteristic behavior in the vicinity of the dips. (a) shows the conversion gain, (b) the power of the LO signal and (c) the IF-DC voltage. The color coding of the curves is the same for all subfigures.

3.1.2 Circuit Level

To understand the mixer's behavior in the presence of the additional LO-RF signal in more detail, the mixer is analyzed on the circuit level. The circuit of the resistive mixer is shown in Fig. 3.5. The LO signal is applied to the gate and the RF, LO-RF and IF signals are present at the drain of the FET. The gate is biased with a voltage of $-0.2\,\mathrm{V}$.

Several transistor models of the IAF mHEMT were evaluated regarding their ability to predict the conversion gain without obvious artifacts. The available models differ in the description of the intrinsic transistor fingers and the outer parasitic shell. The bias-independent parasitic shell can be modeled with discrete or lumped elements. The chosen model consists of a shell with discrete elements and the transistor fingers are modeled as a mulit-port device which is described by its large signal equations [Ohl+16].

By investigating the behavior of the FET on the gate and drain side, the positions of the dips in G_c are compared to the frequency dependence of different parameters. Based on these correlations, two main assumptions for the dips are made and investigated.

Gate Node of the FET

To analyze the behavior of the FET from the gate side, the influence of P_{LO} is examined first. When comparing the shapes of G_c and the accepted LO power versus frequency (Fig. 3.4(b)), it is evident that P_{LO} shows minima at the same frequencies as the dips in G_c.

Based on this correlation, the first assumption regarding the occurrence of the dips can be formulated. The LO-RF signal affects the FET in such a way that, for a certain phase difference, the accepted LO power at the gate is significantly reduced. One possible explanation could be the parasitic gate-drain capacitance C_{GD} through which the LO-RF signal couples over the FET to the gate. Fig. 3.6 illustrates the resistive mixer with the parasitic capacitance C_{GD}. This results in a superposition of the LO and LO-RF signal at the gate, both having the same frequency. At a certain critical phase difference of both signals, destructive interference occurs and a drop in the available power at the gate leads to a reduced mixing efficiency.

To verify that behavior, the results of a sweep of the LO Power from 2 to $8\,\mathrm{dBm}$ are shown in

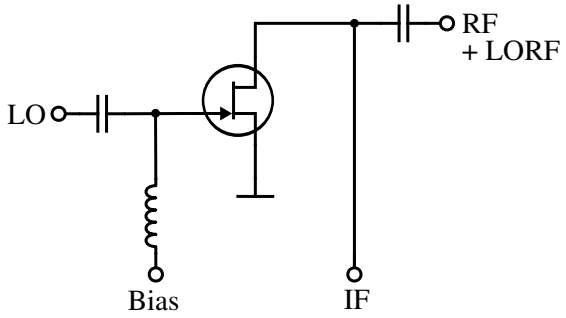

Figure 3.5: Circuit of the FET resistive mixer with the desired signals LO, RF and IF and the additional delayed LO-RF signal. The gate node is biased with U_{B}.

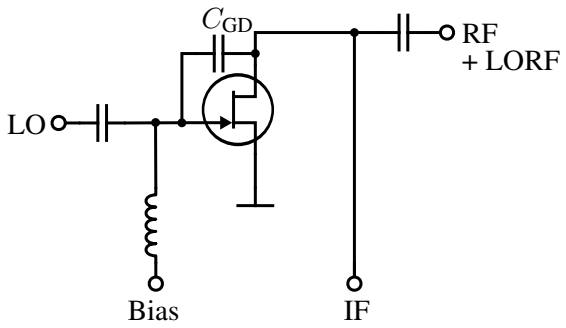

Figure 3.6: Schematic of the FET resistive mixer with the parasitic gate-drain capacitance. It is assumed that the LO-RF signal couples over C_{GD} to the gate node.

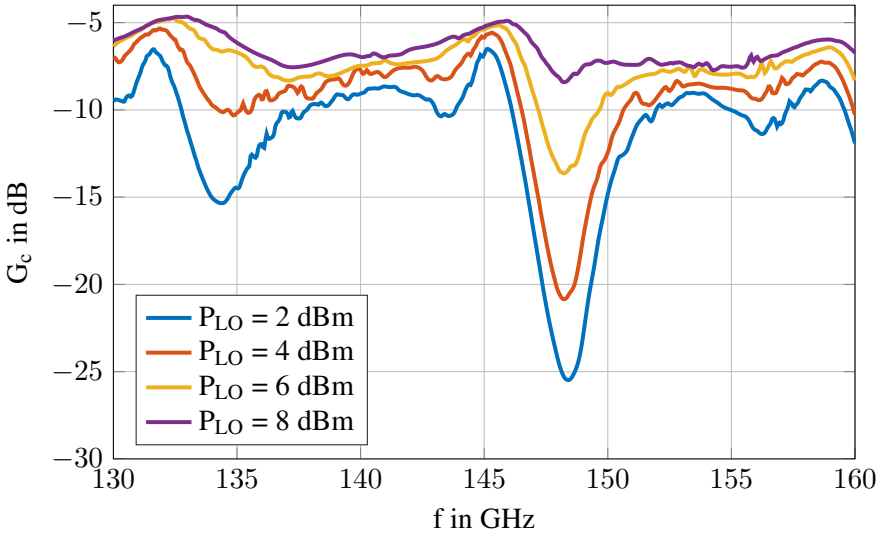

Figure 3.7: Simulation of the FET resistive mixer for different P_{LO} and $P_{LORF} = 2\,\mathrm{dBm}$ to investigate the impact of the ratio of P_{LO}/P_{LORF} on the dips in G_c.

Fig. 3.7. The power of the LO-RF signal is set to $2\,\mathrm{dBm}$. It can be seen that a high ratio of P_{LO}/ P_{LORF} corresponds to the dips becoming less pronounced. Looking at the characteristics of g_{DS} (Fig. 3.8), it becomes clear that for smaller gate voltages, i.e. smaller LO powers, the variation of g_{DS} is too small to sustain the mixing process. g_{DS} is calculated by differentiating I_D w.r.t. U_D at $U_G = 0$. If the ratio of P_{LO} to $P_{LO,RF}$ becomes larger, the influence of the LO-RF signal becomes smaller and the effect of destructive interference is reduced. It can be stated that the simulation with different ratios of P_{LO}/ P_{LORF} supports the first assumption of the occurrence of the dips.

Another parameter at the gate is the bias voltage. It is required to shift the mean value of the LO signal to an appropriate operating point. A simulation with different gate-bias voltages from $-0.5\,\mathrm{V}$ to $0\,\mathrm{V}$ is performed and the results are shown in Fig. 3.9. It can be noticed that the different bias voltages have an influence on the width and the depth of the dips. The smaller $U_{G,B}$, the deeper and wider the dips become.

Based on the first assumption this effect can be explained as follows. If the bias voltage is small, it shifts the mean value of the LO signal towards a region where the slope of g_{DS} (Fig. 3.9) is small.

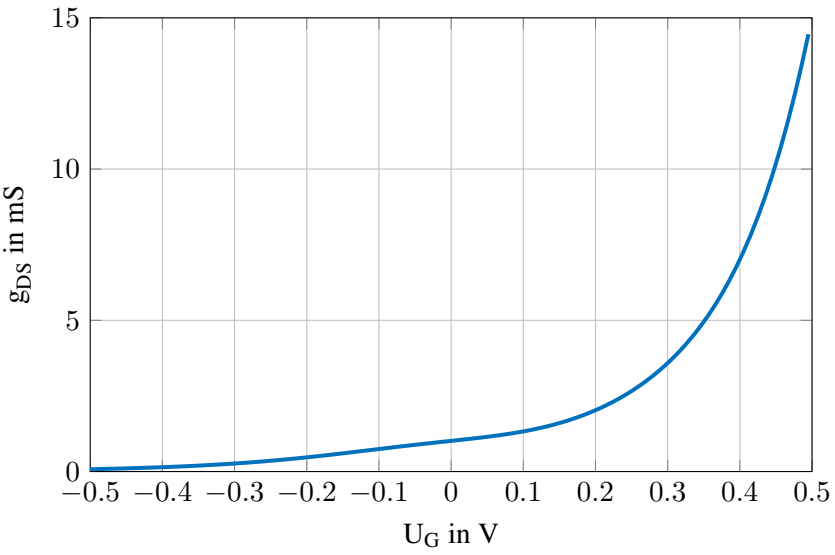

Figure 3.8: Simulation of g_{DS} versus U_{G}. The data was extracted from a DC simulation of a single mHEMT by differentiation of I_{D} w.r.t. U_{D} at $U_{\mathrm{G}} = 0\,\mathrm{V}$.

A small decrease in the accepted LO power is sufficient for G_c to drop significantly. This condition is met for a larger interval of phase differences so the dips become wider.

Drain Node of the FET

Looking at the drain node of the FET, another interesting behavior can be observed. Usually, the resistive mixer has no drain bias. The DC component of the IF signal, however, is found to be cosine-shaped, varying between $-0.2\,\mathrm{V}$ and $0.6\,\mathrm{V}$ (Fig. 3.4(c)). This can be understood as a self-biasing of the drain. Comparing the DC IF signal with G_c, it can be seen that the dips of G_c occur at the maxima of the DC IF-signal for all values for τ.

This leads to the second assumption for the occurrence of the dips. The cosine of the DC IF signal can be explained as follows. In addition to the desired mixing process of the RF and LO signal, the LO-RF signal at the drain is also mixed with the LO signal, where both signals have the same frequency ω_{LO}. The IF signal for this process is calculated as

$$s_{\mathrm{LO}}(t) \cdot s_{\mathrm{LORF}}(t) = a(t)\cos((\omega_{\mathrm{LO}} + \omega_{\mathrm{LO}})t + \Delta\varphi) + a(t)\cos((\omega_{\mathrm{LO}} - \omega_{\mathrm{LO}})t - \Delta\varphi) \tag{3.6}$$

$$= a(t)\cos(2\omega_{\mathrm{LO}}t + \Delta\varphi) + a(t)\cos(\Delta\varphi) \tag{3.7}$$

$$\text{with } a(t) = \frac{1}{2}a_{\mathrm{LORF}} \cdot a_{\mathrm{LO}}.$$

The second term is the DC component of the IF signal. The DC component varies with the cosine of the phase difference or $2\pi f\tau$. This confirms that the position of the dips corresponds to a certain phase difference of the LO and LO-RF signal. Note, however, that it is difficult to associate the presence of this phase difference $\Delta\phi$ with a certain point in the physical mixer layout.

As a consequence of the self-biasing effect of the drain, the FET mixer might operate outside its optimum point, causing a drop in the conversion efficiency.

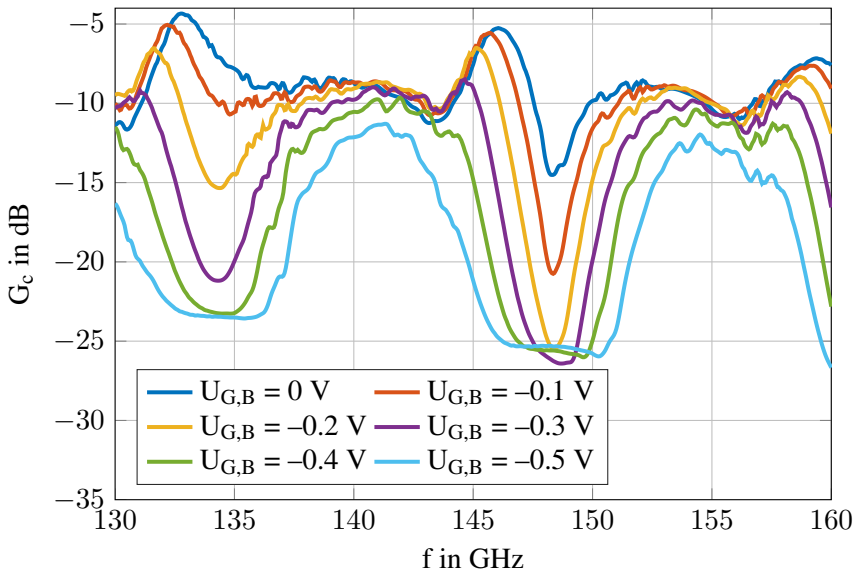

Figure 3.9: Simulation of the FET resistive mixer with different gate-bias voltages to investigate their impact on G_c.

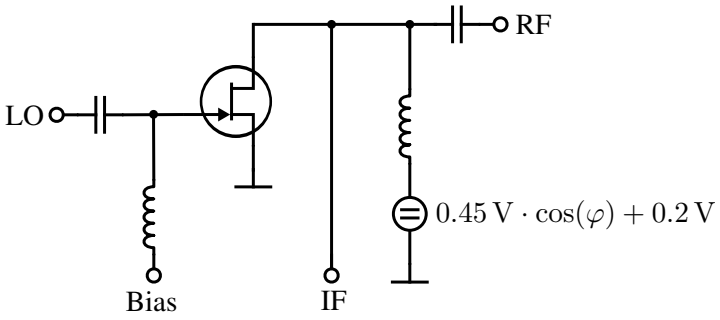

Figure 3.10: Simulation setup of the FET resistive mixer with an additional drain bias. At the drain, no LO-RF signal is applied to analyze the isolated impact of the self-biasing effect.

In the light of both assumptions, the question is raised whether the self-biasing effect is the cause or the consequence of the dips in G_c. To answer this question, another simulation is performed. To analyze the isolated impact of the DC component at the drain, no LO-RF signal is applied to the drain. The FET is biased with a DC voltage which changes its amplitude with $0.45\,\mathrm{V} \cdot \cos(\varphi) + 0.2\,\mathrm{V}$. φ is swept between 0 and 360° of 5°. The setup is shown in Fig. 3.10. Fig. 3.11 shows G_c over the frequency with different drain bias voltages. The resulting curves lie between the two present envelopes. It can be noticed that the drain bias alone does not lead to dips in G_c. This leads to the conclusion that the self biased drain is a consequence of the dips and not the cause.

Conclusion

Analyses of the FET at the gate and drain node have led to two assumptions regarding the occurrence of the dips in G_c. There are two quantities which correlate with the dips.

1. The accepted LO power has its minima at the same frequencies as the dips in G_c. This has

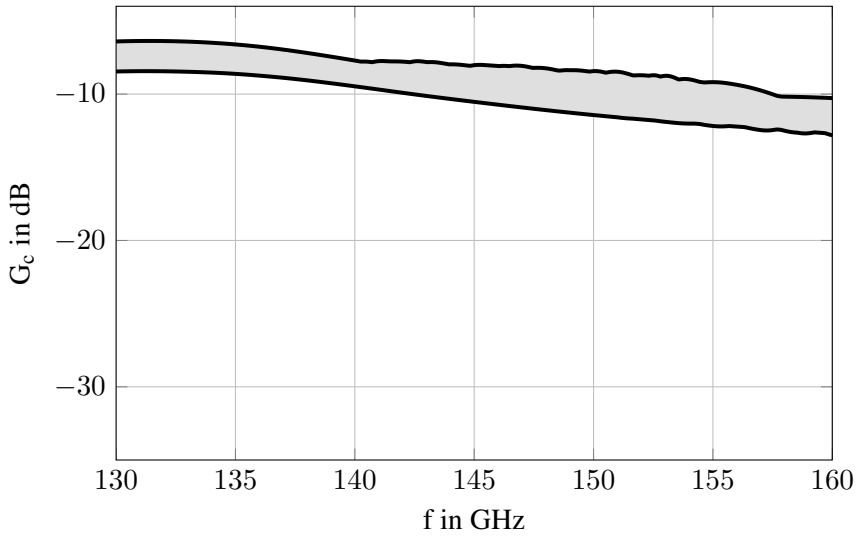

Figure 3.11: Simulation results with an additional drain bias without the LO-RF signal at the drain. The resulting curves for bias voltages between -0.25 and $0.65\,\mathrm{V}$ lie between the two envelopes.

led to the first assumption that the LO-RF signal couples to the gate via C_{GD} and destructive interference between the LO and LO-RF signal occurs. Thus, the accepted LO power is not high enough and the mixing process becomes very inefficient. The simulation of the mixer with different ratios of P_{LO}/ P_{LORF} supports this first assumption.

2. The drain bias has its maxima at the same frequencies as the dips in G_c. Based on this observation, the second assumption is that the FET is operated outside its operating point. A simulation using an externally applied bias has shown that the self-biasing effect is not the cause but rather the consequence of the dips.

To quantify the first assumption in a more systematic way, an analytic model is developed in the next section. With the ADS simulation it is not possible to analyze the isolated influence of e.g. the capacitance C_{GD} because of the complex structure of the provided IAF transistor models. The derivation and solution of this analytic model is explained in the next section.

3.2 Analytic Model

The starting point of the analytic model is the textbook calculation of G_c based on the standard small signal model of the FET resistive mixer (Fig. 2.5) explained in chapter 2.

Two approaches of different complexity are then developed to incorporate the additional LO-RF path into the calculation of G_c. The first model directly includes the LO-RF path in the expression for U_{G} and the second model modifies the equivalent circuit in a suitable way.

The following parameters are chosen as input variables of the models: the effective delay τ of the LO-RF signal w.r.t. to the LO signal, the gate-drain capacitance C_{GD}, the voltage amplitudes of the LO and LO-RF signals $\hat{U}_{\mathrm{LO}}$ and $\hat{U}_{\mathrm{LO,RF}}$, respectively, and the gate bias $U_{\mathrm{G,B}}$. By solving the analytic

model, the impacts of the different parameters can be investigated separately from each other and the behavior of the mixer can be understood in detail.

The two approaches to derive the analytic models are presented in the following.

3.2.1 First Model: Direct Modification of the Gate Voltage

The easiest way to include the delayed LO-RF signal is to directly modify the equation of g_{DS} in the small signal equivalent circuit (Fig. 2.5). g_{DS} depends on the gate voltage

$$U_{\mathrm{G}} = \underbrace{U_{\mathrm{B}} + \hat{U}_{\mathrm{LO}} \cos(\omega_{\mathrm{LO}} t)}_{\text{as in Eq. 2.10}} + \underbrace{\alpha \hat{U}_{\mathrm{LORF}} \cos(\omega_{\mathrm{LO}} t + \varphi)}_{\text{modified part}} . \tag{3.8}$$

Besides the desired bias and LO voltage, the LO-RF voltage is also present at the gate node. To take the effect of the parasitic capacitance C_{GD} into account, a dimensionless parameter α is introduced to describe the coupling of the LO-RF signal from the drain to the gate. The phase difference of the LO and LO-RF signal is described by φ.

Linear Channel Conductance

A first approximation to describe g_{DS} in its simplest form is the linear relationship

$$\begin{aligned} g_{\mathrm{DS}}(U_{\mathrm{G}}) &= \gamma \cdot U_{\mathrm{G}} \\ &= \gamma \cdot \left(U_{\mathrm{B}} + \hat{U}_{\mathrm{LO}} \cos(\omega_{\mathrm{LO}} t) + \alpha \hat{U}_{\mathrm{LORF}} \cos(\omega_{\mathrm{LO}} t + \varphi) \right) \end{aligned} \tag{3.9}$$

with a proportionality constant γ.

As described in chapter 2, g_{DS} can be rewritten in the form of a Fourier series. With the trigonometric identity

$$\cos(\omega_{\mathrm{LO}} t + \varphi) = \cos(\omega_{\mathrm{LO}} t) \cos(\varphi) - \sin(\omega_{\mathrm{LO}} t) \sin(\varphi) \tag{3.10}$$

Eq. 3.9 results in

$$g_{\mathrm{DS}} = \gamma U_{\mathrm{B}} + \gamma \cos(\omega_{\mathrm{LO}} t) \left(\hat{U}_{\mathrm{LO}} + \alpha \hat{U}_{\mathrm{LORF}} \cos(\varphi) \right) + \gamma \sin(\omega_{\mathrm{LO}} t) \left(-\alpha \hat{U}_{\mathrm{LO}} \sin(\varphi) \right) . \tag{3.11}$$

Invoking Euler's formula yields

$$\begin{aligned} g_{\mathrm{DS}} = \underbrace{\gamma U_{\mathrm{B}}}_{=g_{\mathrm{DS}}^{0}} &+ e^{j\omega_{\mathrm{LO}} t} \underbrace{\left(\frac{1}{2} \gamma \hat{U}_{\mathrm{LO}} + \frac{1}{2} \gamma \alpha \hat{U}_{\mathrm{LORF}} \cos(\varphi) - \frac{1}{2j} \gamma \alpha \hat{U}_{\mathrm{LORF}} \sin(\varphi) \right)}_{=g_{\mathrm{DS}}^{1}} \\ &+ e^{-j\omega_{\mathrm{LO}} t} \underbrace{\left(\frac{1}{2} \gamma \hat{U}_{\mathrm{LO}} + \frac{1}{2} \gamma \alpha \hat{U}_{\mathrm{LORF}} \cos(\varphi) + \frac{1}{2j} \gamma \alpha \hat{U}_{\mathrm{LORF}} \sin(\varphi) \right)}_{=g_{\mathrm{DS}}^{-1}} \end{aligned} \tag{3.12}$$

Table 3.2: Chosen parameters for the evaluation of the first model.

Description	Symbol	Number	Unit
Amplitude of LO voltage	$\hat{U}_{\mathrm{LO}}$	0.35	V
Amplitude of LO-RF voltage	$\hat{U}_{\mathrm{LORF}}$	0.2	V
Gate bias	$\hat{U}_{\mathrm{B}}$	0.5	V
Proportionality constant	γ	1	$\mathrm{S\,V^{-1}}$
Delay	τ	71	ps
Coupling factor	α	0.7	

and the Fourier coefficients can directly be extracted as

$$g_{\mathrm{DS}}^{0} = \gamma U_{\mathrm{B}} \tag{3.13}$$

$$g_{\mathrm{DS}}^{1} = \frac{1}{2}\gamma\hat{U}_{\mathrm{LO}} + \frac{1}{2}\gamma\alpha\hat{U}_{\mathrm{LORF}}\cos(\varphi) - \frac{1}{2j}\gamma\alpha\hat{U}_{\mathrm{LORF}}\sin(\varphi) = \left(g_{\mathrm{DS}}^{-1}\right)^{*}. \tag{3.14}$$

Inserting g_{DS}^{0} and g_{DS}^{1} in Eq. 2.18, the conversion gain is obtained:

$$G_c = \frac{1 - \sqrt{1 - \left|\frac{\hat{U}_{\mathrm{LO}} + \alpha\hat{U}_{\mathrm{LORF}}\cos(\varphi) - \frac{1}{j}\alpha\hat{U}_{\mathrm{LORF}}\sin(\varphi)}{2U_{\mathrm{B}}}\right|^2}}{1 + \sqrt{1 - \left|\frac{\hat{U}_{\mathrm{LO}} + \alpha\hat{U}_{\mathrm{LORF}}\cos(\varphi) - \frac{1}{j}\alpha\hat{U}_{\mathrm{LORF}}\sin(\varphi)}{2U_{\mathrm{B}}}\right|^2}} \tag{3.15}$$

Note that with $\varphi = 2\pi f\tau$ as discussed before, G_c is independent of γ. In this model, the parameter U_{B} does not represent the real bias voltage, instead it keeps the modulation of g_{DS} in the ohmic region, i.e. $g_{\mathrm{DS}} > 0$. With the parameters in Tab. 3.2 the conversion gain over frequency is plotted in Fig. 3.12. It shows two dips similar to those in the measurements and ADS simulation. The scaling of the y-axis directly depends on the arbitrary choice of U_{B} and is not representative of the real values.

Exponential Channel Conductance

In order to map the bias voltage and hence g_{DS} better to reality, an exponential fit of the characteristic curve of g_{DS} as seen in Fig. 3.13 is performed based on an ADS simulation. The simple exponential form

$$g_{\mathrm{DS}} = Ae^{BU_{\mathrm{G}}} \tag{3.16}$$

with $A = 1.67\,\mathrm{mS}$ and $B = 6.140\,91\,\frac{1}{\mathrm{V}}$ is in good agreement with the simulated characteristic and yields an analytical expression for G_c that can be handled without a computer. Inserting Eq. 3.8

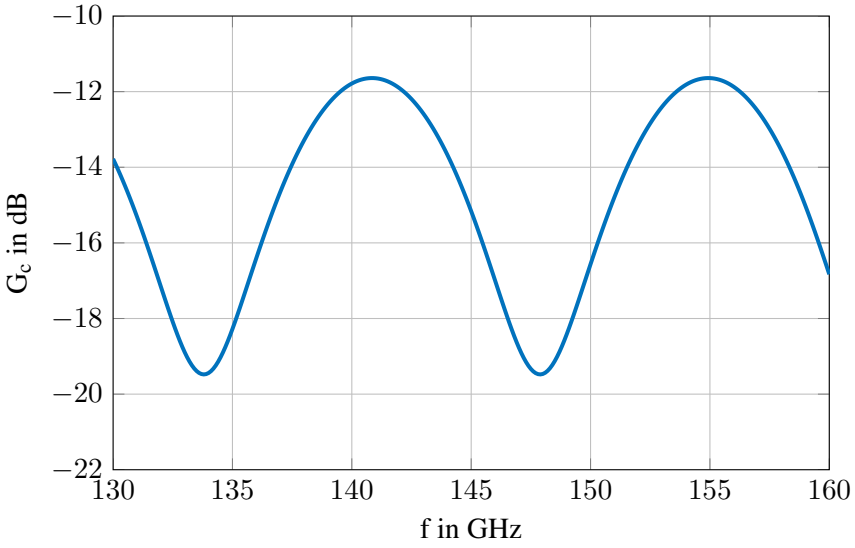

Figure 3.12: Results of the first model with linear channel conductance. As in the ADS simulation, the separation of the dips is 14 GHz. The y-axis depends on the arbitrary choice of U_B and thus is not quantitative.

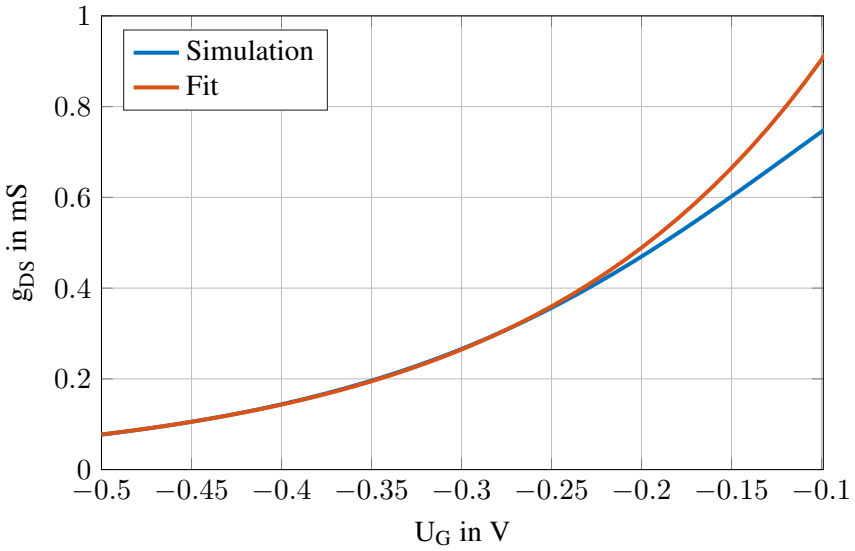

Figure 3.13: Exponential fit for $g_{DS} = Ae^{BU_B}$ based on the DC simulation of a single mHEMT.

in 3.16 results in

$$g_{\mathrm{DS}} = Ae^{BU_{\mathrm{B}}} \exp\Big(\cos(\omega_{\mathrm{LO}}t) \underbrace{\Big(B\hat{U}_{\mathrm{LO}} + B\hat{U}_{\mathrm{LORF}}\alpha\cos(\varphi)\Big)}_{=:\beta} - \sin(\omega_{\mathrm{LO}}t) \underbrace{\Big(B\hat{U}_{\mathrm{LORF}}\alpha\sin(\varphi)\Big)}_{=:\gamma} \Big)$$
$$= Ae^{BU_{\mathrm{B}}} \exp\big(\beta\cos(\omega_{\mathrm{LO}}t) - \gamma\sin(\omega_{\mathrm{LO}}t)\big)\,. \tag{3.17}$$

To evaluate the integral for the Fourier coefficients, Eq. 3.17 has to be transformed in the following form

$$g_{\mathrm{DS}} = Ae^{BU_{\mathrm{B}}} e^{C_1\cos(\omega_{\mathrm{LO}}t+C_2)} \tag{3.18}$$
$$= Ae^{BU_{\mathrm{B}}} e^{C_1\cos(\omega_{\mathrm{LO}}t)\cos(C_2) - C_1\sin(\omega_{\mathrm{LO}}t)\sin(C_2)} \tag{3.19}$$

with the coefficients

$$C_1 := \sqrt{\beta^2+\gamma^2} \tag{3.20}$$
$$C_2 := \arctan\left(\frac{\gamma}{\beta}\right). \tag{3.21}$$

The Fourier coefficients are calculated as

$$g_{\mathrm{DS}}^{(n)} = \frac{Ae^{BU_{\mathrm{B}}}}{2\pi} \int_{-\pi}^{\pi} e^{C_1\cos(\omega_{\mathrm{LO}}t+C_2)} \cdot e^{-j\omega_{\mathrm{LO}}nt} d\left(\omega_{\mathrm{LO}}t\right). \tag{3.22}$$

Substitution of $\omega_{\mathrm{LO}}\tilde{t} = \omega_{\mathrm{LO}}t + C_2$ and exploiting the 2π-periodicity of the integrand results in

$$g_{\mathrm{DS}}^{(n)} = \frac{Ae^{BU_{\mathrm{B}}}}{2\pi} \int_{-\pi}^{\pi} e^{C_1\cos(\omega_{\mathrm{LO}}\tilde{t})} \cdot e^{-jn(\omega_{\mathrm{LO}}\tilde{t}-C_2)} d\left(\omega_{\mathrm{LO}}\tilde{t}\right)$$
$$= e^{jnC_2}\frac{Ae^{BU_{\mathrm{B}}}}{2\pi} \int_{-\pi}^{\pi} e^{C_1\cos(\omega_{\mathrm{LO}}\tilde{t})} \cdot e^{-jn(\omega_{\mathrm{LO}}\tilde{t})} d\left(\omega_{\mathrm{LO}}\tilde{t}\right).$$

Only the real part is considered because $e^{C_1\cos(\omega\tilde{t})} \cdot \sin(n\omega_{\mathrm{LO}}\tilde{t})$ is uneven and its integral vanishes, which leads to

$$g_{\mathrm{DS}}^{(n)} = e^{jnC_2}\frac{Ae^{BU_{\mathrm{B}}}}{\pi} \int_{0}^{\pi} e^{C_1\cos(\omega_{\mathrm{LO}}\tilde{t})} \cdot \cos\left(n\omega_{\mathrm{LO}}\tilde{t}\right) d\left(\omega_{\mathrm{LO}}\tilde{t}\right). \tag{3.23}$$

With the modified Bessel function for $n \in \mathbb{N}$

$$I_n(x) := \frac{1}{\pi}\int_0^{\pi} e^{x\cos(\theta)}\cos(n\theta)d\theta - \underbrace{\frac{\sin(n\pi)}{\pi}\int_0^{\infty} e^{-x\cosh(t)-nt}dt}_{=0,\text{ because } n \text{ is an integer}} \tag{3.24}$$

the final result is

$$g_{\mathrm{DS}}^{(n)} = Ae^{BU_{\mathrm{B}}} e^{jnC_2} \cdot I_n(C_1) \tag{3.25}$$

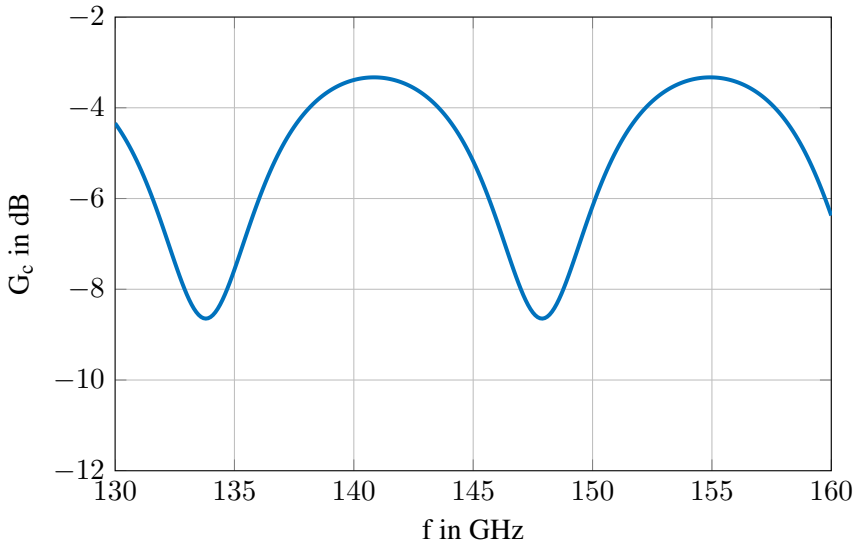

Figure 3.14: Results of the first model with exponential channel conductance. Similar to the ADS simulation results and the approximation with the linear channel conductance, the distance of the dips is 14 GHz. The scale of the y-axis is fixed, because G_c is independent of U_B.

The first two Fourier coefficients are

$$g_\mathrm{DS}^{(0)} = Ae^{BU_\mathrm{B}} I_0(C_1) \tag{3.26}$$

$$g_\mathrm{DS}^{(1)} = Ae^{BU_\mathrm{B}} e^{jC_2} I_1(C_1) \tag{3.27}$$

which determine the conversion gain as

$$G_c = \frac{1 - \sqrt{1 - \left|\frac{I_0(C_1)}{I_1(C_1)}\right|^2}}{1 + \sqrt{1 - \left|\frac{I_0(C_1)}{I_1(C_1)}\right|^2}}. \tag{3.28}$$

With the same parameters as for the linear characteristic, G_c is plotted over frequency in Fig. 3.14. As an interesting first observation, G_c is independent of U_B when an exponential form is assumed for g_DS. Therefore, the scaling of the y-axis is fixed. Apart from the different scaling of the y-axis, the curves for G_c are very similar for the linear and exponential case. The dips occur at the same frequencies and the form is also very similar.

To understand the impact of the coupling factor α, which represents the source of the problem in this model, Fig. 3.15 shows G_c with $\alpha = 0$, $\alpha = 0.5$ and $\alpha = 1$. The higher α the more of the LO-RF signal couples over and the deeper the dips become.

3.2.2 Second Model: Realistic Equivalent Circuit

To account for the effect of the capacitance C_GD in a direct manner, the standard small signal equivalent circuit of a FET resistive mixer is modified. The large signal equivalent circuit as it can

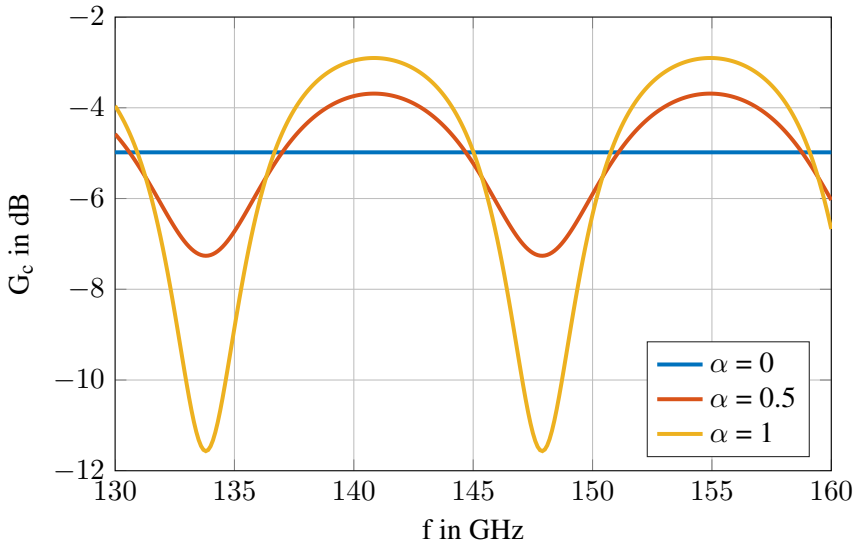

Figure 3.15: Conversion gain extracted from the first model with exponential channel conductance with different coupling factors: (a) $\alpha = 0$, (b) $\alpha = 0.5$ and (c) $\alpha = 1$. The higher the coupling factor, the deeper the dips become.

be found in literature [ST71] is shown in Fig. 3.16(a). The LO and RF signals are coupled via ideal transformers. The LO and bias voltages are applied to the gate via a bias-tee. The capacitance C blocks the DC voltage and the inductance L blocks the AC voltage. Beside the FET transistor itself, the parasitic capacitances C_{GD} and C_{GS} are included. At the drain terminal the RF signal is applied. As a result of the mixing process, the IF signal is generated.

To calculate G_c, the classic equivalent circuit is simplified and the additional LO-RF signal is included as shown in Fig. 3.16(b). The bias voltage is included in u_{LO}. The parasitic capacitance C_{GS} is absorbed in the complex gate impedance Z_{G}. The FET channel is reduced to its drain/source conductance g_{DS}. The LO-RF signal is also applied to the drain.

In a first step, the gate voltage is calculated. To that end, the circuit in Fig. 3.16(b) is further simplified (Fig. 3.17). The RF and IF signals are neglected because they make no contribution at the LO frequency. For g_{DS} only the zeroth Fourier coefficient is considered because it has the largest impact on the gate voltage. U_{G} is calculated as the superposition

$$U_{\mathrm{G}} = \underline{\psi}_1 \left(g_{\mathrm{DS}}^0\right) \hat{U}_{\mathrm{LO}} + \psi_2 \left(g_{\mathrm{DS}}^0\right) \hat{U}_{\mathrm{LORF}} \tag{3.29}$$

$$= \underline{\hat{U}}_{\mathrm{G}} e^{j\varphi_{\mathrm{G}}}. \tag{3.30}$$

The first part of the equation is calculated by shorting the LO-RF source which results in

$$\psi_1 = \frac{U_{\mathrm{G}}}{U_{\mathrm{LO}}} = \frac{\underline{Z}_1}{\underline{Z}_{\mathrm{ges},1}} \tag{3.31}$$

with

$$\underline{Z}_1 = \underline{Z}_{\mathrm{G}} \parallel \left(\frac{1}{j\omega C_{\mathrm{GD}}} + \left(\underline{Z}_{\mathrm{i,LORF}} \parallel R_{\mathrm{DS}}^0\right) \right) \tag{3.32}$$

$$\underline{Z}_{\mathrm{ges1}} = \underline{Z}_{\mathrm{i,LO}} + \underline{Z}_1. \tag{3.33}$$

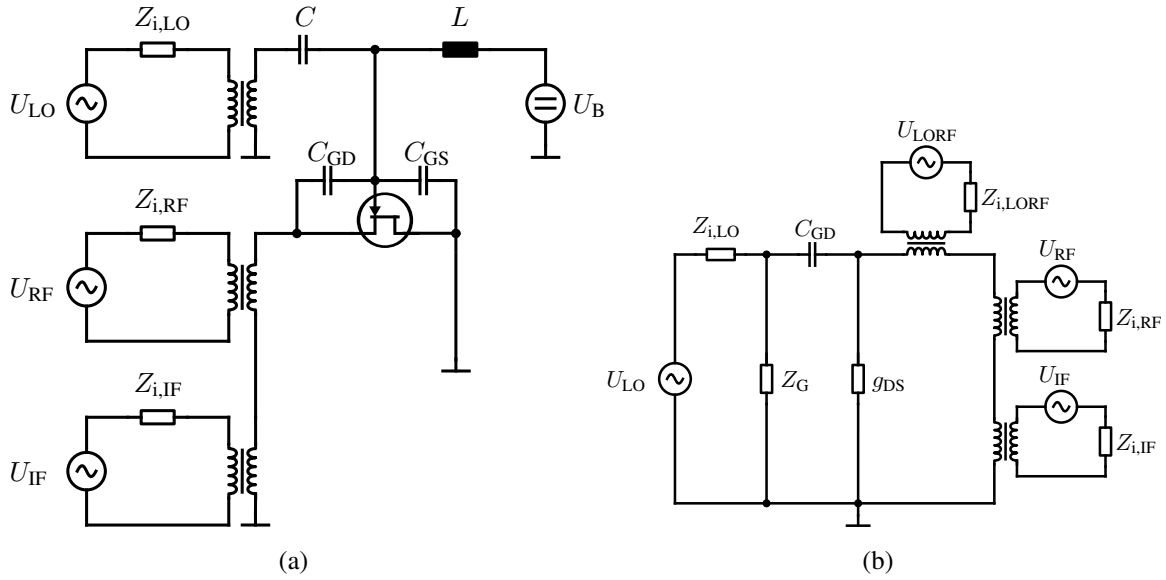

Figure 3.16: Large signal equivalent circuit of a FET resistive mixer, (a) according to literature, (b) modified and simplified to consider the additional LO-RF path.

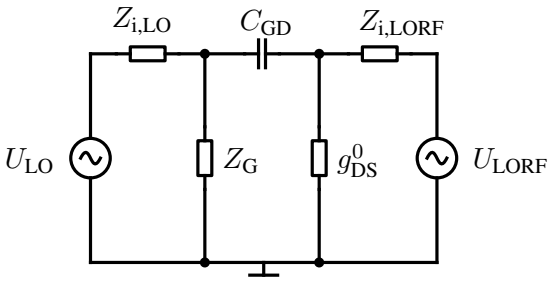

Figure 3.17: Modified circuit to calculate U_{G} in a first step. At the gate node, only the LO and LO-RF signal make a contribution at the LO frequency. For simplicity, only g^0_{DS} is considered because the other Fourier coefficients of g_{DS} have a negligible impact on U_{G}.

The second part of the equation is calculated in the same way by shorting the LO source and is given by

$$\psi_2 = \frac{U_\mathrm{G}}{U_\mathrm{LORF}} = \frac{U_\mathrm{G}}{U_\mathrm{s}} \cdot \frac{U_\mathrm{s}}{U_\mathrm{LORF}} = \frac{\underline{Z}_1}{\underline{Z}_2} \cdot \frac{\underline{Z}_3}{\underline{Z}_4} \tag{3.34}$$

with

$$\underline{Z}_1 = \underline{Z}_\mathrm{G} \parallel \underline{Z}_\mathrm{i,LO} \tag{3.35}$$

$$\underline{Z}_2 = \frac{1}{j\omega C_\mathrm{GD}} + \underline{Z}_1 \tag{3.36}$$

$$\underline{Z}_3 = R^0_\mathrm{DS} \parallel \underline{Z}_2 \tag{3.37}$$

$$\underline{Z}_4 = \underline{Z}_\mathrm{i,LORF} + \underline{Z}_3. \tag{3.38}$$

The second step is to calculate the Fourier coefficients in analogy to chapter 3.2.1 based on the small signal equivalent circuit in Fig. 2.5. In the process, the internal impedance $\underline{Z}_\mathrm{i,LORF}$ and $\underline{Z}_\mathrm{i,LO}$ are transferred outside of the two port network under the assumption of perfectly matched ports.

Linear Channel Conductance

The assumption of a linear form for g_DS results in

$$g_\mathrm{DS,linear} = \gamma \left(U_\mathrm{G}(\omega_\mathrm{LO} t) + U_\mathrm{B} \right) \tag{3.39}$$

$$= \gamma \left(U_\mathrm{B} + \psi_1 \hat{U}_\mathrm{LO} + \psi_2 \hat{U}_\mathrm{LORF} e^{j\varphi} \right). \tag{3.40}$$

By using Euler's formula and the trigonometric identity in Eq. 3.10, this can be written as

$$\begin{aligned} g_\mathrm{DS,linear} = \gamma U_\mathrm{B} &+ \underbrace{\cos(\omega_\mathrm{LO} t) \left(\gamma \psi_1 \hat{U}_\mathrm{LO} + \gamma \psi_2 \hat{U}_\mathrm{LORF} \cos(\varphi) \right)}_{=a} \\ &+ \underbrace{\sin(\omega_\mathrm{LO} t) \left(\gamma \psi_2 \hat{U}_\mathrm{LORF} \sin(\varphi) \right)}_{=b} \end{aligned} \tag{3.41}$$

$$= \gamma U_\mathrm{B} + \frac{a - jb}{2} e^{j\omega_\mathrm{LO} t} + \frac{a + jb}{2} e^{-j\omega_\mathrm{LO} t}. \tag{3.42}$$

This results in the Fourier coefficients

$$g^0_\mathrm{DS} = \gamma U_\mathrm{B} \tag{3.43}$$

$$g^1_\mathrm{DS} = \frac{1}{2} \gamma \left(\psi_1 \hat{U}_\mathrm{LO} + \psi_2 \hat{U}_\mathrm{LORF} \cos(\varphi) - j \psi_2 \hat{U}_\mathrm{LORF} \sin(\varphi) \right) \tag{3.44}$$

and, consequently, the conversion gain

$$G_c = \frac{1 - \sqrt{1 - \left| \frac{\psi_1 \hat{U}_\mathrm{LO} + \psi_2 \hat{U}_\mathrm{LORF} \cos(\varphi) - j \psi_2 \hat{U}_\mathrm{LORF} \sin(\varphi)}{2 U_\mathrm{B}} \right|^2}}{1 + \sqrt{1 - \left| \frac{\psi_1 \hat{U}_\mathrm{LO} + \psi_2 \hat{U}_\mathrm{LORF} \cos(\varphi) - j \psi_2 \hat{U}_\mathrm{LORF} \sin(\varphi)}{2 U_\mathrm{B}} \right|^2}} \tag{3.45}$$

Table 3.3: Chosen parameters for the evaluation of the second model.

Description	Symbol	Number	Unit
Amplitude of LO voltage	$\hat{U}_{\mathrm{LO}}$	0.08	V
Amplitude of LO-RF voltage	$\hat{U}_{\mathrm{LORF}}$	0.1	V
Gate bias	$\hat{U}_{\mathrm{B}}$	-0.2	V
Delay	τ	71	ps
Gate-Drain capacitance	C_{GD}	10	fF
Gate impedance	$\underline{Z}_{\mathrm{G}}$	30	Ω
Internal impedance of LO-RF source	$\underline{Z}_{\mathrm{i,LORF}}$	$15.92 + 11.41\mathrm{j}$	Ω
Internal impedance of RF source	$\underline{Z}_{\mathrm{i,LO}}$	$12.96 + 1.5\mathrm{j}$	Ω

which is plotted in Fig. 3.18 based on the parameters in Tab. 3.3.

Again, U_{B} does not represent a realistic bias voltage. Referring to Fig. 3.17, $\underline{Z}_{\mathrm{i,LO}}$ and $\underline{Z}_{\mathrm{i,LORF}}$ are calculated so that they are matched to the corresponding load impedance at the center frequency.

Exponential Channel Conductance

Assuming the more realistic exponential form (3.16) for g_{DS}, inserting (3.30) in (3.16) leads to the Fourier coefficients

$$g_{\mathrm{DS}}^{(n)} = \frac{A}{2\pi} \int_0^{2\pi} e^{B\left(\hat{U}_{\mathrm{G}} \cos(\omega_{\mathrm{LO}} t + \varphi_{\mathrm{G}}) + U_{\mathrm{B}}\right)} e^{-j\omega_{\mathrm{LO}} n t} d(\omega_{\mathrm{LO}} t) \tag{3.46}$$

where the amplitude $\hat{U}_{\mathrm{G}}$ is calculated from Eq. 3.30 using Matlab. Solving the integral similar to the previous calculations, this yields

$$g_{\mathrm{DS}}^{(n)} = A e^{BU_{\mathrm{B}}} e^{jn\varphi_G} I_n(B\hat{U}_{\mathrm{G}}). \tag{3.47}$$

The first two Fourier coefficients are

$$g_{\mathrm{DS}}^{0} = A e^{BU_{\mathrm{B}}} I_0\left(B\hat{U}_{\mathrm{G}}\right) \tag{3.48}$$

$$g_{\mathrm{DS}}^{1} = A e^{BU_{\mathrm{B}}} e^{j\varphi_{\mathrm{G}}} I_1\left(B\hat{U}_{\mathrm{G}}\right). \tag{3.49}$$

The zeroth Fourier coefficient depends on $\hat{U}_G$ which depends on the zeroth Fourier coefficient itself. Therefore, a fixed-point iteration is used in order to numerically evaluate the expression. The resulting conversion gain

$$G_c = \frac{1 - \sqrt{1 - \left|\frac{e^{j\varphi_{\mathrm{G}}} I_1\left(B\hat{U}_{\mathrm{G}}\right)}{I_0\left(B\hat{U}_{\mathrm{G}}\right)}\right|^2}}{1 + \sqrt{1 - \left|\frac{e^{j\varphi_{\mathrm{G}}} I_1\left(B\hat{U}_{\mathrm{G}}\right)}{I_0\left(B\hat{U}_{\mathrm{G}}\right)}\right|^2}} \tag{3.50}$$

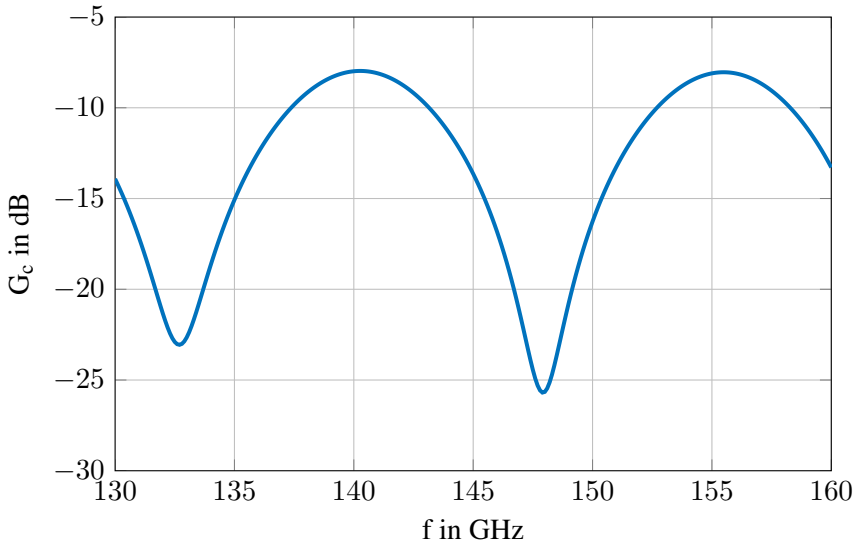

Figure 3.18: Result of the second model with linear channel conductance directly including the value of the gate-drain capacitance. Again, two dips can be observed with a frequency separation of around 14 GHz. As in Fig. 3.12, G_c is not captured quantitatively as it depends on U_B in a non-physical way.

is plotted in Fig. 3.19. In this model, the conversion gain depends on the bias voltage via $\hat{U}_\mathrm{G}$ and therefore indirectly influences the voltage at the gate node. In comparison to the linear characteristic of g_DS, this influence of U_B covers the realistic case best. Again, the shapes of the curves are similar for the linear and the exponential characteristic.

To conclude the quantification of the problem by the second developed model with exponential channel conductance, the impact of the input parameters on the dips in the conversion gain are summarized.

- Delay τ

  Fig. 3.20 shows the influence of effective delays of $\tau = 0, 71$ and $142\,\mathrm{ps}$. The separation of the dips becomes smaller when the delay of the LO-RF signal is higher. This confirms the results of the ADS simulation.

- Voltage ratio $\hat{U}_\mathrm{LO}/\hat{U}_\mathrm{LORF}$

  The identified influence of the voltage ratio $\hat{U}_\mathrm{LO}/\hat{U}_\mathrm{LORF}$ on G_c is plotted in Fig. 3.22(a) with the corresponding gate voltage shown in Fig. 3.22(b). When doubling the voltage ratio, the mean voltage at the gate is higher and the depth of the dips of G_c become smaller.

  This supports the first assumption regarding the cause of the dips. If $\hat{U}_\mathrm{LORF}$ is higher, more of the LO-RF signal is present at the gate and the influence of destructive interference is higher. This results in more pronounced dips.

- Capacitance C_GD

  Fig. 3.21 shows that no dips would occur in the absence of C_GD. In comparison to the simulation, it is possible to investigate the occurrence of the dips only in dependence of C_GD

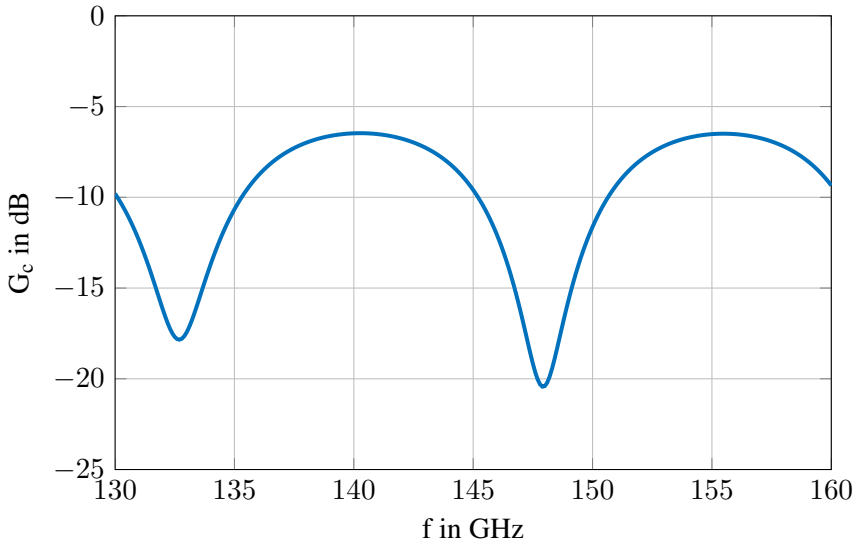

Figure 3.19: Result of the second model with exponential channel conductance. The position and shape of the dips agree with the previous results. This model directly includes the value of the gate-drain capacitance and describes the influence of U_B more realistically than in the other cases.

by leaving the other parameters unchanged. The result of the analytic model strengthens the first assumption made in the previous section that the dips are caused by the coupling of the LO-RF signal over the parasitic capacitance C_{GD}.

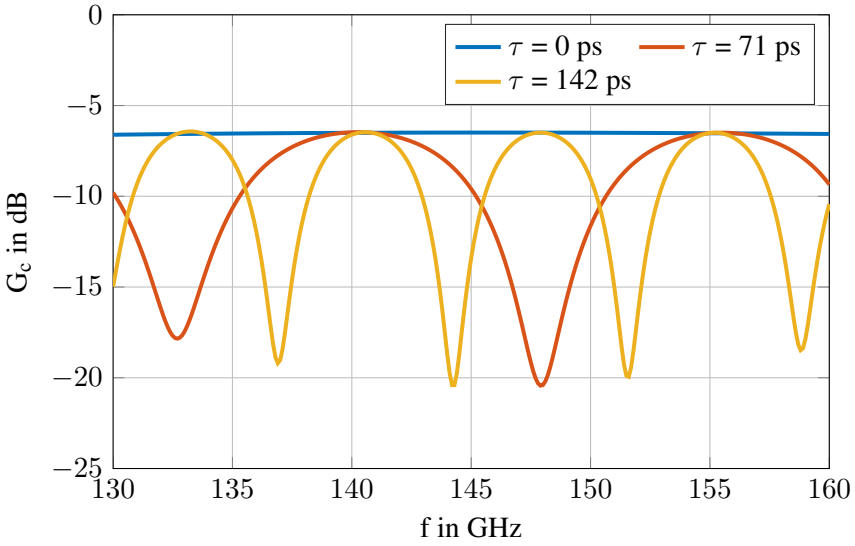

Figure 3.20: Investigation of the effect of different delays on the dips in G_c, based on the second model with exponential channel conductance, (a) $\tau = 0\,\mathrm{ps}$, (b) $\tau = 71\,\mathrm{ps}$, (c) $\tau = 142\,\mathrm{ps}$.

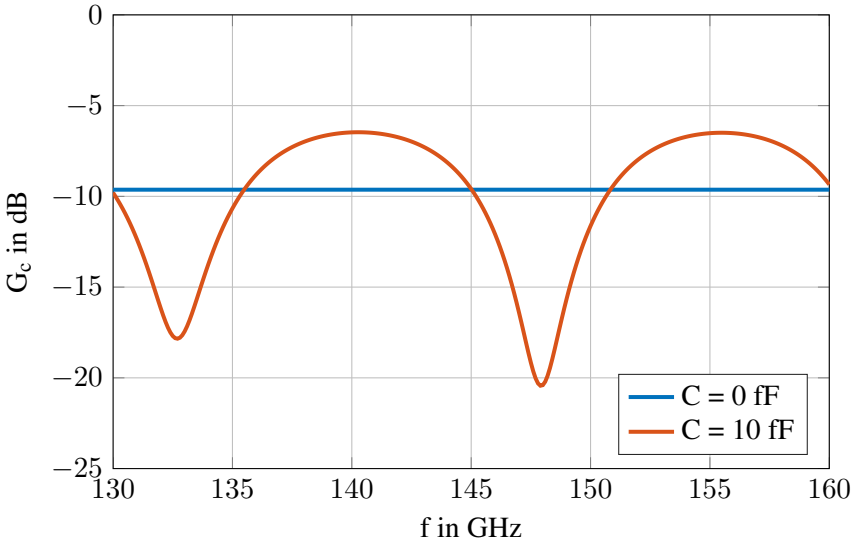

Figure 3.21: Investigation of the influence of the gate-drain capacitance on the dips in G_c, based on the second model with exponential channel conductance, (a) $C = 0\,\mathrm{fF}$, (b) $C = 10\,\mathrm{fF}$.

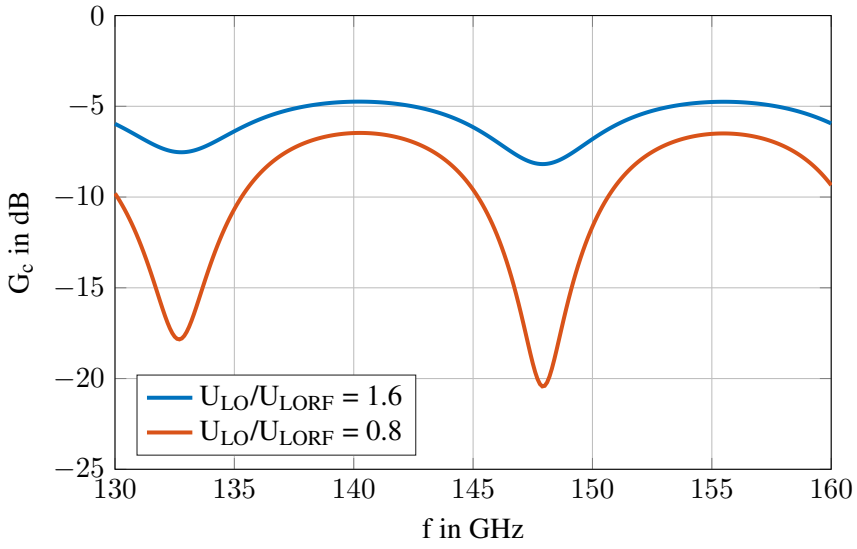

(a)

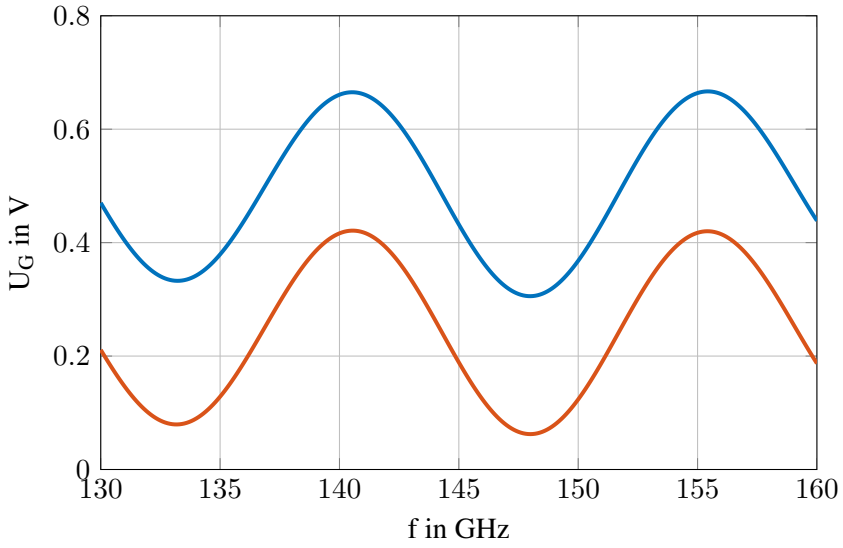

(b)

Figure 3.22: Influence of different ratios of $\hat{U}_{\mathrm{LO}}/\hat{U}_{\mathrm{LORF}}$ on the dips in G_c and the corresponding gate voltages, based on the second model with exponential channel conductance, with $\hat{U}_{\mathrm{LORF}} = 0.1\,\mathrm{V}$ and $\hat{U}_{\mathrm{LO}} = 0.08\,\mathrm{V}$ or $\hat{U}_{\mathrm{LO}} = 0.16\,\mathrm{V}$. The color coding of the curves is the same for both subfigures.

4 Measurement of the Individual Resistive Mixer

The assumption regarding the additional LO-RF signal causing the dips in the conversion gain should be quantified by directly applying the LO-RF signal at the resistive mixer, i.e. using the measurement system to present a precisely controlled LO feedback path to the mixer. In the measurement it should be possible to adjust

- the power levels of the LO and LO-RF signal and
- the relative phase of the LO and LO-RF signal on the chip level, individually for each frequency.

Note that it is possible to realize a delay τ between the LO and LO-RF signal by varying the adjustable relative phase linearly with the frequency according to $\Delta\varphi = 2\pi f\tau$ in addition to a frequency independent global phase shift φ_0.

In the first section of this chapter the measurement setup is explained. The second section covers the performed measurement sequences and their analysis.

4.1 Measurement Setup

To understand the measurement setup the standard procedure for measuring the conversion gain of a mixer is explained in the beginning. The modification of this setup to investigate the influence of the feedback path is explained afterwards.

4.1.1 Standard Method to Measure the Conversion Gain of Mixers

A basic characterization of the individual resistive mixer (Fig. 4.1) has been done in the past and the results are available for comparison. The standard setup to measure the conversion gain of the mixer is summarized in the following.

The LO and RF signals are each generated by a frequency synthesizer (E8257C PSG Analog Signal Generator, Agilent Technologies). The synthesizer for the RF signal is used up to its full specified bandwidth of $50\,\mathrm{GHz}$, the output signal being subsequently multiplied by three. The synthesizer for the LO signal operates from $130/12\,\mathrm{GHz}$ to $150/12\,\mathrm{GHz}$ and is multiplied by an x12 active fullband multiplier (AFM). To contact the wafer, D-band probes are used for the RF and LO signal. For the IF-path, a coaxial probe with $40\,\mathrm{GHz}$ connectors is used. The IF signal is displayed on a spectrum analyzer (PXA Signal Analyzer N9030A, Keysight). The DC supply provides the necessary gate

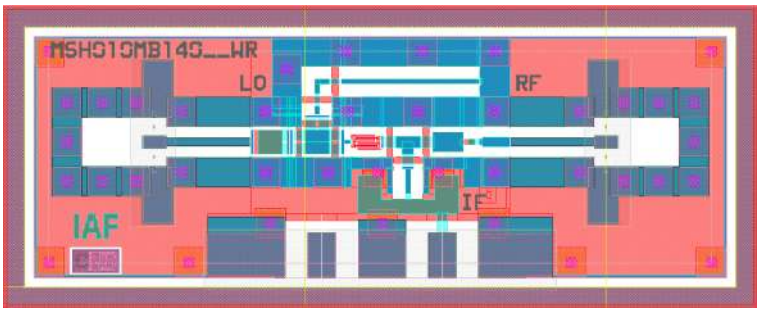

Figure 4.1: Layout of the measured individual resistive mixer designed and processed at the IAF. The LO signal is applied to the left RF pad and the RF signal to the right RF pad. The IF signal is routed off the chip at the bottom side. The RF and LO signals are fed to the FET by matching networks. The gate fingers of the FET are displayed in red in the middle of the layout. The DC line above the transistor is used for the gate bias.

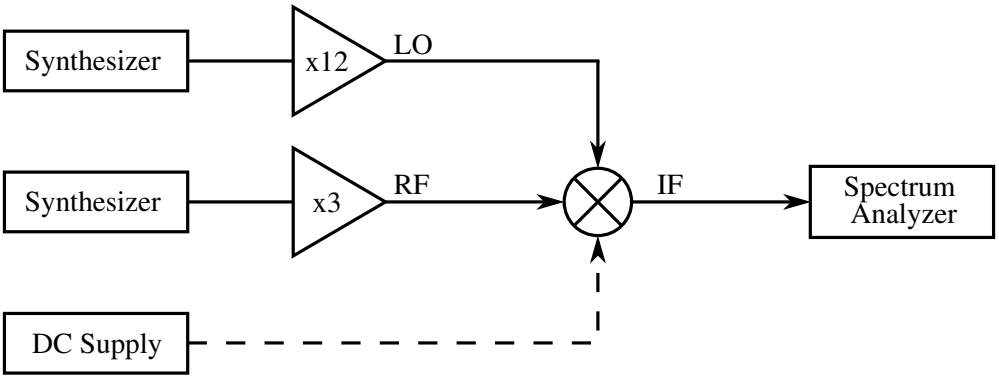

Figure 4.2: Schematic of the standard G_c measurement setup. The D-band signals are generated by a synthesizer in combination with multipliers and the resulting IF signal is captured with a spectrum analyzer. Note that the resistive mixer is operated with a gate bias, provided by the DC supply.

bias voltage for the mixer. A simplified overview of the measurement setup can be seen in Fig. 4.2. The measured conversion gain is shown in Fig. 4.3 with the corresponding parameters listed in Tab. 4.1. The conversion gain is about $-5\,\mathrm{dB}$ over the whole bandwidth and no dips occur because the LO-RF path is not yet implemented.

4.1.2 Addition of a Controlled LO-RF Feedback Path to the Setup

The setup presented in the previous section is modified to reproduce the problem of the dips in G_c in the presence of the additional LO-RF path. It is crucial to maintain a stable phase relationship between the LO and LO-RF signal to control the delay of the LO-RF signal w.r.t. the LO signal. Therefore, two channels of an Arbitrary Waveform Generator (M8195A 65GSa/s AWG, Keysight), instead of the second synthesizer, are used to generate the LO and LO-RF signal. As a consequence, both signals are derived from the same reference clock. Besides, an additional x12 multiplier is needed for the LO-RF signal. To superimpose the RF and LO-RF signal at the RF port of the mixer,

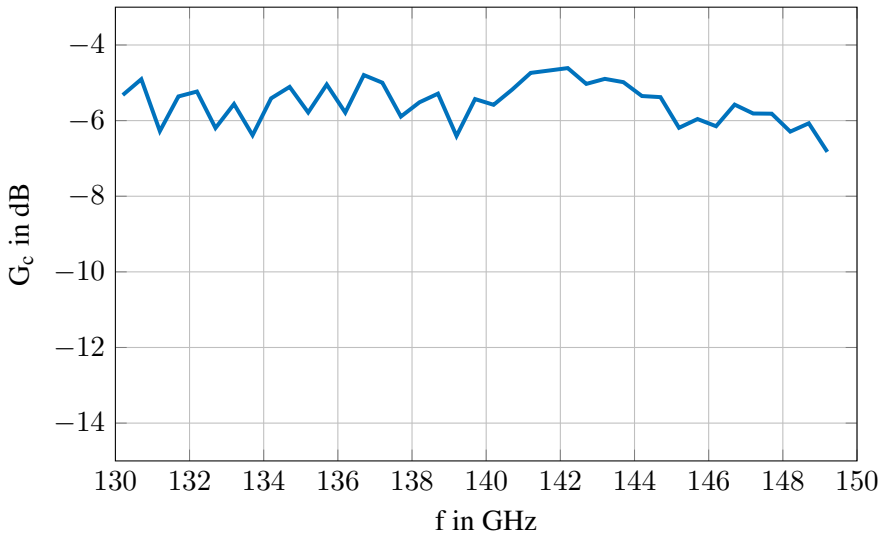

Figure 4.3: Measurement results of the conversion gain of the individual resistive mixer with the standard measurement setup without the interference signal LO-RF, used as a reference.

Table 4.1: Parameters for the characterization of the individual resistive mixer.

Parameter	Value	Unit
$V_{\mathrm{G,B}}$	-0.15	V
P_{LO}	2	dBm
P_{RF}	-20	dBm
f_{IF}	200	MHz

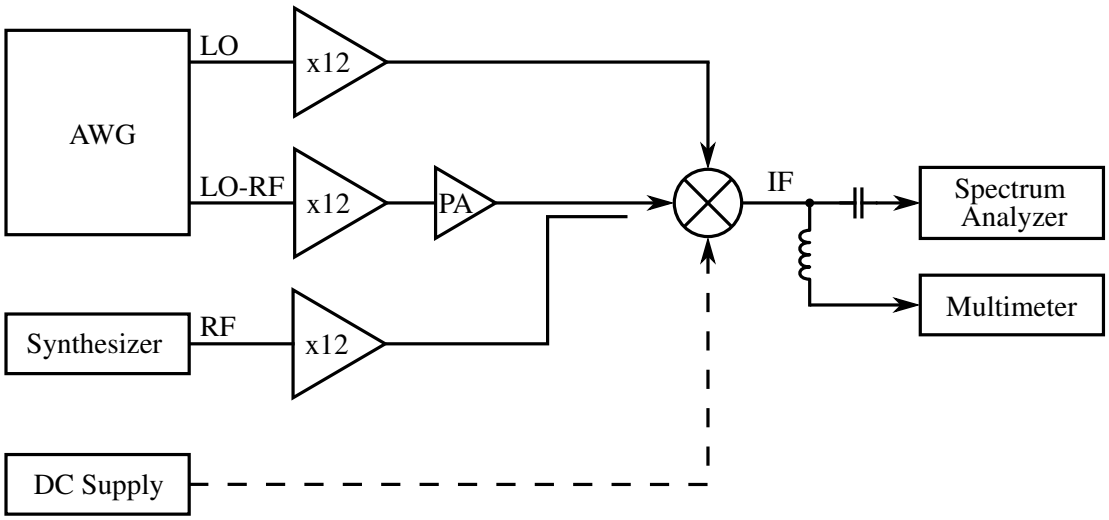

Figure 4.4: Block diagram of the modified measurement setup. The LO and LO-RF signal are generated with an AWG to synchronize their phase. The LO-RF signal is applied to the RF port of the mixer via a directional waveguide coupler. In addition to the desired IF, the DC component at the IF port is measured with a multimeter.

a directional waveguide coupler is used. The setup allows displaying the IF signal on a spectrum analyzer and its DC component on a multimeter. Both are connected to a bias tee which separates the RF and DC components. The schematic of the modified measurement setup is shown in Fig. 4.4; Fig. 4.5 and Fig. 4.6 show the probing station and the actual devices used in the measurement.

The AWG is a key element of the setup and will therefore be explained more in detail in the next section.

Programming the AWG

An AWG is a device used to generate an arbitrarily defined waveform based on the principle of direct digital synthesis. The AWG generates discrete values (samples) of the desired output signal which are stored in a fast memory. The samples are converted to voltages by a digital-to-analog (DA) converter. It is followed by a reconstruction filter which filters out the higher Nyquist zones of the analog signal. In addition, the AWG provides a control logic to synthesize complex sequences of segments [Keya].

To generate a sinusoidal signal, the configurable parameters are the sample rate ($f_\mathrm{s} = 1/T_\mathrm{s}$), the segment length ($l_\mathrm{seg}$) in samples, the number of periods (N), the amplitude of the signal (A), the frequency varying phase ($\Delta\varphi = 2\pi f\tau$) and the global phase ($\varphi_0$) which is independent of the frequency. The specifications for the available AWG are shown in Tab. 4.2. For the LO and LO-RF signal follow:

$$s = A \cdot \sin(2\pi ft + \Delta\varphi + \varphi_0) \tag{4.1}$$

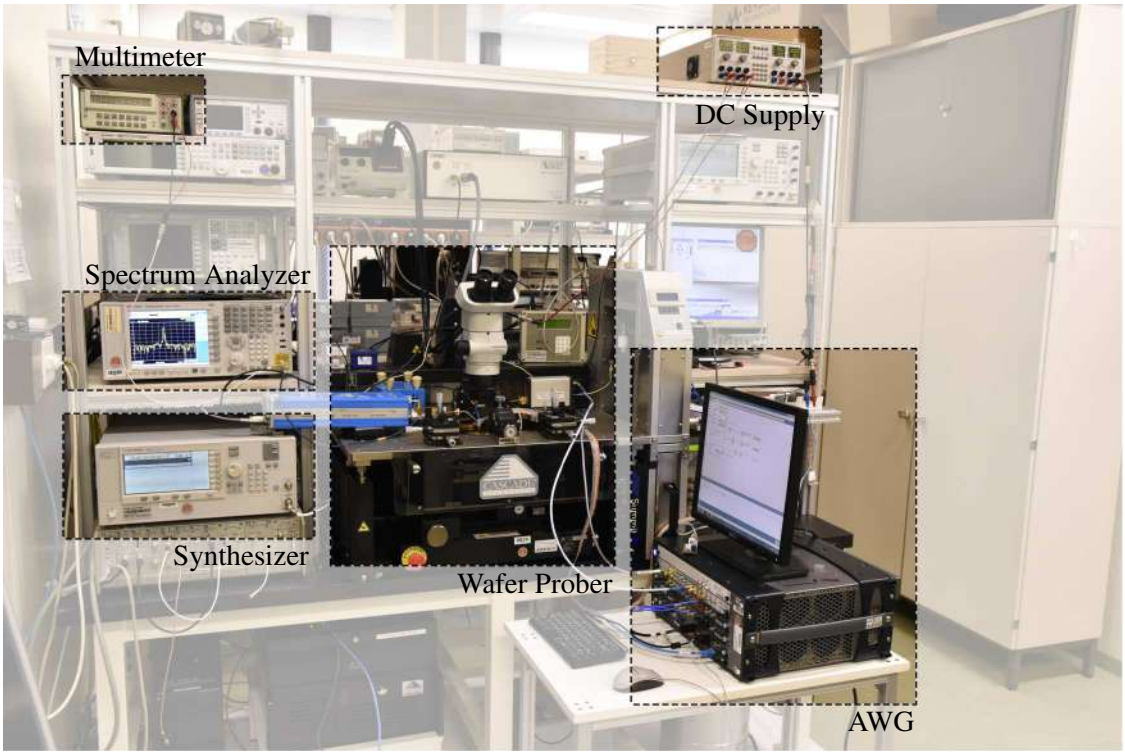

Figure 4.5: Picture of the whole measurement setup. The relevant devices are highlighted and connected according to the block diagram in Fig. 4.4.

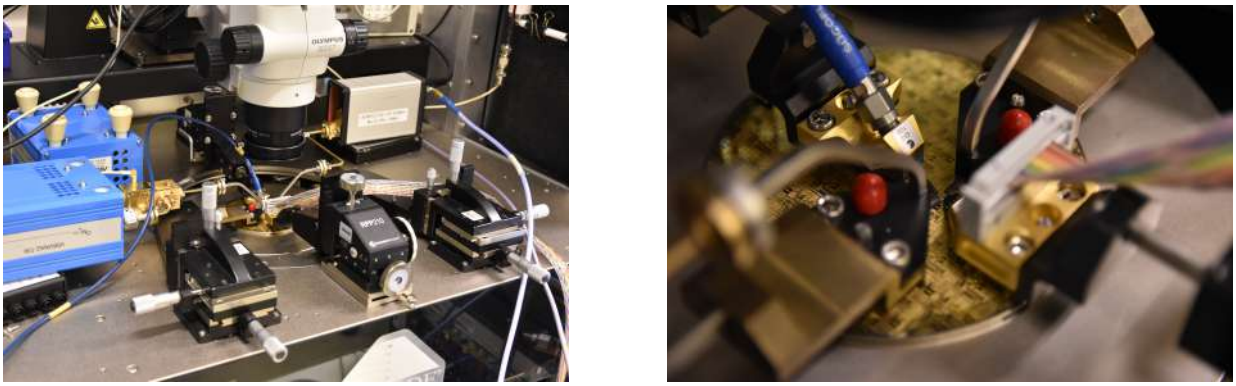

(a) (b)

Figure 4.6: Various closeups of the measurement setup in Fig. 4.5. (a) Wafer Prober with the x12 multipliers for the LO (LORF) signal on the right (left) hand side. The LO-RF multiplier is combined with the RF signal coming from the left hand side with a directional waveguide coupler. (b) Two D-band probes for the RF + RF-LO signal and the LO signal (bottom left and top right), coaxial probe with 40 GHz connectors for the IF signal visible in the top left, and a DC probe in the bottom right.

$$\text{with } f = \frac{N}{T} = \frac{N}{T_\text{s} \cdot l_\text{seg}} = \frac{N f_\text{s}}{l_\text{seg}}.$$

To achieve a frequency resolution of $100\,\text{MHz}$ at the MMIC, the frequency step size of the AWG has to be $\frac{100}{12}\,\text{MHz}$ because of the downstream x12 multiplier. There are several possible combinations of the parameters, one of the simplest being a fixed $f_\text{step} = \frac{f_\text{s}}{l_\text{seg}}$ and the variation of N only, leading to $f = N \cdot f_\text{step}$ as desired (see Tab. 4.3). Due to the discrete sampling and several filtering and transition stages in the signal chain, the theoretical output power according to the programmed amplitude differs from the actual power level. Some of these effects (such as the $sin(x)/x$ distortion due to the hold-circuit) can be easily compensated for while others (such as the analog reconstruction filter) are more challenging to predict. The frequency response of the AWG as specified by the manufacturer is cited in Fig. 4.7, making the calibration procedure described in the section "Challenges of the Measurement Setup" necessary.

The AWG offers the possibility to define a sequence of waveform segments. Each segment can be repeated until an external Advance Event is triggered. This feature is used to implement the frequency/phase stepping during the measurement loop.

Control of Measurement Devices

The standard IAF characterization routine for mixers is implemented in the Keysight Visual Engineering Environment (VEE). The remote control of the AWG and its synchronization with the other measurement devices were not available at the beginning of this work. Thus, a measurement script is developed in Matlab in order to implement the automated measurement routine for the modified setup.

The AWG is controlled via the virtual instrument software architecture (VISA) interface over the Transmission Control Protocol/Internet Protocol (TCP-IP). The other measurement devices are connected over a General Purpose Input Bus (GPIB). The command syntax for controlling the measurement devices is the Standard Commands for Programmable Instruments (SCPI). It defines a set of commands typical of certain device classes such as network analyzers, power meters etc. These ASCII strings are largely independent of the specific manufacture and provide a useful layer of abstraction. The developed measurement setup is based on these SCPI commands.

Challenges of the Measurement Setup

The required measurements in the D-band present some challenges which are discussed in the following.

1. Maximum power levels at the MMIC

   In the radar front end the expected LO power level at the resistive mixer is approx. $2\,\text{dBm}$. Due to the LNA in the receiver path the LO-RF signal can reach power levels in the same order of magnitude. To reproduce the scenario discussed in section 3.1.1 it is desirable to attain similar power levels in the measurement setup.

Table 4.2: Specifications of the AWG [Keyb].

Parameter	Specification
Sample rate	53.76 GSa/s to 65 GSa/s
V_{pp} in differential mode	0.5 V (3.98 dBm at 50 Ω)
Range of segment length (no. of segments)	1280 to 8 589 934 592
Max. number of periods	524 288
DAC resolution	8 bits
Frequency range for a multi-tone signal	DC to 32 GHz
Impedance of output channel	50 Ω
Internal synthesizer clock accuracy	0.7 ppm

Table 4.3: Parameters for the signal generation with the AWG.

Parameter	Value	Unit
f_s	32	GSa/s
l_{seg}	3840	Sa
N_{min}	1300	
N_{max}	1600	

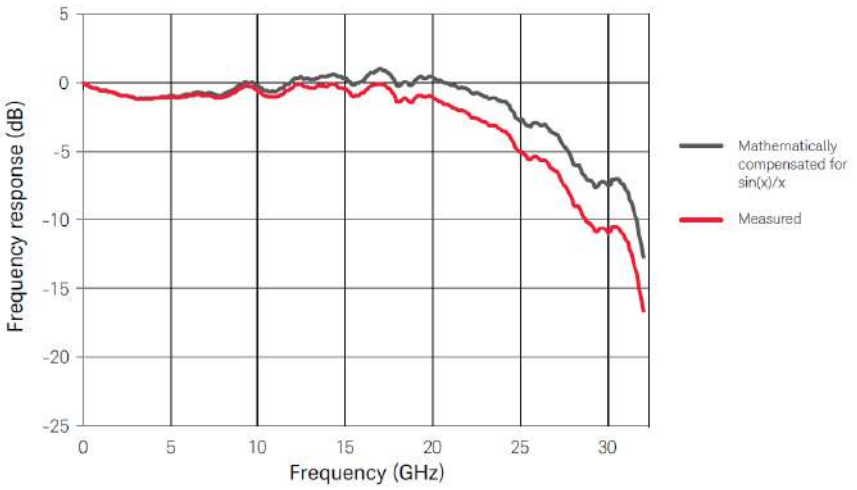

Figure 4.7: Frequency response of the AWG which indicates the deviation of the actual power level from the programmed amplitude [Keyb].

Table 4.4: Mean value and standard deviation of the power calibration.

Target level in dBm	Signal path	μ in dBm	σ in dBm
-1	LO-RF	-1.17	0.12
-1	LO	-1.59	0.28
-4	LO-RF	-4.31	0.33
-4	LO	-4.90	0.34

The maximum output power level of the AWG is about $4\,\mathrm{dBm}$. In the LO path, the resulting output power after the AFM is between $3\,\mathrm{dBm}$ and $10\,\mathrm{dBm}$ over the whole frequency band, including the cable losses. The LO-RF path can provide maximum power levels of $-0.8\,\mathrm{dBm}$ to $1.7\,\mathrm{dBm}$ after the directional waveguide coupler, including the AFM and PA. The second available AFM in the LO-RF path has a lower maximum output power than the AFM in the LO path and the output power of the downstream power amplifier is limited due to its saturation.

To obtain the power available at the MMIC level, the losses of the D-band probes of $2.6\,\mathrm{dB}$ have to be subtracted. This results in maximum power levels at the MMIC over the whole frequency band of $0.4\,\mathrm{dBm}$ for the LO signal and $-3.4\,\mathrm{dBm}$ for the LO-RF signal. Since the power levels are lower than the original power levels in the radar front end, a reduced gain is expected. Still, the dips in G_c can be observed and its occurrence can be investigated as the measurement results show in section 4.2.2. Note that the relative power levels have to be chosen correctly.

2. Calibration of the power levels of the LO and LO-RF signal

   As there are no regulated D-band sources available, the power levels of the signal paths have to be calibrated. In a first step the reference curves of the LO and LO-RF signal paths are measured from the output of the AWG to the input of the probes. It is found that the actual output power of the AWG does not match the theoretical value expected from the set amplitudes to the required level of accuracy (cf. Fig. 4.7). As a second step, the reference curves of the whole paths including the AWG are measured and used as a correction in the AWG. To assess the quality of the calibration, the resulting output power curves for $P_{\text{out}} = -1\,\mathrm{dBm}$ and $P_{\text{out}} = -4\,\mathrm{dBm}$ are crosschecked with a power meter and can be seen in Fig. 4.8. This power levels correspond to $P = -3.6\,\mathrm{dBm}$ and $P = -7.6\,\mathrm{dBm}$ at the MMIC, considering the loss of the probes of $-2.6\,\mathrm{dBm}$. The mean value (μ) and standard deviation (σ) of the power calibration are shown in Tab. 4.4. It can be seen that the power levels have a systematic deviation towards smaller values than the set value. The lower the requested power, the larger σ due to the increased steepness of the transfer function of the AFMs.

3. Verification of the phase relationship of the LO and LO-RF signal

   To realize the delay of the LO-RF signal it is crucial that the LO and LO-RF signal are generated synchronously and the relative phase difference of the LO and LO-RF signal is controllable over the whole bandwidth and for all power levels. Unfortunately, the devices along the

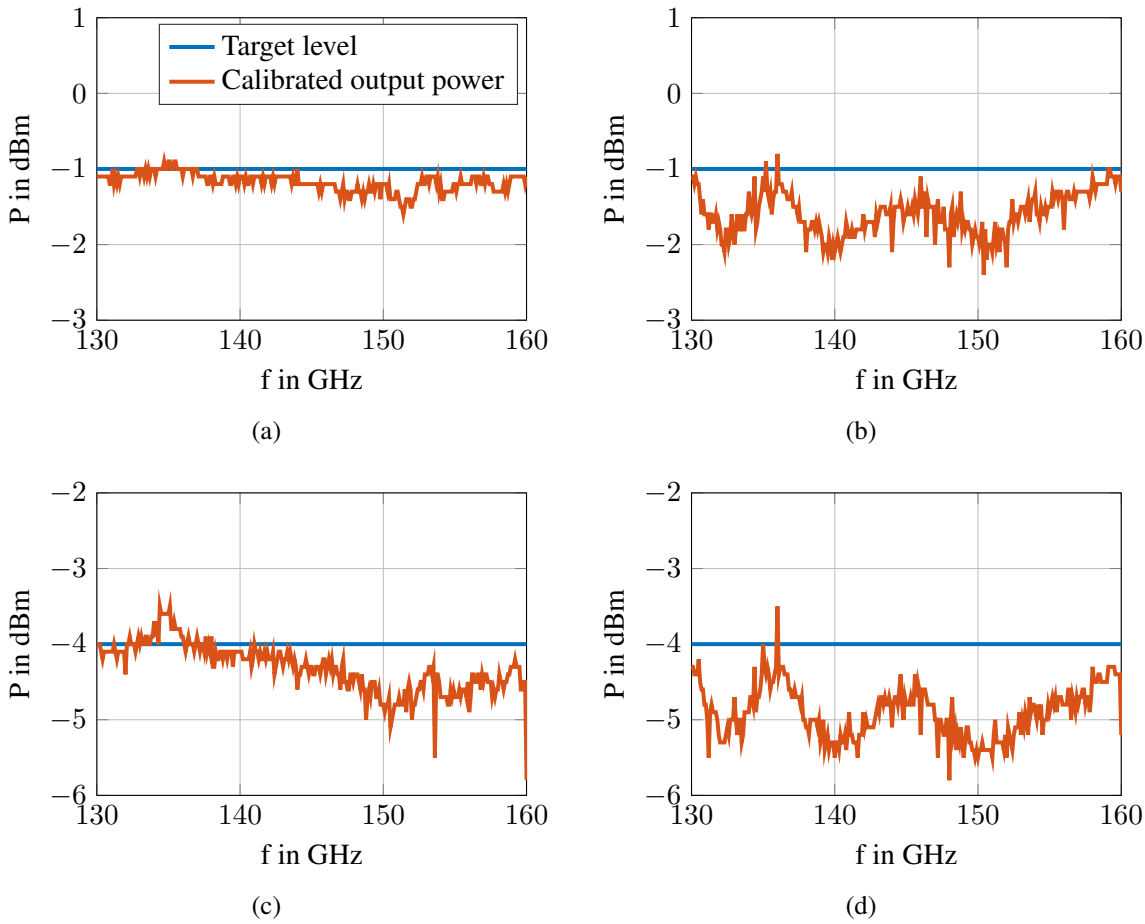

Figure 4.8: Measurement of the output power levels after the AFMs, (a)(c) for the LO-RF path, (b)(d) for the LO path. Note that these power levels do not include the probe losses of $-2.6\,\mathrm{dB}$.The color coding of the curves is the same for all subfigures.

signal path do not show a linear phase behavior independent of the power amplitude. This causes some challenges which are addressed in the next section.

4.2 Measurement Sequences and Analysis

Based on the constraints regarding the maximum attainable power levels at the MMIC the following power scenarios are chosen to analyze the behavior of the mixer:

Table 4.5: Chosen power levels at the MMIC.

Scenario	P_{LO} in dBm	P_{LORF} in dBm
$P_{\mathrm{LO}} = P_{\mathrm{LORF}}$	-3.5	-3.5
$P_{\mathrm{LO}} > P_{\mathrm{LORF}}$	-3.5	-7.0
$P_{\mathrm{LO}} < P_{\mathrm{LORF}}$	-7.0	-3.5

Two measurement series are performed to obtain the conversion gain. First it is measured directly versus the frequency and in the second series, G_c is measured versus the phase for each frequency.

4.2.1 First Measurement Sequence – Variation of the Frequency

In the first measurements the IF power is directly measured over frequency. The conversion gain is then calculated using Eq. 2.9. The procedure for the measurement is shown in Measurement Program 1. The adjustable input parameters are the first frequency point f_1 and the last frequency point f_2, the number of frequency points N_f, the IF frequency f_{IF}, the power levels P_{RF}, P_{LO}, P_{LORF}, the delay τ and the global phase shift φ_0.

The first measurement is performed with the parameters given in Tab. 4.6. $\tau = 0\,\mathrm{ps}$ is chosen first to obtain a reference curve and the result can be seen in Fig. 4.9(a). It can be seen that G_c is very noisy with a lot of dips. This could be explained by an additional delay caused by the propagation times of the LO and LO-RF paths due to the different lengths of the cables and the other components in the signal path.

To calibrate the phase of the signal paths, the DC component of the IF signal is measured with a multimeter for each frequency point with a programmed phase difference of the LO and LO-RF signal of $0°$. As described in chapter 3, the theoretical IF-DC signal is a cosine proportional to $\cos(2\pi f\tau)$. The resulting cosine thus provides information about the introduced τ by the devices in the path. To obtain τ a Fourier transform is calculated w.r.t. f. The Fourier transform of the theoretical cosine features two Dirac impulses, one for the positive and one for the negative value of τ. In this case, f mathematically corresponds to the time domain variable and τ to the frequency domain variable.

A plot of the FFT versus the delay can be seen in Fig. 4.10. Using the Nyquist-Shannon sampling theorem, the maximum unambiguous phase difference φ of two adjacent frequency points is π

Table 4.6: Parameters used in the modified measurement setup.

Parameter	Value	Unit
f_1	130	GHz
f_2	160	GHz
N_f	301	
f_{IF}	100	MHz
$V_{\text{G,B}}$	-0.15	V
P_{LO}	-3.5	dBm
P_{LORF}	-3.5	dBm
P_{RF}	-20	dBm
τ	0	ps
φ_0	0	°

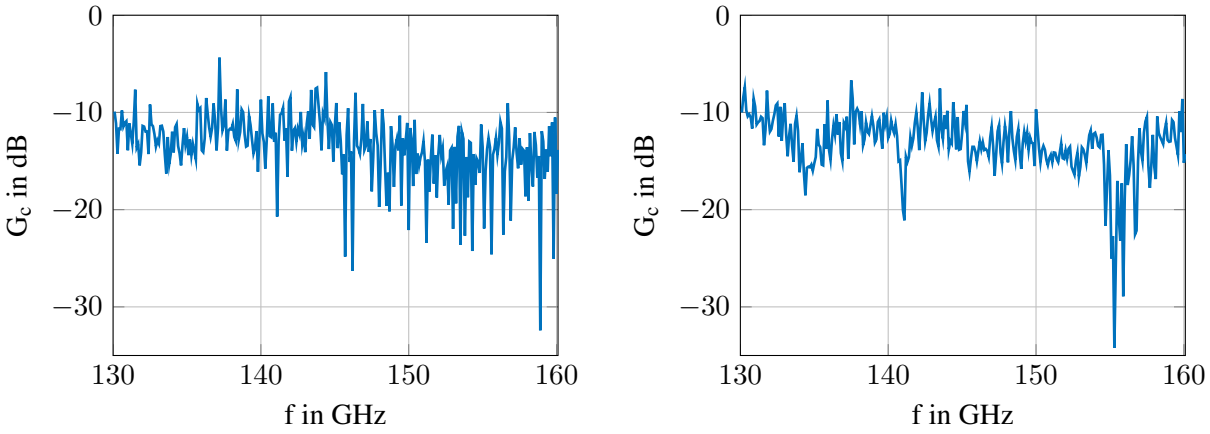

Figure 4.9: Measured conversion gain, (a) no delay between the LO and LO-RF signal, and (b) $\tau = 4\,\text{ns}$ in an attempt to compensate for the delays of the cables.

Measurement Program 1 G_c versus frequency.

Input: f_1, f_2, N_f, f_{IF}, P_{RF}, P_{LO}, P_{LORF}, τ, φ_0

Output: $G_c(f)$

1: $f_{\text{min}} \leftarrow f_1$
2: $f_{\text{max}} \leftarrow f_2$
3: $f_{\text{step}} \leftarrow (f_{\text{max}} - f_{\text{min}})/(N_f - 1)$
4: Synthesizer: set calibrated output power
5: AWG: set calibrated power for channel 1 (LORF) and channel 2 (LO)
6: AWG: program sequence of sinoids from f_{min} to f_{max} in f_{step} for f_{LO} and f_{LORF}, according to Eq. 4.1
7: **for** $k = 1$ to N_f **do**
8: Synthesizer: set f_{RF} to $f_{\text{min}} + (k-1)f_{\text{step}} + f_{\text{IF}}$
9: AWG: trigger Advance Event, the current segment has
$f_{\text{LO}} = f_{\text{LORF}} = f_{\text{min}} + (k-1)f_{\text{step}}$
$\varphi_{\text{LO}} = 0^\circ$
$\varphi_{\text{LORF}} = \varphi_0 + 2\pi f_{\text{LORF}}\tau$.
10: Spectrum Analyzer: read power of IF at f_{IF}
11: PC: calculate $G_c = P_{\text{IF}}/P_{\text{RF}}$
12: **end for**

which leads to

$$2\pi\Delta f\tau_{\text{max}} = \pi \quad \Leftrightarrow \quad \tau_{\text{max}} = \frac{1}{2\Delta f}. \tag{4.2}$$

With $\Delta f = 100\,\text{MHz}$, this results to a maximum unambiguous delay of $\tau_{\text{max}} = 5\,\text{ns}$. Beyond $5\,\text{ns}$ the spectrum is repeated. The y-axis is normalized because the absolute value is not relevant. It can be seen that a number of peaks occur at around $4\,\text{ns}$. This leads to the assumption that an effective delay introduced by the components in the signal path is around $4\,\text{ns}$. It is attempted to compensate for the delay in the signal path by calibrating the LO-RF signal with an additional delay of $4\,\text{ns}$ as this corresponds to one of the highest peaks in the FFT. Fig. 4.9(b) shows the resulting G_c. It can be seen that the signal is still very noisy.

As there is not only one Dirac impulse observed, the phase distortion caused by the components in the signal path is not linear (corresponding to an effective delay) but depends on the frequency in a non-linear way and also on the power levels. Thus, the influence of the phase on the LO and LO-RF signal requires the information of the actual phase offset φ_{off} as a function of f and P and cannot be fully compensated for in this straight forward way.

Without being able to compensate for the delay of the cables and the other non-linear transfer functions in the signal path in the order of ns, it is not possible to display the original dips which are caused by a delay in the order of ps.

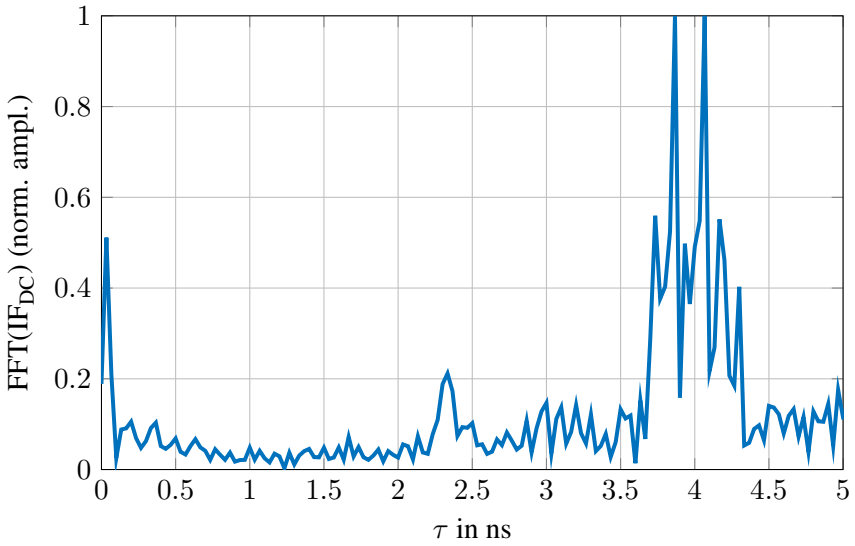

Figure 4.10: FFT of the IF-DC signal with $\tau = 0\,\mathrm{ps}$ and $\varphi_0 = 0°$ to estimate the propagation delay of the different paths. Due to the finite frequency resolution the maximum unambiguous delay is $5\,\mathrm{ns}$ according to the Nyquist-Shannon sampling theorem.

4.2.2 Second Measurement Sequence – Variation of the Phase

To overcome the uncertainty regarding the phase relation of the LO and LO-RF signal, a different measurement approach is devised and realized. In contrast to the first measurement series, not only the frequency but also the phase difference of the LO and LO-RF signal is swept. This means that for each frequency point the relative phase of the LO and LORF signal is swept from 0 to $360°$. The IF signal and its DC component are measured simultaneously. The information about the phase relationship is obtained from the IF-DC signal which, again, has the form of a cosine. The shift of e.g. the maximum of this cosine provides the necessary information about the phase offset. This phase offset is defined as the actual phase difference of the LO and LO-RF signal as indicated by the IF-DC component for a programmed phase offset of $0°$ at the AWG. According to this phase offset, the conversion gain can be shifted on the φ-axis. Thus, the phase difference of the LO and LO-RF signal is directly calibrated at the mixer without the need for precise information about the phase behavior of the components in the signal paths. This measurement series contains more information than the previous one because every possible combination of the frequency and the phase relationship of the LO and LO-RF signal is measured. Any phase difference and effective delay can be synthesized from the available measurement data.

Assessment of the Raw Data

In Fig. 4.11 the described measurement is shown in comparison with the simulation of the IF power and its DC component for the frequencies $140\,\mathrm{GHz}$ and $150\,\mathrm{GHz}$. Note that the simulated data are shifted in such a way that the maximum of the measurement and the simulation are at the same phase. The measured and simulated data are in good agreement. In these examples, the phase

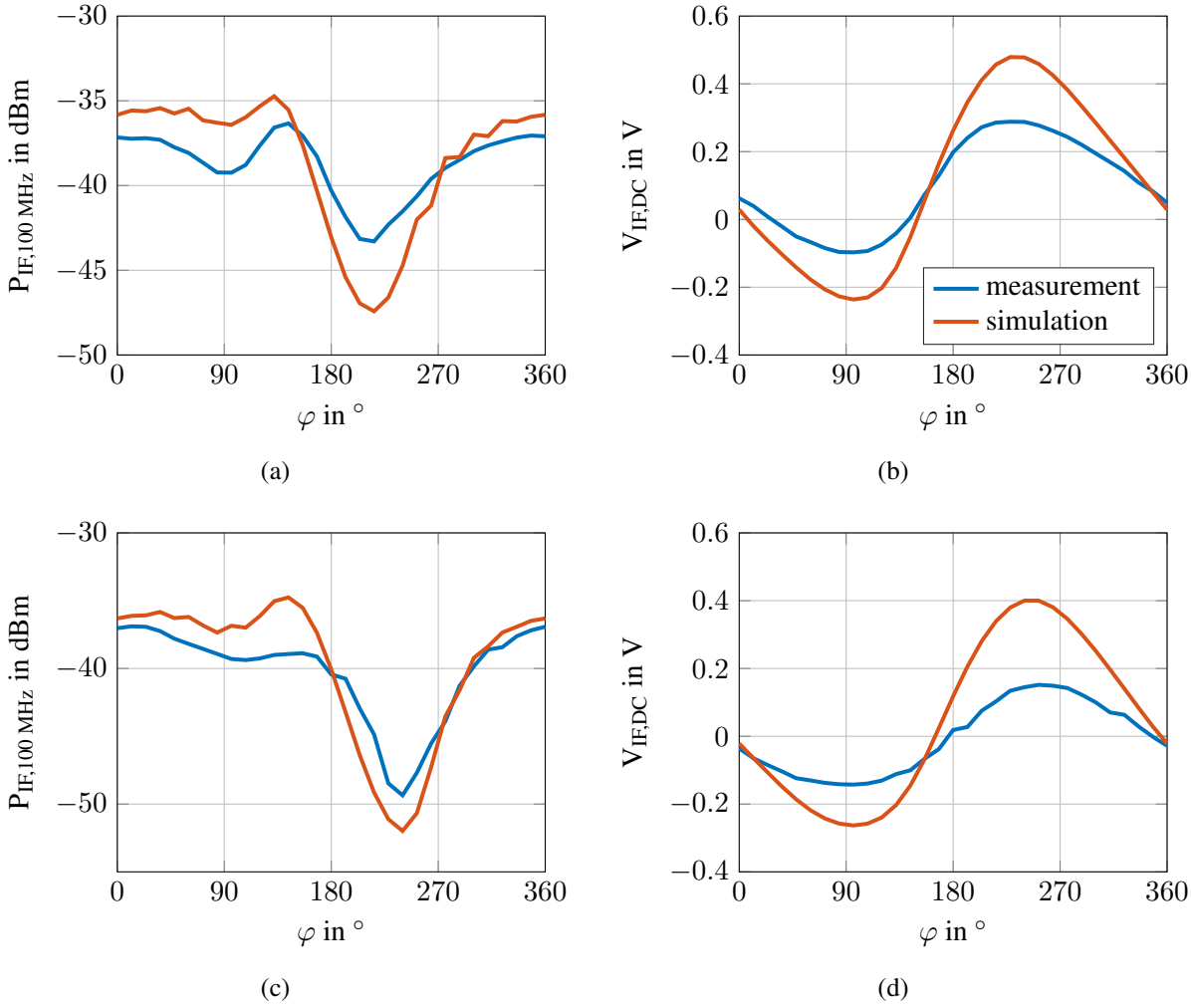

Figure 4.11: Measurement and simulation results of the IF signal and its DC component versus the programmed phase difference between LO and LORF, for $f = 140\,\text{GHz}$ (a,b) and $f = 150\,\text{GHz}$ (c,d). The color coding of the curves is the same for all subfigures.

offset w.r.t. the maximum is around 230° (250°) for 140 GHz (150 GHz).

The correlation between the positions of the maxima of $P_{\text{IF,DC}}$ and the dips in $P_{\text{IF,100 MHz}}$ is an interesting quantity. In Fig. 4.12, each cross corresponds to one frequency. The x-coordinate of a cross corresponds to the position of the maximum of the IF-DC component, the y-coordinate to the position of the minimum of $P_{\text{IF,100 MHz}}$. Most points are close to the bisector of the line $y = x$. There are also accumulations of frequency points near the two parallel lines $y = x \pm 180°$.

Without further calculations this diagram allows the conclusion that the occurrence of the dips indeed corresponds to a specific phase relation between the LO and LO-RF signal. The position of the maximum of the IF-DC component defines the point $\varphi = 0°$. If the dips occur at the same phase difference, this also results in $\varphi = 0°$ via the offset correction. Thus, the points on the bisector of the line $y = x$ show all frequencies that have their minimum in G_c at a phase difference of $\varphi = 0°$ at the IF port. The two parallel accumulation lines show the frequencies where the minimum of G_c

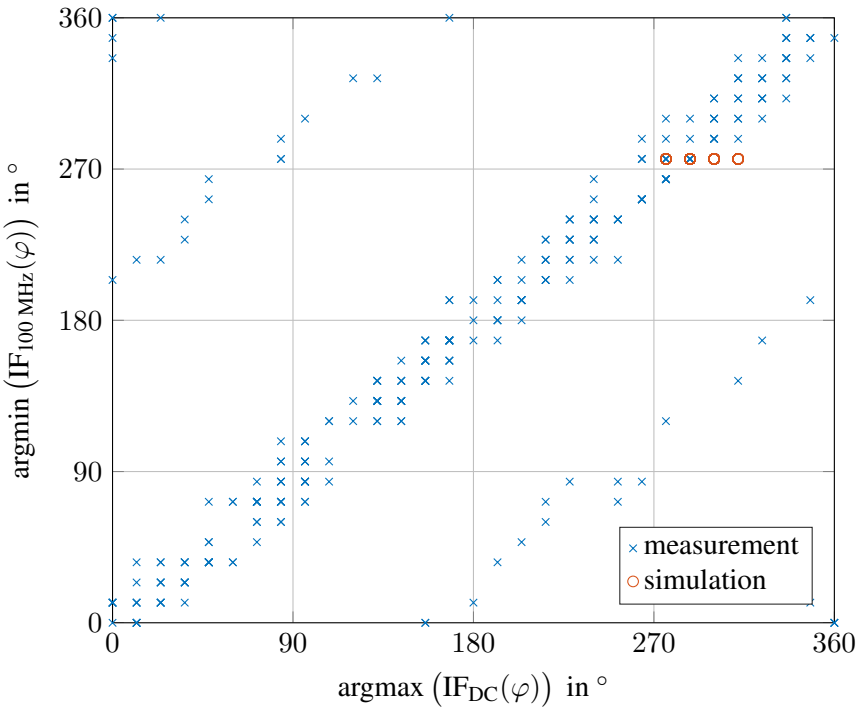

Figure 4.12: Correlation between the position of the minima in the conversion gain and the maxima of the IF-DC signal. Each cross or circle corresponds to a single frequency point. Note that there is no phase fluctuation in the simulation as it only includes the MMIC and not the signal generation in the measurement system.

occurs at $\varphi = 180°$ and $\varphi = -180°$ which indicates that the second minimum in G_c is sometimes more pronounced than the minimum at $0°$.

To crosscheck these results, the same setup is simulated, i.e. for each frequency point the IF power is swept over different φ of the LO and LO-RF signal, which is displayed by the circles in Fig. 4.12. It can be seen that the phase difference of the LO and LO-RF signal for the minimum in G_c and the maximum of the IF-DC signal is around $270°$ for all frequencies. Only four points can be seen because the results for all frequencies share the same phase offset. In the simulation no additional phase offset is set. Thus, the dips occur at the same phase offset and do not vary in the same way as the measurements which includes the active components and cable delays. The simulation results also indicate that the minimum of G_c occurs at $\varphi = 0°$. As mentioned before, it is not easy to define the actual physical position, e.g. drain/gate etc. at the transistor for this phase relation. However, this is irrelevant for the purpose of this analysis.

Synthesis of the Conversion Gain over Frequency

Using the information about the phase offset extracted in the previous section, the conversion gain can be calculated as a function of the frequency. The following calculations were implemented in Matlab.

In a first step, the position of the maximum of the IF-DC signal is determined which directly yields

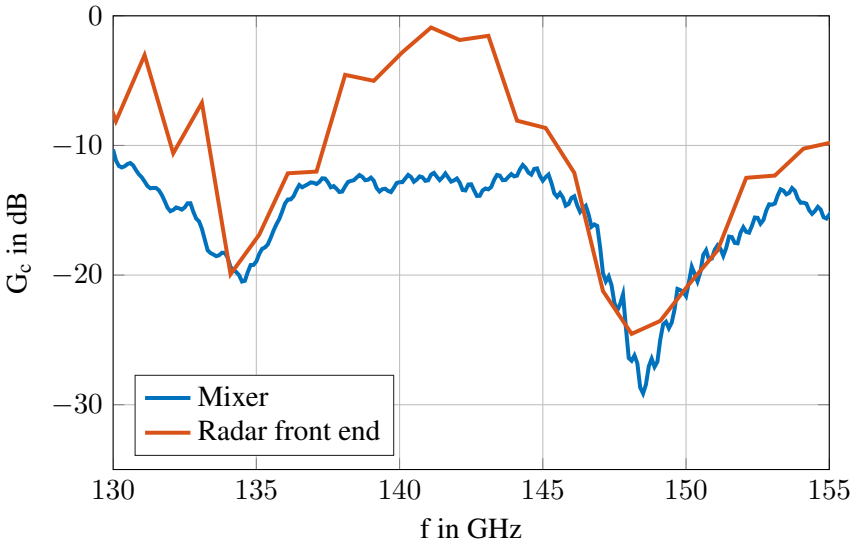

Figure 4.13: Comparison of the measurement of the integrated radar transceiver with the measurement of the individual mixer with $\tau = 71\,\mathrm{ps}$ and a global phase $\varphi_0 = 160°$. The LO/LORF power levels are around $2\,\mathrm{dBm}$ at the mixer of the radar front end and $-3.5\,\mathrm{dBm}$ at the individual mixer.

the phase offset φ_{off} caused by the components in the signal generation paths. In the second step, the relative phase $\Delta\varphi$ corresponding to the requested effective delay τ is calculated according to Eq. 3.1. The global phase φ_0 is added which is expected to shift the position of the dips.

In the last step, the measured G_c is evaluated at a phase of

$$\varphi = (\varphi_{\mathrm{off}} + \Delta\varphi + \varphi_0) \bmod 2\pi \tag{4.3}$$

for each frequency point and the resulting $G_c(f)$ is synthesized for the parameters τ and φ_0 from these values.

To compare the measurement data acquired directly at the mixer with the measurement of the integrated radar front end, both curves are shown in Fig. 4.13. With a delay of $71\,\mathrm{ps}$ and a global phase of $160°$, the mixer measurement agrees with the original measurement results. It can be observed that the mean value for G_c is higher for the integrated transceiver. This is due to the higher power level of the LO signal reaching the mixer ($P_{\mathrm{LO}} = 2\,\mathrm{dBm}$ vs. $P_{\mathrm{LO}} = -3.5\,\mathrm{dBm}$ at the individual mixer). The dip in G_c at higher frequencies is more pronounced for both measurements. Note the coarser frequency resolution in the measurement of the radar front end.

The raw data of the measurement is quite noisy as seen in Fig. 4.14, due to the statistical variation of the calibrated power levels at the MMIC (cf. Fig. 4.8). To smooth these variations, the measurement data are processed using a Savitzky-Golay filter. It is based on the method of linear least squares approximation by fitting the data in small intervals to a low-degree polynomial. To filter the measurement data, an interval length of 11 points and a polynomial degree of 3 is chosen. With these parameters the high frequency noise can be filtered while not affecting the position and shape of the dips. An example is shown in Fig. 4.14, the processed data is less noisy and still correctly

Figure 4.14: Example measurement data in its noisy raw version and after applying the Savitzky-Golay filter of degree 3 and with an interval length of 11. The parameters of the measurement are $\tau = 71\,\mathrm{ps}$ and $P_{\mathrm{LO}} = P_{\mathrm{LORF}} = -3.5\,\mathrm{dBm}$.

reproduces the characteristic features. The delay is $71\,\mathrm{ps}$ and $P_{\mathrm{LO}} = P_{\mathrm{LORF}} = -3.5\,\mathrm{dBm}$ for both curves.

In the following paragraphs, the influence of different parameters on the dips is investigated.

The influence of τ is shown in Fig. 4.15. The delay is chosen as $\tau = 35\,\mathrm{ps}$, $\tau = 71\,\mathrm{ps}$ and $\tau = 142\,\mathrm{ps}$ for $P_{\mathrm{LO}} = P_{\mathrm{LORF}} = -3.5\,\mathrm{dBm}$. As in the ADS simulation, the frequency separation of the dips becomes proportionally closer with increasing τ. For $\tau = 142\,\mathrm{ps}$, the second dip lies in the middle of the two dips for $\tau = 71\,\mathrm{ps}$. It can also be seen that for smaller frequencies the dips are less pronounced than for higher frequencies. In addition, it can be observed that the dips become narrower for higher τ. With larger delays, the phase difference changes at a higher rate and remains in the critical region for a smaller frequency interval.

The second parameter being varied is the global phase difference between the LO and LO-RF signal. Fig. 4.16 shows the result for $\varphi_0 = 0°$, $\varphi_0 = 90°$ and $\varphi_0 = 180°$ for $\tau = 71\,\mathrm{ps}$ and $P_{\mathrm{LO}} = P_{\mathrm{LORF}} = -3.5\,\mathrm{dBm}$. Changing the global phase difference causes a shift of G_c on the frequency axis.

To investigate the influence of the self-biasing effect of the drain, the DC current of the IF signal instead of the DC voltage was measured with the multimeter. Measuring the current implies shorting the drain, thus the conversion gain is measured with a drain bias of $0\,\mathrm{V}$. In Fig 4.17 it is observed that the dips become less pronounced in the case of zero drain bias, leading to the dip vanishing at lower frequencies. As seen in the ADS simulation, the drain bias is not the cause of the dips, but the measurement results indicate that it is possible to reduce them with a $0\,\mathrm{V}$ bias to the drain.

In a last step, the ratio of the power levels of the LO and LO-RF signal is varied (Fig. 4.18). The case of similar power levels ($P_{\mathrm{LO}} = P_{\mathrm{LORF}} = -3.5\,\mathrm{dBm}$) is compared to a higher LO power level ($P_{\mathrm{LO}} = -3.5\,\mathrm{dBm}, P_{\mathrm{LORF}} = -7\,\mathrm{dBm}$) and a smaller LO power level ($P_{\mathrm{LO}} = -7\,\mathrm{dBm}, P_{\mathrm{LORF}} =$

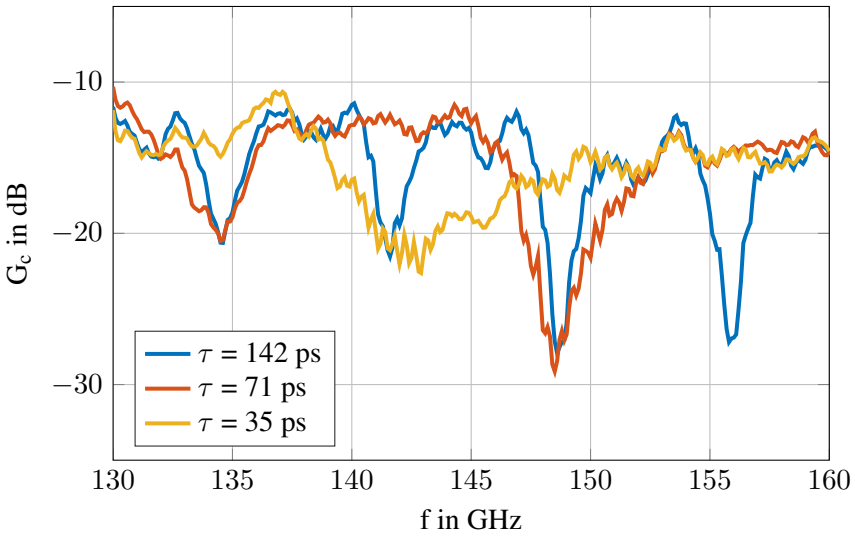

Figure 4.15: Comparison of different delays with $P_{\mathrm{LO}} = P_{\mathrm{LORF}} = -3.5\,\mathrm{dBm}$.

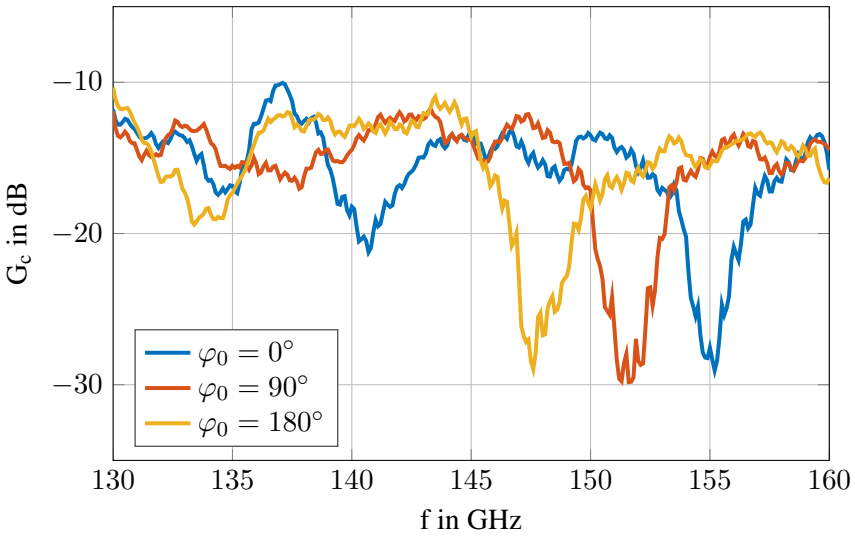

Figure 4.16: Influence of the global phase difference on the conversion gain with $\tau = 71\,\mathrm{ps}$ and $P_{\mathrm{LO}} = P_{\mathrm{LORF}} = -3.5\,\mathrm{dBm}$.

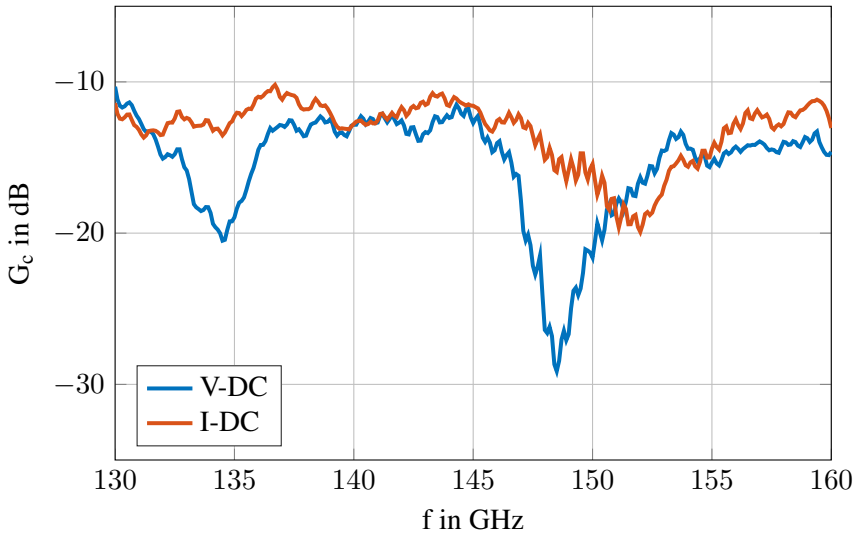

Figure 4.17: Comparison of the conversion gain with a drain bias of $-0.15\,\mathrm{V}$ (V-DC) and $0\,\mathrm{V}$ (I-DC). The measurement with $0\,\mathrm{V}$ bias is realized by measuring the DC current with a multimeter. The values for τ and the power levels are the same as for Fig. 4.16.

$-3.5\,\mathrm{dBm}$) w.r.t. the LO-RF power level. Choosing a higher LO power level leads to slightly less pronounced dips. The case of $P_{\mathrm{LO}} < P_{\mathrm{LORF}}$ is not easily comparable to the other two curves because the mean value of G_c is already lower due to the lower LO power level. Note that the actual power levels of the signals fluctuate (cf. Fig. 4.8) which makes the comparison of the power levels difficult.

To be able to evaluate the influence of the power levels of the LO and LO-RF signal in a more reliable way, an additional measurement is performed, now at the integrated transceiver MMIC. It is possible to indirectly vary the power level of the LO-RF signal by adjusting the drain current or voltage of the LNA, respectively. The measurement results for G_c with different drain currents of the LNA can be seen in Fig. 4.19. Five different bias currents are chosen to $75\,\mathrm{mA/mm}$, $100\,\mathrm{mA/mm}$, $125\,\mathrm{mA/mm}$, $150\,\mathrm{mA/mm}$ and $250\,\mathrm{mA/mm}$. Note that for the original measurement (Fig.1.1) the drain current was chosen to $150\,\mathrm{mA/mm}$. It can be observed that for higher bias currents the dips in G_c become more pronounced. Higher bias currents correspond to a higher output power of the LNA, thus reaching higher power levels of the LO-RF signal. For smaller bias currents the dips become very small. In addition it can be seen that the conversion gain is reduced at lower frequencies. This effect is stronger for smaller bias currents. The collapse of G_c for low frequencies can be explained by the growing mismatch of the LNA when operated with lower gain or output power. Thus, the possibility to reduce the dips comes with a lower usable frequency bandwidth. The overall level of G_c is not much affected because the coupled LO signal drives the LNA into saturation, reducing its RF gain from $30\,\mathrm{dB}$ to around $12\,\mathrm{dB}$, almost independently of the drain current.

With the present extension of the measurement setup it is finally possible to demonstrate the occurrence of the dips directly at the individual mixer. The difficulties of the phase calibration are overcome by measuring the IF power at $100\,\mathrm{MHz}$ and DC as a function of the phase difference of

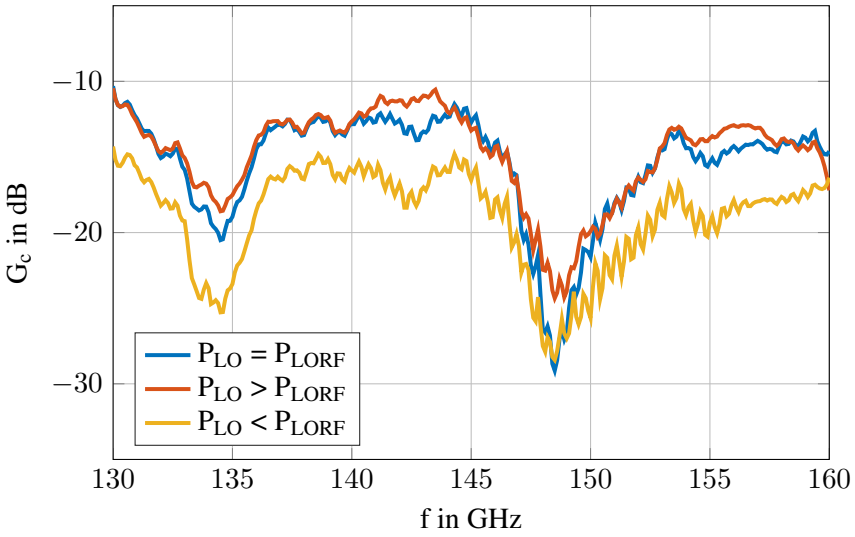

Figure 4.18: Comparison of different power levels of the LO and LO-RF signal for a delay of 71 ps. The power levels corresponding to the three scenarios in Tab. 4.5.

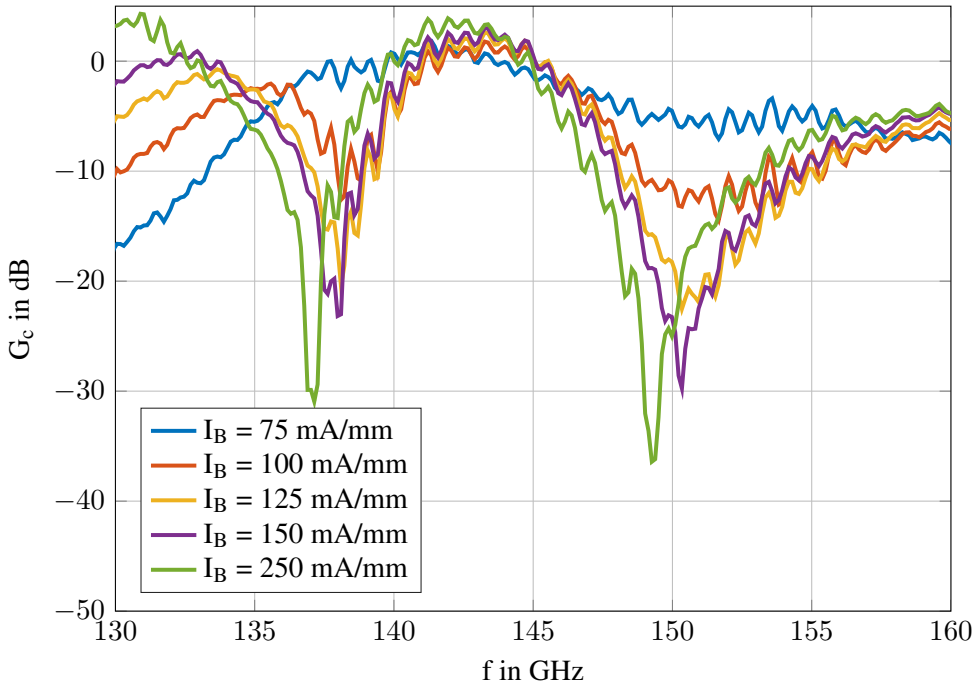

Figure 4.19: Measurement results for the conversion gain of the integrated transceiver with different drain currents of the LNA to adjust the power level of the LO-RF signal.

the LO and LO-RF signal. Extracting the necessary information about the phase offset of the LO and LO-RF signal from the DC measurement allows the reconstruction of the conversion gain over the frequency. Using the new measurement setup, it was possible to investigate the impacts of the effective delay, the global phase shift, the power levels of the LO/LO-RF signal and the drain bias and to dramatically improve the results from the direct measurement (Fig. 4.9(a)), effectively eliminating the negative influence of the nonlinear multiplication and amplifying stages in the signal paths on the phase control.

5 Solution Approaches

The presented simulations, analytic models and measurements all support the assumption that the dips in G_c are caused and can be controlled by the effective delay τ between the LO and LO-RF signal. To compensate for this relative delay and thus avoid the occurrence of critical phase differences, an additional delay can be inserted in the LO path, thus reducing the effective delay between both paths. In this section, different circuit design approaches to realize such a delay cell are investigated. In the general case, the effective delay or group velocity of a two-port is calculated as the derivative of the phase of S_{21} w.r.t. the frequency. Note that the phase has to change linearly over the frequency to describe an effective delay.

5.1 Basic Transmission Line

The easiest way to generate a delay τ is by means of a basic transmission line (TL). The required length of a homogeneous the TL line is calculated as

$$l = c_{\text{eff}}\tau = \frac{c_0}{\sqrt{\varepsilon_{\text{r,eff}}}}\tau \tag{5.1}$$

with the propagation velocity c_{eff} in the medium and the speed of light c_0. For the GaAs substrate, $\varepsilon_{\text{r}} = 12.9$. For a first estimation for $\varepsilon_{\text{r,eff}}$ it is assumed that half of the electric field lines are in free space, and half are in the dielectric. This results in

$$\varepsilon_{\text{r,eff}} \approx \frac{\varepsilon_{\text{r}} + 1}{2} = 6.95. \tag{5.2}$$

Consequently, a length of around $8.08\,\text{mm}$ is needed to realize a delay of $\tau = 71\,\text{ps}$.

To determine the actual delay of the IAF CPW transmission line, an ADS S-parameter simulation is performed. The available IAF model is based on results of a 3D EM simulation. The characteristic impedance is chosen to $50\,\Omega$ because the radar front end is originally implemented in a $50\,\Omega$ environment. The phase of S_{21} and the resulting delay for a length of $4.1\,\text{mm}$ and $8.2\,\text{mm}$ are shown in Fig. 5.1. Not surprisingly, the phase of S_{21} shows a linear behavior over the frequency. A length of $4.1\,\text{mm}$ results in a delay of around $35\,\text{ps}$ and $l = 8.2\,\text{mm}$ results in around $71\,\text{ps}$. The latter agrees with the calculated estimation. Obviously, a higher length implies higher transmission losses, displayed in Fig 5.2 for both cases.

Though a simple transmission line offers almost perfect linearity, it is not economical to insert such a delay line considering the overall dimensions of the MMIC (4x2 mm^2). The relatively high losses are another potential disadvantage which might be compensated for by an additional amplifier stage.

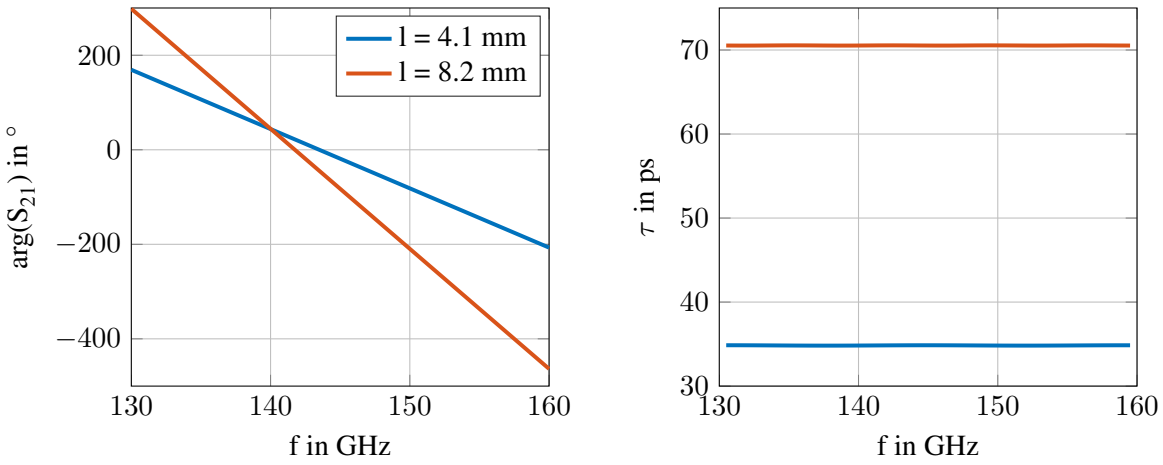

Figure 5.1: Results of the ADS simulation of a $50\,\Omega$ CPW transmission line, (a) phase of S_{21}, and (b) delay τ calculated as the derivative of $\arg(S_{21})$ w.r.t. the frequency. The color coding of the curves is the same for both subfigures.

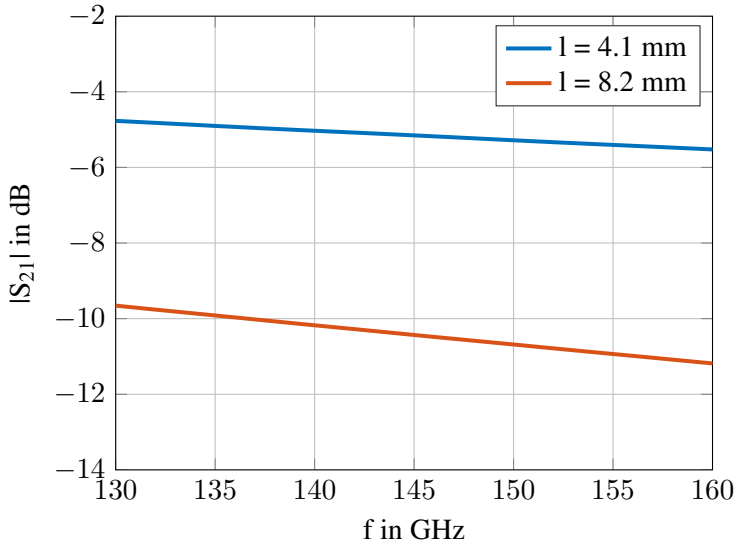

Figure 5.2: Transmission losses of a $50\,\Omega$ CPW TL based on an ADS simulation.

5.2 All-Pass g_m-RC Delay Circuit

A TL is a special kind of an all-pass filter with a linear phase shift. One possible active realization is the all-pass g_m-RC delay circuit.

The transfer function of an all-pass filter in the Laplace domain is

$$H(s) = e^{-s\tau}. \tag{5.3}$$

A first-order all-pass filter provides this functionality to a good approximation. Its transfer function includes only the first order products of the pole-zero representation of H(s) and results in:

$$H_{ap} = \frac{1 - s(\tau/2)}{1 + s(\tau/2)} \tag{5.4}$$

The magnitude and phase of a first-order all-pass filter is compared to an ideal delay cell in Fig. 5.3. The transfer function can be split into a low pass filter with a DC gain of two and a unity gain part:

$$H_{ap} = \frac{2}{1 + s(\tau/2)} - 1 \tag{5.5}$$

In CMOS technology different active delay cells can be found in literature [BH04; Gar+15]. The g_m-RC first order all-pass in Fig. 5.4 is a "classical" realization of H_{ap} [HH89]. It is used to realize a delay cell with adjustable delay steps. The circuit consists of two parts. The unity gain part is realized by an inverter, e.g. a source degenerated amplifier with a gain of -1 as shown in Fig. 5.5(b). The phase difference of ϕ_1 and ϕ_2 is $180°$. To maintain gain symmetry the two resistors have to be equal or very high. The second part consists of a constant amplitude phase shifter and is shown in Fig. 5.5(b). Its behavior can be explained in a phasor diagram (Fig. 5.6). Assuming symmetrical output swings, V_1 is equal to V_2 and can be assumed to be real-valued. The signal vectors of the voltages of the resistor V_R and the voltage of the capacitor V_C must be perpendicular to each other. When adding these voltages they have to form a vector of constant length along the real axis. With Thales' theorem, the tip of the formed triangle is always on a circle. By adjusting the values of C_H and R_H, the phase can be tuned between 0 and $180°$. Note that the phase shift also depends on the frequency of the input signal.

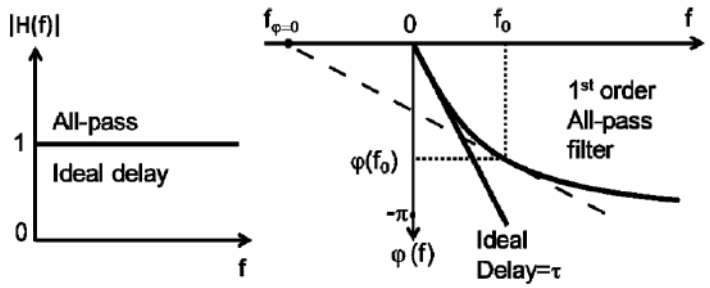

Figure 5.3: Comparison of a 1st order all-pass filter and an ideal delay in terms of the magnitude and phase transfer functions [GKN+13].

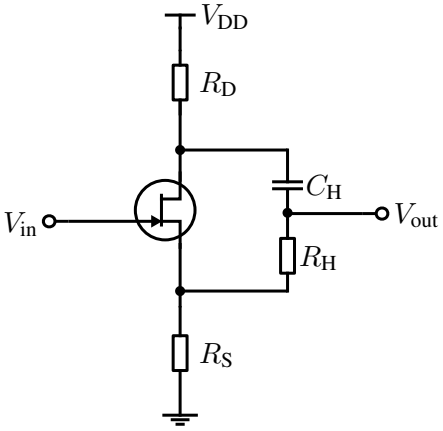

Figure 5.4: Circuit of the "classical" g_m-RC first order all-pass according to [HH89].

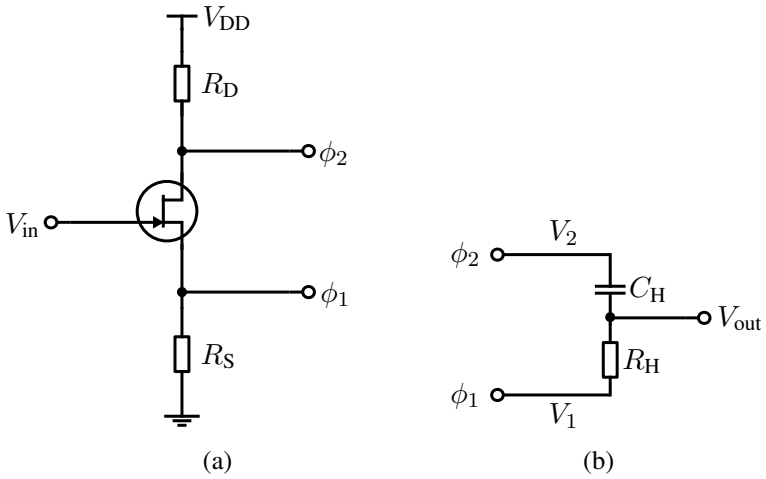

Figure 5.5: The "classical" delay cell of Fig. 5.4 divided in its two parts according to the the transfer function of Eq. 5.5. (a) shows the unity gain part and (b) realizes the low pass filter.

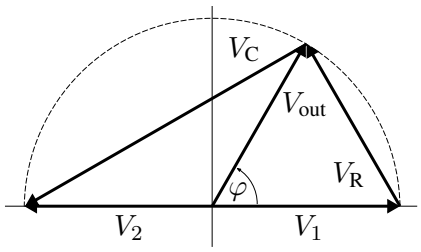

Figure 5.6: Phasor diagram of the circuit in Fig. 5.5(b) in order to illustrate its behavior as a constant amplitude phase shifter.

Table 5.1: Parameters used to simulate the "classical" all-pass cell.

Parameter	Value	Unit
R_{D}	10	kΩ
R_{S}	10	kΩ
C_{H}	50	fF
R_{H}	18	kΩ

According to [GKN+13] an approximate transfer function of the "classical" delay cell is

$$\frac{V_{\mathrm{out}}}{V_{\mathrm{in}}} \approx \frac{g_{\mathrm{m}}}{g_{\mathrm{m}} + G_{\mathrm{D}}} + \frac{1 - R_{\mathrm{H}} C_{\mathrm{H}} s}{1 + \left(R_{\mathrm{H}} + \frac{2}{g_{\mathrm{m}} + G_{\mathrm{D}}}\right)(C_{\mathrm{H}} + C_{\mathrm{in}})s} \tag{5.6}$$

with C_{in} as the input capacitance of the next stage which becomes relevant when cascading the delay cells. Based on this transfer function it can be seen that the DC gain of the circuit is less than one and the absolute value of the pole and zero differ from each other.

To approximate the transfer function of the first order all-pass (Eq. 5.4) two conditions have to be satisfied:

$$\frac{g_{\mathrm{m}}}{g_{\mathrm{m}} + G_{\mathrm{D}}} \approx 1 \tag{5.7}$$

$$\left(R_{\mathrm{H}} + \frac{2}{g_{\mathrm{m}} + G_{\mathrm{D}}}\right)(C_{\mathrm{H}} + C_{\mathrm{in}}) \approx R_{\mathrm{H}} C_{\mathrm{H}}. \tag{5.8}$$

Garakoui et al. realized the circuit with a CMOS transistor with a transit frequency of $12.4\,\mathrm{GHz}$. To prove its realizability with III/V semiconductors and to evaluate the abilities of the circuit when using transistors with a much higher f_{T}, different values for the parameters which meet the two conditions are tried out. Exemplarily, the results of a simulation with the values listed in Tab. 5.1 are shown in Fig. 5.7. The transconductance g_{m} for the used IAF mHEMT is around $1\,\mathrm{mS}$ for $V_{\mathrm{G}} = -0.1\,\mathrm{V}$ as extracted from a DC ADS simulation. Only the behavior of one cell is investigated, thus C_{in} is neglected.

The results in Fig. 5.7(a) show that for one cell the transmission loss is already around $-3.5\,\mathrm{dB}$. The phase of S_{21} is linear over frequency (Fig.5.7(b)) and its derivative w.r.t. frequency yields a delay of around $0.7\,\mathrm{ps}$. To reach a delay of $71\,\mathrm{ps}$, a large amount of these delay cells is needed which is not compatible with the underlying mHEMT technology due to its large transistors and relatively low yield as compared to e.g. CMOS. Thus, this approach will not be pursued further.

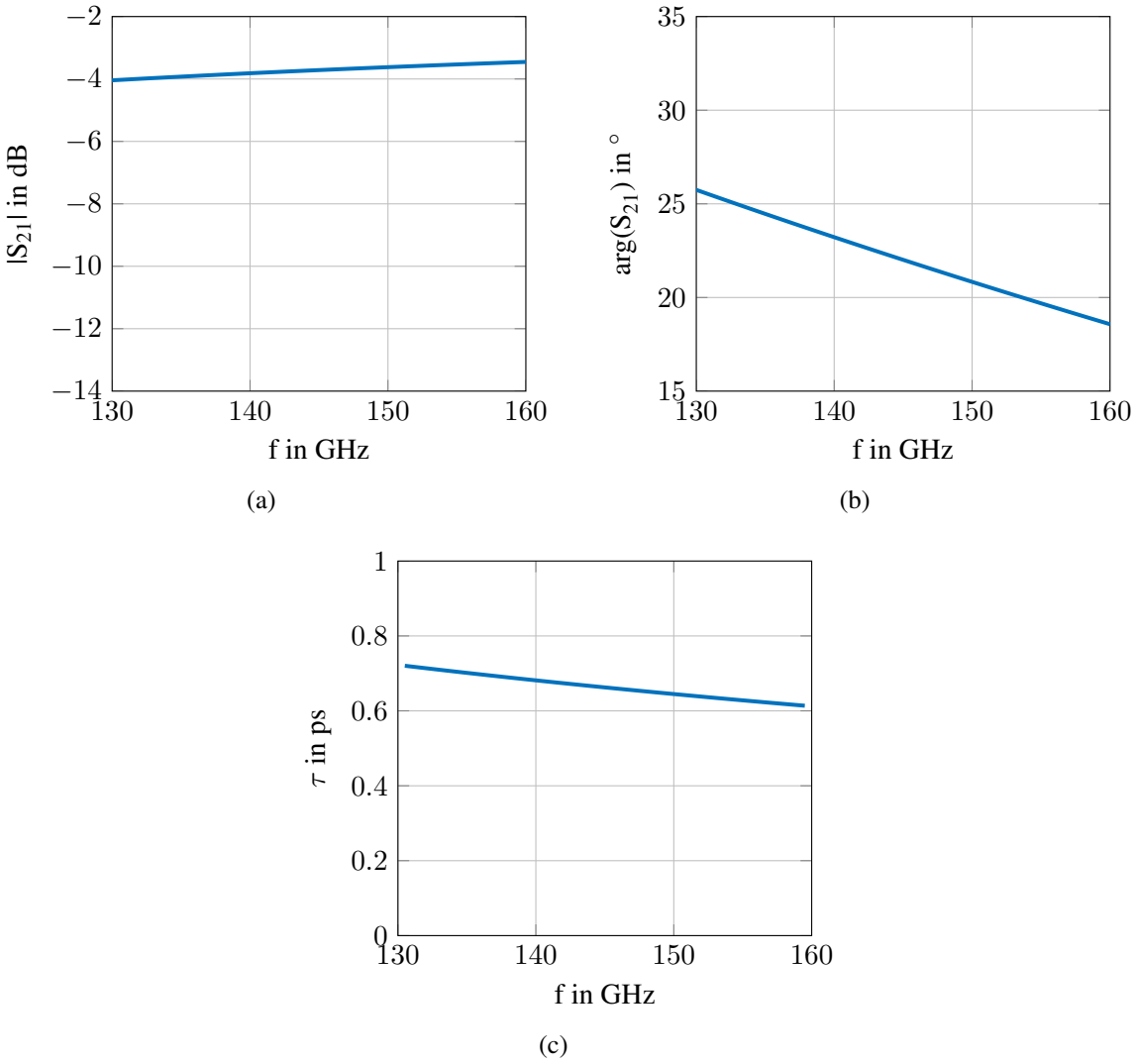

Figure 5.7: Simulation results of the "classical" all-pass in Fig. 5.4. (a) shows the magnitude (b) the phase of S_{21}. (c) shows the effective delay calculated as the derivative of $\arg(S_{21})$ w.r.t. the frequency.

5.3 Structures with Increased Delay per Length

As shown in the first section, a transmission line is the simplest option to generate an almost perfect effective delay. To overcome its disadvantage of large dimensions, this section discusses concepts which improve upon the basic TL in order to achieve a more effective space utilization.

5.3.1 Artificial Transmission Lines and Slow-Wave Structures

A TL can be represented by the distributed element model which describes the TL as an infinite chain of two-port unit cells. One unit cell contains the resistance per unit length R' in series with an inductance per unit length L', which are connected in parallel to a capacitance per unit length C' and a conductance per unit length G'. The theory of artificial transmission lines exploits this fact by realizing a potentially large number of unit cells consisting of a discrete inductor and capacitor much smaller than the wavelength. Thus, it is possible to realize the behavior of a TL up to a certain frequency while reducing its length due to the discrete components.

The delay of a single discrete unit cell can be calculated using basic network theory, starting with the transmission matrix of an LC section

$$M = \begin{pmatrix} A & B \\ C & D \end{pmatrix} = \begin{pmatrix} 1-\omega^2 LC & j\omega L \\ j\omega C & 1 \end{pmatrix}. \tag{5.9}$$

The phase of the corresponding forward voltage gain

$$\arg S_{21} = \arg \frac{2}{A + B/Z_0 + CZ_0 + D} \tag{5.10}$$

$$= \arg \frac{2}{2 - \omega^2 LC + j\omega/Z_0 + j\omega CZ_0} \tag{5.11}$$

can be linearized for $\omega \ll 1/\sqrt{LC}$ as

$$\arg S_{21} = \arctan \frac{\omega L + \omega C Z_0^2}{\omega^2 CLZ_0 - 2Z_0} \approx \underbrace{\frac{1}{2}\left(\frac{L}{Z_0} + CZ_0\right)}_{\tau} \omega. \tag{5.12}$$

In a matched environment ($Z_0 = \sqrt{L/C}$), this reduces to $\tau = \sqrt{LC}$.

On the other hand, the effective delay of a quasi-homogeneous structure with length l can be calculated as

$$\begin{aligned} \tau &= l/v_{\mathrm{g}} \\ &= l \cdot \frac{\partial \beta}{\partial \omega} \end{aligned} \tag{5.13}$$

with the group velocity v_{g}, which is given by the derivative of the phase constant β w.r.t. ω. Adhering to the usual convention, β is defined as the imaginary part of the propagation constant

$$\gamma = \alpha + j\beta \tag{5.14}$$

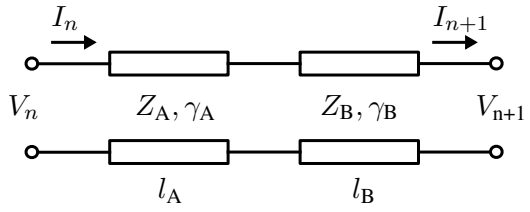

Figure 5.8: Circuit of periodic structure of two different impedance sections. The impedance sections are characterized by their length l_i, impedance Z_i and propagation constant γ_i.

with the attenuation constant α. In continuous transmission line theory, the propagation constant γ is

$$\gamma = \sqrt{(R' + j\omega L')(G' + j\omega C')} \tag{5.15}$$

which yields

$$\beta = \omega\sqrt{L'C'} \quad \text{or} \quad \tau = l\sqrt{L'C'} = \sqrt{LC}. \tag{5.16}$$

Comparing Eq. 5.16 and Eq. 5.12 shows that the approximation of a TL by a chain of discrete low-pass sections is valid for $\omega \ll \frac{1}{\sqrt{LC}}$ or, equivalently, for unit cells that are short compared to the wavelength. As ω approaches the critical frequency, the delay is no longer independent of the frequency and the losses increase due to the low-pass nature of the unit cells.

For the considered frequencies beyond $100\,\mathrm{GHz}$ the capacitance and inductances required for the design of a linear artificial transmission lines are very small so they are usually realized by short transmission line sections. In these so called slow wave structures, TL section with low and high impedances are alternated, representing capacitive and inductive behavior, respectively (see Fig. 5.8). This results in spatially separated storage of electric energy predominantly in the capacitive section and magnetic energy in the inductive section.

A propagating mode within such a periodic structure is characterized by the following properties:

- dispersion relation $\beta(\omega)$ (or $\gamma(\omega)$ when also considering attenuation)
- Bloch impedance Z_Bloch, which describes the effective impedance of the periodic structure
- cut-off frequency f_c due to the artificial periodicity

Note that for $f \ll f_c$ the dispersion is expected to be linear and becomes nonlinear as f approaches f_c. Based on the dispersion equation, the slow wave factor $\lambda_0/\lambda_\mathrm{g}$ and the effective delay τ can be calculated. The slow wave factor describes the ratio of the free-space wavelength and the guided wavelength of the slow wave structure

$$\frac{\lambda_0}{\lambda_\mathrm{g}} = \frac{c_0/f}{2\pi/\beta} = \frac{c_0\beta}{\omega} = \frac{c_0}{v_\mathrm{ph}}. \tag{5.17}$$

The delay τ can be calculated according to Eq. 5.13. In the linear dispersion region the group velocity v_g approximately equals the phase velocity v_ph.

5.3.2 Dispersion Relation and Bloch Impedance

To obtain an expression for the dispersion relation of the structure in Fig. 5.8, a standard method used to analyze periodic structures such as filters [Poz12] is employed. In a first step the transmission parameters of the unit cell is calculated. They are given by the matrix multiplication of the two transmission matrices

$$\begin{pmatrix} V_n \\ I_n \end{pmatrix} = \begin{pmatrix} \cosh(\gamma_i l_i) & Z_i \sinh(\gamma_i l_i) \\ \frac{1}{Z_i} \sinh(\gamma_i l_i) & \cosh(\gamma_i l_i) \end{pmatrix} \cdot \begin{pmatrix} V_{n+1} \\ I_{n+1} \end{pmatrix} \tag{5.18}$$

with the propagation constants γ_i and the lengths l_i describing the sections $i \in \{\mathrm{A}, \mathrm{B}\}$ with the characteristic impedances Z_A and Z_B, respectively. This results in the total transmission matrix of the unit cell of the periodic structure

$$\begin{pmatrix} V_n \\ I_n \end{pmatrix} = \underbrace{\begin{pmatrix} A & B \\ C & D \end{pmatrix}}_{:=M} \begin{pmatrix} V_{n+1} \\ I_{n+1} \end{pmatrix} \tag{5.19}$$

with

$$A = \cosh(\gamma_\mathrm{A} l_\mathrm{A}) \cosh(\gamma_\mathrm{B} l_\mathrm{B}) + \frac{Z_\mathrm{A}}{Z_\mathrm{B}} \sinh(\gamma_\mathrm{A} l_\mathrm{A}) \sinh(\gamma_\mathrm{B} l_\mathrm{B}) \tag{5.20}$$

$$B = Z_\mathrm{B} \cosh(\gamma_\mathrm{A} l_\mathrm{A}) \sinh(\gamma_\mathrm{B} l_\mathrm{B}) + Z_\mathrm{A} \cosh(\gamma_\mathrm{B} l_\mathrm{B}) \sinh(\gamma_\mathrm{A} l_\mathrm{A}) \tag{5.21}$$

$$C = \frac{1}{Z_\mathrm{B}} \cosh(\gamma_\mathrm{A} l_\mathrm{A}) \sinh(\gamma_\mathrm{B} l_\mathrm{B}) + \frac{1}{Z_\mathrm{A}} \cosh(\gamma_\mathrm{B} l_\mathrm{B}) \sinh(\gamma_\mathrm{A} l_\mathrm{A}) \tag{5.22}$$

$$D = \cosh(\gamma_\mathrm{A} l_\mathrm{A}) \cosh(\gamma_\mathrm{B} l_\mathrm{B}) + \frac{Z_\mathrm{B}}{Z_\mathrm{A}} \sinh(\gamma_\mathrm{A} l_\mathrm{A}) \sinh(\gamma_\mathrm{B} l_\mathrm{B}). \tag{5.23}$$

In a second step, Floquet's theorem is invoked. In its general form, it describes the form of the solutions of a linear set of ordinary differential equations for periodic geometries. In this analysis it reduces to the fact that the currents and voltages at the terminals of the unit cells are periodic up to a complex factor which is expressed as $e^{-\gamma l}$:

$$\begin{pmatrix} V_{n+1} \\ I_{n+1} \end{pmatrix} = e^{-\gamma l} \begin{pmatrix} V_n \\ I_n \end{pmatrix} \tag{5.24}$$

Inserting this in Eq. 5.19 yields

$$e^{\gamma l} \begin{pmatrix} V_{n+1} \\ I_{n+1} \end{pmatrix} = M \begin{pmatrix} V_{n+1} \\ I_{n+1}. \end{pmatrix} \tag{5.25}$$

$$\Leftrightarrow 0 = \left(M - e^{\gamma l} I \right) \begin{pmatrix} V_{n+1} \\ I_{n+1} \end{pmatrix} \tag{5.26}$$

with the identity matrix I. To allow for non-trivial solutions V_n, I_n, the determinant of the coefficient matrix $M - e^{-\gamma l} I$ has to vanish, leading to

$$0 = \det(M - e^{\gamma l} I) \tag{5.27}$$

$$\Leftrightarrow \cosh(\gamma l) = \frac{1}{2}(A + D) \tag{5.28}$$

in accordance with [Poz12]. Inserting the concrete expressions for the transmission parameters A and D yields the dispersion relation

$$\cosh(\gamma l) = \frac{1}{2}\left(\frac{Z_\mathrm{A}}{Z_\mathrm{B}} + \frac{Z_\mathrm{B}}{Z_\mathrm{A}}\right)\sinh(\gamma_\mathrm{A} l_\mathrm{A})\sinh(\gamma_\mathrm{B} l_\mathrm{B}) + \cosh(\gamma_\mathrm{A} l_\mathrm{A})\cosh(\gamma_\mathrm{B} l_\mathrm{B}) \tag{5.29}$$

$$= \frac{(1+K)^2}{4K}\cosh(\gamma_\mathrm{A} l_\mathrm{A} + \gamma_\mathrm{B} l_\mathrm{B}) - \frac{(1-K)^2}{4K}\cosh(\gamma_\mathrm{A} l_\mathrm{A} - \gamma_\mathrm{B} l_\mathrm{B}) \tag{5.30}$$

with the impedance ratio

$$K = \frac{Z_\mathrm{A}}{Z_\mathrm{B}}. \tag{5.31}$$

Based on the dispersion relation the propagation constant is calculated to

$$\gamma = \frac{1}{l}\operatorname{arcosh}\left(\frac{(1+K)^2}{4K}\cosh(\gamma_\mathrm{A} l_\mathrm{A} + \gamma_\mathrm{B} l_\mathrm{B}) - \frac{(1-K)^2}{4K}\cosh(\gamma_\mathrm{A} l_\mathrm{A} - \gamma_\mathrm{B} l_\mathrm{B})\right). \tag{5.32}$$

The Bloch impedance of the periodic structure is given by

$$Z_\mathrm{Bloch} = \frac{V_{n+1}}{I_{n+1}} = \frac{V_n}{I_n} = \frac{-2B}{A - D \mp \sqrt{(A+D)^2 - 4}}. \tag{5.33}$$

The last equality follows from inserting Eq. 5.28 into Eq. 5.24.

For the simplified case of $\gamma = j\beta$ the expression for the dispersion equation (5.30) agrees with the results of Seki et al. [SH81]. The authors analyze the behavior of a slow wave structure in GaAs for the special case of $\beta_\mathrm{A} = \beta_\mathrm{B}$, deriving the simplified expression for the Bloch impedance

$$Z_\mathrm{Bloch} = \sqrt{Z_\mathrm{A} Z_\mathrm{B}}. \tag{5.34}$$

This corresponds to a Taylor approximation of the general expression for Z_Bloch in Eq. 5.33, truncated after the zeroth order.

5.3.3 Concrete Realizations of Slow-Wave Structures

Based on the calculations in the previous section, two different approaches for a slow wave structure are simulated and analyzed w.r.t. the parameters β, Z_Bloch, f_c, the slow wave factor and the effective delay.

1. As a baseline reference, the listed parameters are calculated and simulated for a standard CPW transmission line with an impedance of around $50\,\Omega$ and a length of $50\,\mu\mathrm{m}$. The CPWs originally used in the radar transceiver MMIC are realized in a $50\,\Omega$ environment which results in a fixed spacing $d = 50\,\mu\mathrm{m}$ of the two ground planes. This leads to a width of the inner conductor of $w_\mathrm{CPW} = 16\,\mu\mathrm{m}$.
2. The second structure consists of two alternating transmission line sections with different widths of $w_\mathrm{CPW,1} = 5\,\mu\mathrm{m}$ ($Z_\mathrm{A} = 80\,\Omega$) and $w_\mathrm{CPW,2} = 40\,\mu\mathrm{m}$ ($Z_\mathrm{B} = 30\,\Omega$). For $d = 50\,\mu\mathrm{m}$ and observing the design rules regarding minimum structure sizes, these are the minimum and maximum realizable impedances, respectively. Both sections have a length of $25\,\mu\mathrm{m}$.

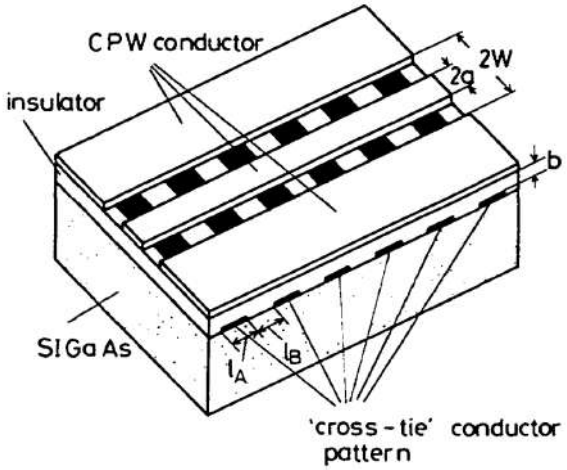

Figure 5.9: Structural view of the cross-tie coplanar waveguide. On the top metal layer the CPW conductor is realized while on the second metal layer floating stripes are oriented perpendicular to the wave propagation direction [SH81].

3. For the last structure, the different impedances are realized by inserting floating stripes underneath the CPW, perpendicular to the direction of the wave propagation and separated by an insulator (Fig. 5.9). Other works propose the usage of an epitaxial layer [HO77] or realize the slow wave structure with high-Q overlap capacitors [BD79], both of which are technologically more challenging. The structure based on floating stripes is referred to as 'cross-tie' coplanar waveguide (CT-CPW) in literature [SH81]. The section with a stripe under the CPW shows capacitive behavior while the second section can be designed to have a stronger inductive behavior [BFF15]. With two metal layers available in the IAF mHEMT stack, the CPW can be realized on the top layer METG and the floating stripes on the MET1 layer. The isolating layer consists of SiN. The length of the section with the stripes is chosen to $l_{\text{stripe,1}} = 20\,\mu\text{m}$ and for the standard CPW sections to $l_{\text{CPW,2}} = 30\,\mu\text{m}$. The inner conductor width is chosen to $10\,\mu\text{m}$ for both sections.

To evaluate the two different slow wave structures according to theory, Z_A, Z_B, β_A and β_B of the sections with constant impedance have to be known. The impedances of the TL sections $i \in \{\text{A}, \text{B}\}$ can be calculated as

$$Z_i = \sqrt{\frac{L_i'}{C_i'}} \tag{5.35}$$

with the inductance per unit length L' and the capacitance per unit length C'. For the sake of simplicity, losses are neglected in this expression. As already shown in Eq. 5.16, the phase constant can be calculated as

$$\beta_i = \omega\sqrt{L_i' C_i'}. \tag{5.36}$$

Table 5.2: Parameters for the different slow wave structures.

Structure	Section 1				Section 2			
	w_1 µm	l_1 µm	L'_1 nH/m	C'_1 pF/m	w_2 µm	l_2 µm	L'_2 nH/m	C'_2 pF/m
Transmission Line	16	25	369	143	16	25	369	143
Alternating TL	5	25	580	91	40	25	202	262
CT CPW	10	30	788	6494	10	20	454	116

To obtain the values for L' and C' an ADS S-Parameter simulation is performed for the different sections. By converting the S-parameters to ABCD-parameters, γ and Z_0 can be calculated as

$$\gamma = \frac{1}{l}\operatorname{arcosh}(A) \tag{5.37}$$

$$Z_0 = \sqrt{\frac{B}{C}}, \tag{5.38}$$

which is immediately clear from Eq. 5.18. The series impedance and parallel admittance of the TL are given by

$$Z_\mathrm{L} = \gamma Z_0 = R' + j\omega L' \tag{5.39}$$

$$Y_\mathrm{L} = \gamma\frac{1}{Z_0} = G' + j\omega C' \tag{5.40}$$

which leads to

$$L' = \frac{1}{\omega}\operatorname{Im}(\gamma Z_0) \tag{5.41}$$

$$C' = \frac{1}{\omega}\operatorname{Im}(\gamma/Z_0). \tag{5.42}$$

Note that for analyzing L' and C' for the CT-CPW, the stripes are modeled as MIM capacitors in the ADS simulation. As verified by a 3D simulation, the behavior of the standard MIM capacitor corresponds to a section with floating stripes to a very good approximation.

Tab. 5.2 shows the parameters for the different approaches. The dispersion of the single sections of the alternating TL and of the CT-CPW are compared in Fig. 5.10. It can be seen that for the alternating TL the phase constants are almost the same while for the CT-CPW the phase constants differ by a factor of five.

The Bloch impedance for the standard TL is $50.8\,\Omega$ which agrees with the characteristic impedance of $50.7\,\Omega$, proving the correctness of the derived expression in this limit. For the alternating TL it is $Z_\mathrm{Bloch} = 47\,\Omega$ and for the CT-CPW it is $Z_\mathrm{Bloch} = 15\,\Omega$.

The 3D simulation is performed with the Computer Simulation Technology (CST) software. Corresponding to the theory of periodic structures, one cell of each structure is modeled and simulated with the eigenmode solver of CST. It calculates the propagating modes and their corresponding field patterns. In contrast to the transient and frequency solvers, the eigenmode solver supports

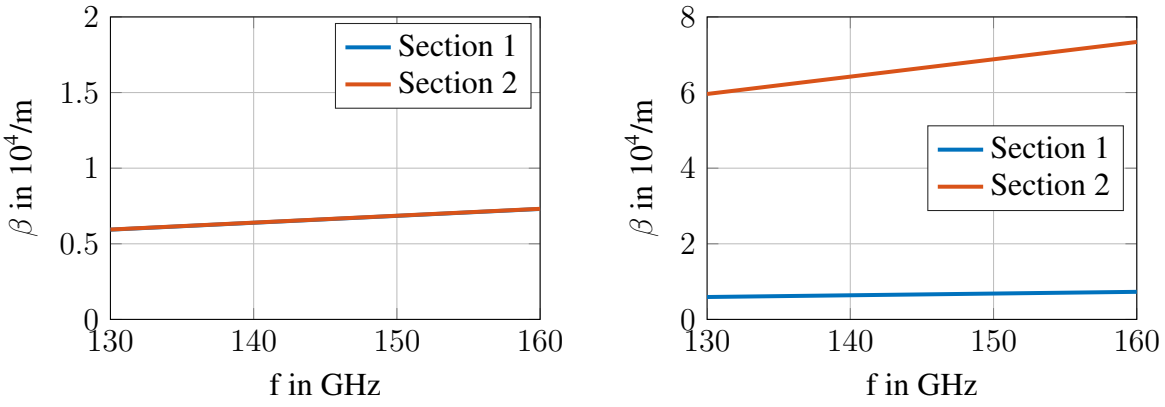

Figure 5.10: Comparison of the phase constant of the two individual impedance sections for (a) the alternating TL and (b) the CT-CPW. The corresponding values for the characteristics of section 1 and section 2 can be obtained by Tab. 5.2. In subfigure (a), the two curves are almost identical.

periodic boundaries on the faces containing the exciting RF port which corresponds to the boundary conditions of Floquet's theorem. Periodic boundaries have the same field pattern while their phase difference can be varied [CST19]. For the first resonance frequency the phase difference corresponds to βl. Varying the phase difference or β, respectively, results in the dispersion curve. Note that the eigenmode solver does not support open boundaries. As a workaround, a metal cage is added with sufficient spacing between its walls and the structure. By ensuring that the fields belonging to the analyzed modes have negligible magnitudes in the vicinity of the cage, it is assumed that the metal cage does not influence the solution in any significant way.

Based on the simulation results of the dispersion relation, the slow wave factor can be calculated as in Eq. 5.17. To calculate τ (cf. Eq. 5.13) the derivative of β has to be evaluated numerically, e.g. using the standard first order difference quotient. Unfortunately, the eigenmode solver does not provide easy access to the Bloch impedance, i. e. the surface / line integral of the electric / magnetic field over the port area.

The resulting phase constant β according to theory and simulation is plotted in Fig. 5.11 for all three structures. The continuous lines show the results of the theory, while the dotted lines show the results of the CST simulation. It can be observed that the values of the theory and the simulation are in the same range. The CT-CPW features the highest values for β while the alternating TL is just slightly above the reference curve. Theory predicts the first cutoff frequency of the CT-CPW at $212\,\mathrm{GHz}$ and for the alternating TL at $934\,\mathrm{GHz}$. The simulations show a slightly lower cutoff frequency.

Fig. 5.12 shows the slow wave factor of the three different structures. Analogous to the result of β, the CT-CPW yields the highest slow wave factor. The delaying effect of the alternating TL as compared to the standard TL is very small.

To get an idea of the effective delays achievable with the described structures, the results for τ can

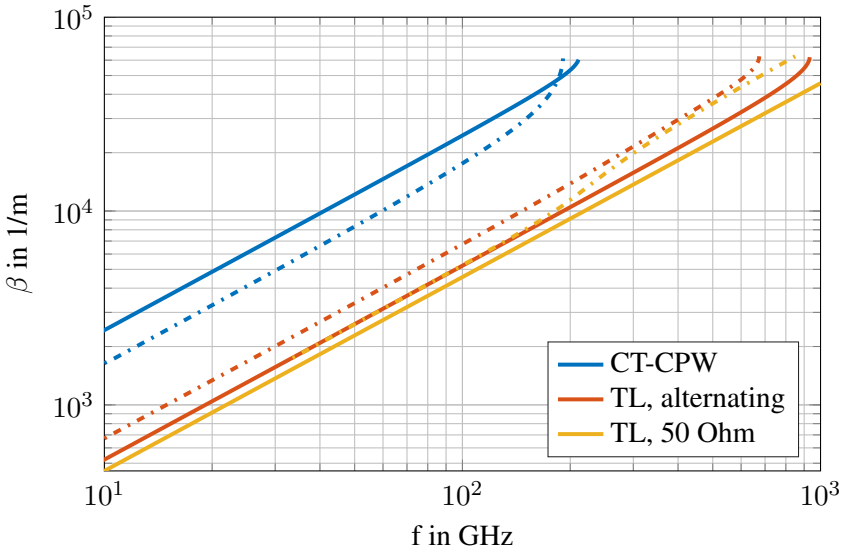

Figure 5.11: Dispersion relation for the three investigated structures. The dotted lines show the results of the CST simulation, while the continuous lines show the results of the theory. The cut-off frequency is indicated by the bend of the curve.

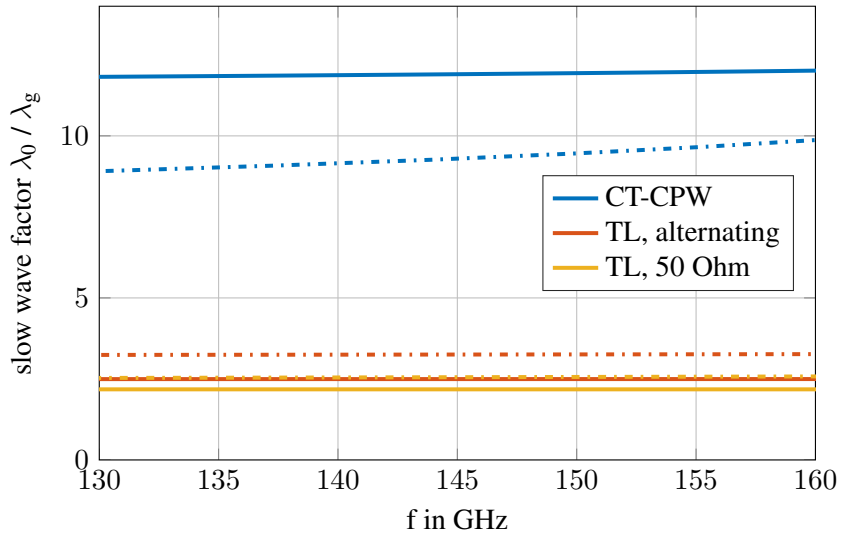

Figure 5.12: Results for the slow-wave factor of the investigated structures. It is calculated according to Eq. 5.17. The color coding is the same as for Fig. 5.11.

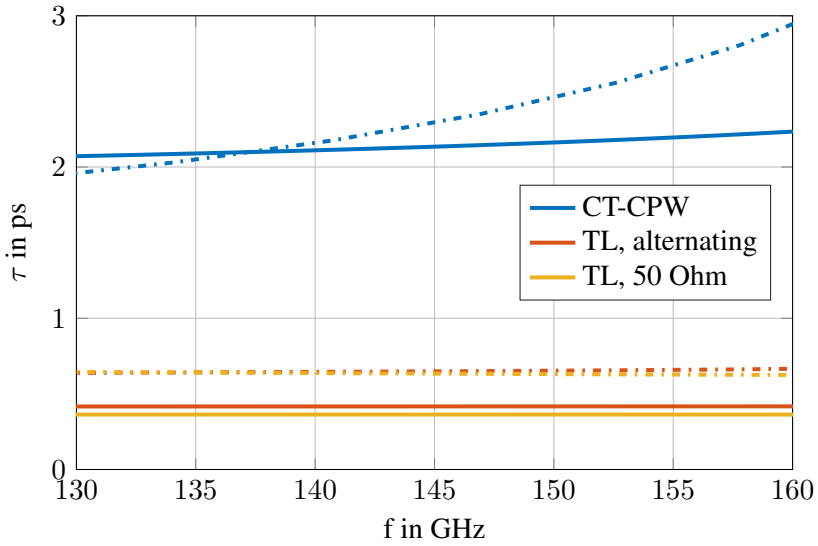

Figure 5.13: Achievable delays of the analyzed unit cells with a length of $50\,\mu\mathrm{m}$. The delay can be obtained according to 5.13. For the CST results, the derivative is evaluated numerically. Again, the color coding is the same as for Fig. 5.11.

be seen in Fig. 5.13. The highest effective τ is around $2.1\,\mathrm{ps}$ with a structure length of $50\,\mu\mathrm{m}$ for the CT-CPW structure. It shows a slight variation with the frequency as β is not perfectly linear over the displayed bandwidth. There is a clear trade-off between dispersion linearity (or proximity to f_c) and the achievable delay.

In summary, the presented results show that the delay of the alternating TL is not much higher than the delay of a normal TL. This can be explained by the very similar values of the phase constant of both sections. At the same time, the alternating TL has the obvious advantage of a characteristic impedance of $50\,\Omega$ which can be easily matched. A first evaluation of the cross-tie coplanar waveguide, however, shows very promising results regarding the achievable effective delay. Compared to a standard TL, the delay is increased by a factor of 3.5, leading to a decrease in the space utilization of the same amount. Floquet theory predicts a corresponding impedance of roughly $15\,\Omega$.

6 Conclusion and Outlook

In the present work, the system performance of resistive mixers has been investigated as part of a $140\,\mathrm{GHz}$ radar transceiver developed at the Fraunhofer IAF. Preliminary measurements of the integrated radar front end had shown an unexpected behavior of the conversion gain over the frequency. Two dips can be observed in the operating bandwidth which lead to a reduced system performance. Using a single antenna for transmitting and receiving creates a coupling path of the LO signal to the RF port of the receiving mixer via the Lange coupler. Thus not only the desired RF signal but also a part of the LO signal is present at the mixer.

To investigate the impact of the additional LO-RF signal on the downconversion process, a systematic analysis of the FET resistive mixer in the system context has been performed. Based on ADS simulations, the behavior of the FET at the drain and gate node has been examined. Two assumptions about the occurrence of the dips can be drawn from the simulation: There is a correlation of the accepted LO power with the dips in G_c which leads to the first assumption that the LO-RF signal present at the drain couples to the gate via the parasitic drain-gate capacitance. In the case of destructive interference of the LO and LO-RF signal the power level at the gain is not high enough and the mixing process becomes very inefficient. In addition, the dips in G_c show a correlation with the maximum of the drain bias which results from the mixing process of the LO and LO-RF signal. This leads to the second assumption that the FET is not operated at its optimum operating point. HB simulations have shown that the self-biasing effect is a consequence of the dips but not the cause.

In order to quantify the first assumption, an analytic model of the resistive mixer in the presence of the additional LO-RF path is developed. In the first model the LO-RF path is directly included in the expression for the gate voltage, whereas the more complex second model modifies the equivalent circuit in a suitable way. The analytic models depend only on a small number of accessible system parameters. Thus it can be seen that the capacitance C_{GD}, the effective delay τ and the voltage ratio $\hat{U}_{\mathrm{LO}}/\hat{U}_{\mathrm{LORF}}$ are the main influences on the observed behavior of the conversion gain. In contrast to the ADS simulation, the analytic models allow the evaluation of the influence of the capacitance C_{GD}. The results of the analytic models support the first assumption about the occurrence of the dips.

For the experimental verification of this assumption, a complex measurement setup has been devised and realized which successfully reproduces the dips in G_c in the presence of the additional LO-RF path within the controllable environment of an individual resistive mixer. In a first measurement sequence the conversion gain has been directly measured over the frequency. It was not possible to reproduce the dips because of the uncertainty regarding the phase relation limitation of the LO and LO-RF signal leading to very noisy results. To overcome this constraint, a new ap-

proach for measuring the conversion gain has been developed by varying the phase relation of the LO and LO-RF signal for each frequency point. By additionally measuring the IF-DC signal, the latter can be used as a reference for the phase relation of the LO and LO-RF signal and thus for a phase calibration, effectively eliminating the negative influence of the nonlinear multiplication and amplifying stages in the signal paths on the phase control. With this setup, the influence of the effective delay τ, the power levels $P_{\mathrm{LO}}/P_{\mathrm{LORF}}$ and the global phase shift φ_0 can be investigated. The measurement results support the hypothesis drawn from the ADS simulation in combination with the developed models.

Having gained a structured and in-depth understanding of the performance of the used resistive mixer in the context of a single-antenna radar transceiver, different solution approaches have been evaluated. The most general component needed to compensate for the effective delay between the LO and LO-RF signal has been identified as an all-pass filter with a linear phase transfer function in the operating bandwidth. According to this, the following three structures have been evaluated.

1. Simple transmission line:

   It is possible to compensate for the effective delay with a simple TL featuring an almost perfectly linear phase. However, due to its large dimensions it is not economical to insert such a delay line into the existing circuit.

2. First order g_m–RC active delay cell:

   The "classical" g_m–RC first order all-pass often used in CMOS technology is analyzed w.r.t. its applicability to the IAF technology. First simulations of the active first order all-pass filter do not show promising results regarding the achievable effective delay. A large number of these cells would be necessary to realize a sufficient effective delay. As the available transistors are significant larger than e.g. in CMOS technology, this approach was not pursued further.

3. Slow-wave structure:

   Slow-wave structures have been found to be a promising possibility to reach a more effective space utilization as compared to the simple transmission line. Two realizations of a slow-wave structure were theoretically analyzed and EM simulated.

   The first structure realizes the slow wave behavior by alternating TLs with different widths. Considering the $50\,\Omega$ environment of the transceiver, the attainable effective delay is very limited and compared to a basic TL its slow-wave factor is around 1.1. The (only) advantage of this structure is a Bloch impedance of around $50\,\Omega$.

   The second structure realizes the slow-wave behavior by periodically inserting metal stripes underneath the CPW structure, also leading to sections of higher and lower impedances. In comparison to a basic TL, a promising slow-wave factor of 3.5 can be achieved which corresponds to a decrease in the space utilization of the same amount. Floquet theory predicts a corresponding impedance of roughly $15\,\Omega$ for the chosen geometries. Depending on the system environment, this can be seen as a potential drawback or a feature of the structure.

As an outlook, various aspects have to be investigated further to actually implement an effective delay in the MMIC transceiver. For the CT-CPW structures, the following steps are proposed:

- Development of a simulative approach to extract the Bloch impedance
- Design of a suitable matching network for the CT-CPW. Note that the proposed delay line is driven by an amplifier in the transceiver context, thus the lower characteristic impedance could actually positively affect the design of the matching network.

The LNA in the receiver path also allows for further investigations in order to minimize the influence of the LO-RF signal on the mixer. The measurements of the radar front end with different drain bias currents of the LNA show that the dips can be reduced with lower drain bias currents with the drawback of a reduced bandwidth. Based on this measurement the following aspects could be analyzed:

- Improvement of the matching of the LNA to realise a larger usable bandwidth for lower drain bias currents
- Measurement/simulation optimization of the phase behavior of the LNA with an input power level corresponding to the power level of the LO-RF signal. The phase behavior of an LNA is usually not given much attention, thus this measurement could allow a better understanding of the phase behavior of the LNA driven in saturation. Based on this knowledge it might be possible to remove some of the LNA stages without decreasing the conversion gain, but with the effect of reducing the effective delay it introduces in the LO-RF path.

Regarding the system performance the following questions could be addressed in future works:

- How sensitive is the FMCW radar system w.r.t. the nonlinearity of τ? The simulation results of the CT-CPW slow wave structure show that with higher slow-wave factors the nonlinearity of τ is increased due to the vicinity of the cut-off frequency.
- Which minimum effective delay has to be realized to sufficiently reduce the dips in G_c? To reduce the dips the inserted delay cell does not necessarily have to compensate for the entire effective delay of $71\,\mathrm{ps}$ when considering the possibility to shift the dips outside of the frequency bandwidth. The answer to this question depends on the designed global phase offset φ_0 in the integrated system.

In summary, the results of this thesis enable a systematic approach to the redesign of the $140\,\mathrm{GHz}$ FMCW radar transceiver and provide the basis for reducing the negative effects of the investigated mixer behvaior without drastically altering the system specifications such as the number of antennas.

Bibliography

[BD79] E. M. Bastida and G. P. Donzelli. “Periodic slow-wave low-loss structures for monolithic GaAs microwave integrated circuits”. In: *Electronics Letters* 15.19 (1979), pp. 581–582.

[BFF15] A. Bautista, A. Franc, and P. Ferrari. “Accurate parametric electrical model for slow-wave CPW and application to circuits design”. In: *IEEE Transactions on Microwave Theory and Techniques* 63.12 (2015), pp. 4225–4235.

[BH04] J. Buckwalter and A. Hajimiri. “An active analog delay and the delay reference loop”. In: *2004 IEE Radio Frequency Integrated Circuits (RFIC) Systems. Digest of Papers*. IEEE. 2004, pp. 17–20.

[Bro05] G. M. Brooker. “Understanding millimetre wave FMCW radars”. In: *1st international Conference on Sensing Technology*. 2005, pp. 152–157.

[Bun] Bundesministerium für Wirtschaft. *Entwicklung der erneuerbaren Energien in Deutschland im Jahr 2018*. `https://www.erneuerbare-energien.de/EE/Navigation/DE/Service/Erneuerbare_Energien_in_Zahlen/Entwicklung/entwicklung-der-erneuerbaren-energien-in-deutschland.html` (visited on 2019-07-02).

[CST19] CST AG. *Reference Manual - CST Studio Suite 2018*. 2019.

[DSM15] G. Dua, Ghali V. S., and R. Mulaveesala. “Testing and evaluation of glass fiber reinforced polymers by thermal wave imaging”. In: *2015 International Conference on Signal Processing and Communication Engineering Systems*. IEEE. 2015, pp. 522–526.

[FL16] J. Fu and C. Liu. “In-line phase contrast computed tomography of carbon/carbon composites”. In: *2016 IEEE International Conference on Information and Automation (ICIA)*. IEEE. 2016, pp. 1501–1504.

[GH94] C. Graciet and B. Hosten. “Simultaneous measurement of speed, attenuation, thickness and density with reflected ultrasonic waves in plates”. In: *1994 Proceedings of IEEE Ultrasonics Symposium*. Vol. 2. IEEE. 1994, pp. 1219–1222.

[GKN+13] S. K. Garakoui, E. A. Klumperink, B. Nauta, et al. “Frequency Limitations of First-Order $g\_\{m\}-RC$ All-Pass Delay Circuits”. In: *IEEE transactions on circuits and systems II: express briefs* 60.9 (2013), pp. 572–576.

[Gar+15] S. K. Garakoui, E. A. M. Klumperink, B. Nauta, and F. E. van Vliet. “Compact cascadable gm-C all-pass true time delay cell with reduced delay variation over frequency”. In: *IEEE journal of solid-state circuits* 50.3 (2015), pp. 693–703.

[Gun+08] S. E. Gunnarsson, N. Wadefalk, I. Angelov, H. Zirath, I. Kallfass, and A. Leuther. “A G-band (140-220 GHz) microstrip MMIC mixer operating in both resistive and drain-pumped mode”. In: *2008 IEEE MTT-S International Microwave Symposium Digest*. IEEE. 2008, pp. 407–410.

[HH89] P. Horowitz and W. Hill. *The art of electronics*. Cambridge Univ. Press, 1989.

[HO77] H. Hasegawa and H. Okizaki. “MIS and Schottky slow-wave coplanar striplines on GaAs substrates”. In: *Electronics Letters* 13.22 (1977), pp. 663–664.

[Keya] *Keysight M8195A Arbitrary Waveform Generator - User’s Guide*. Rev. 6.0. Keysight Technologies, Mar. 2017.

[Keyb] *M8195A 65 GSa/s Arbitrary Waveform Generator - Data Sheet*. Rev. 3.1. Keysight Technologies, Oct. 2017.

[Kun99] K. S. Kundert. “Introduction to RF simulation and its application”. In: *IEEE Journal of Solid-State Circuits* 34.9 (1999), pp. 1298–1319.

[LD15] D. Lopez-Diaz. *Broadband Transceiver Circuits for Millimeter-Wave Wireless Communication*. Fraunhofer Verlag, 2015.

[Maa03] S. A. Maas. *Nonlinear microwave and RF circuits*. Artech house, 2003.

[Mei+19] D. Meier, C. Zech, B. Baumann, T. Link, M. Rösch, M. Schlechtweg, J. Kühn, and L. Reindl. “Classification of Epoxy Wedges in Glass-Fiber Reinforced Plastics Using a Millimeter-Wave Imaging System in W-Band”. In: *2019 IEEE Topical Conference on Wireless Sensors and Sensor Networks (WiSNet)*. IEEE. 2019, pp. 1–4.

[Ohl+16] M. Ohlrogge, A. Tessmann, A. Leuther, R. Weber, H. Maßler, M. Seelmann-Eggebert, M. Schlechtweg, and O. Ambacher. “Small signal modelling approach for submillimeter wave III–V HEMTs with analysation and optimization possibilities”. In: *2016 IEEE MTT-S International Microwave Symposium (IMS)*. IEEE. 2016, pp. 1–4.

[Pet12] K. Petermann. *Hochfrequenztechnik II Vorlesungsskript*. TU Berlin, 2012.

[Poz12] D. M. Pozar. *Microwave engineering*. Wiley, 2012.

[Ram17] K. Ramasubramanian. *Using a complex-baseband architecture in FMCW radar systems*. Texas Instruments, 2017.

[SH81] S. Seki and H. Hasegawa. “Cross-tie slow-wave coplanar waveguide on semi-insulating GaAs substrates”. In: *Electronics letters* 17.25 (1981), pp. 940–941.

[ST71] C. Schenk and U. Tietze. *Halbleiter-Schaltungstechnik*. Vol. 7. Springer, 1971.

[Win] Bundesverband Windenergie. *Zahlen und Fakten, Statistische Kennzahlen zur Erfolgsgeschichte Windenergie*. `https://www.wind-energie.de/themen/zahlen-und-fakten/` (visited on 2019-07-02).

Karlsruher Institut für Technologie | Institut für Hochfrequenztechnik und Elektronik

Selina Eckel

Master Thesis: System Performance of Resistive Mixers as Part of an Integrated D-Band Single Antenna Radar Transceiver

Period: 17.01.2019 – 03.07.2019

Examiner: Prof. Dr.-Ing. Thomas Zwick

Advisor: Dr.-Ing. Markus Rösch

Abstract: In the development of renewable energies, there is a trend towards larger wind turbines with rotor blade diameters reaching hundreds of meters. This increases the demands placed on the materials being used, requiring reliable material testing during the manufacturing process.

At the Fraunhofer Institute for Applied Solid State Physics IAF, an integrated D-Band FMCW radar transceiver has been developed for these applications. During the characterization of the transceiver, however, the conversion gain of the integrated mixer shows undesired dips within the operating bandwidth, which leads to a decreased system performance.

This work investigates the characteristics of the integrated FET resistive mixer within the given system context. Based on simulations, different hypotheses regarding the cause of the described behavior are formulated. In order to verify these assumptions, a theoretical model extending the standard mixer analysis is developed as well as a measurement setup enabling the investigation of an individual mixer cell within a precisely controlled artificial system environment.

An undesired coupling path of the local oscillator (LO) signal via the parasitic drain-gate capacitance is identified as the main culprit. In addition, it is shown that the strength of its impact on the conversion gain is significantly influenced by the effective delay between this coupling path and the original LO signal.

To compensate for the effective delay and thus eliminate the dips in the conversion gain, three different approaches for the realization of a delay cell in the LO path are introduced and evaluated based on different criteria. With respect to its practicability and efficient space utilization, a slow-wave structure with alternating metal stripes underneath a coplanar waveguide shows the most promising results.

Postanschrift: Institut für Hochfrequenztechnik und Elektronik
Kaiserstraße 12
D-76131 Karlsruhe

Gebäude: Engesserstraße 5, Geb. 30.10

Tel.: +49 (0) 721 608 4 2522
Sekr.: +49 (0) 721 608 4 2523
Fax: +49 (0) 721 608 4 5027
E-Mail: info@ihe.kit.edu
Web: www.ihe.kit.edu